Analysis and derivation of the spatial and temporal distribution of water vapor from GNSS observations

vorgelegt von
Dipl.-Ing.
Ming Shangguan
aus Jiangxi

von der Fakultät VI - Planen Bauen Umwelt
der Technischen Universität Berlin
Zur Erlangung des akademischen Grades

Doktor der Ingenieurwissenschaften
-Dr.-Ing.-

genehmigte Dissertation

Promotionsausschuss:
Vorsitzender: Prof. Jürgen Oberst
Gutachter: Prof. Roman Galas
Gutachter: Prof. Harald Schuh
Gutachter: Prof. Robert Weber
Gutachter: Dr. Jens Wickert
Tag der wissenschaftlichen Aussprache: 18. März 2014

Berlin 2014
D 83

Abstract

Water vapor in the atmosphere plays an important role in meteorological applications. The Global Navigation Satellite System (GNSS) provides accurate all-weather observations. The application of the existing GNSS infrastructure for atmosphere sounding leads to rather inexpensive and reliable measurements of the atmospheric water vapor. Observations from GNSS networks contain information about the spatial and temporal distribution of the water vapor. Therefore, the German Research Center for Geosciences Potsdam (GFZ) developed a water vapor tomography system to derive 3-Dimensional (3D) distributions of the tropospheric water vapor above Germany. The tomography makes use of the products provided by the GNSS processing center of the GFZ, where the atmosphere processing is currently limited to the Global Positioning System (GPS). Input data for the water vapor tomography are the GPS tropospheric products from about 300 ground stations. The GPS tropospheric products are Zenith Total Delay (ZTD), Integrated Water Vapor (IWV) and Slant Total Delay (STD).

The accuracy of STDs is one of the important factors for the quality of the derived water vapor tomography. However, the Earth Parameter and Orbit System Software (EPOS), which is used to estimate the GPS-STDs at GFZ, provides only limited information about the accuracy of STDs. Three months of Water Vapor Radiometer (WVR) data are used to validate the GPS-STD and estimate its accuracy. By comparing the GPS-STD observations with systematic hemisphere scans of the WVR it could be shown that inhomogeneous atmospheric structures are reliably reproduced by the STDs. The validation has shown a high accuracy of the estimated STDs.

The main objective of this thesis is to improve the water vapor tomography and to provide atmospheric water vapor products with good quality. A new tomographic algorithm based on a Kalman filter is added in the GFZ tomography system. The output is a 3D humidity field with a temporal resolution of 2.5 min and the error covariance matrix of the reconstructed states. The error covariance matrices for the observations and the covariance matrices for the uncertainty of the propagation are estimated in advance. The output has been validated with the Multiplicative Algebraic Reconstruction Technique (MART) tomography and radiosonde profiles.

Besides the accuracy of STDs, the quality of the derived tomography is depending on many factors such as the spatial coverage of the atmosphere with slant paths and the spatial distribution of their intersections. This leads to temporal and spatial variations of the reconstruction quality. Independent observations are required to validate the generated water vapor tomography. One year of radiosonde data from the German Weather Service (DWD) have been used for the validation. The wet refractivity field of the tomography with about 50 km horizontal resolution and 500 m vertical resolution has been interpolated to the RS profiles. The validations have been carried out point-by-point and also for the whole profile. A new technique has been developed to quantify the differences between humidity profiles. By considering the shape of the whole profile much more reliable conclusions can be drawn than by comparing only point-by-point differences. This method can be applied to improve the algorithms of GPS tomography.

Further attempts have been made to analyze the long-term IWV time series. Since the GPS data are available for more than 10 years, the GPS-IWV time series are used for climatological studies and they will become more important in future when long time series will be available. Trends have been calculated for the period 2002-2012 using the IWV from the German GPS ground-based network. Different methods (per station or per region) have been used to analyze the IWV time series. The methods will be helpful for meteorologists to analyze variations of the local or regional weather.

The investigations demonstrated that the ZTD, IWV and STD could describe the amount of water vapor and its distribution in the troposphere reliably. Especially the spatial and temporal variation of the water vapor distribution in the troposphere can be estimated with the tomographic technique. The quality of the derived 3D humidity fields has been checked with the help of radiosonde data. In general the result of the validation is good but it shows a need to improve the quality of the water vapor tomography.

With the development of GNSS (more satellites and more GNSS stations) and with improved algorithms (e.g., introduction of radiometer or radiosonde data), the tomography will in future provide a more complete view of the water vapor distribution in the atmosphere. In addition with increasing of GNSS time series, they can also be used for long-term studies. The GNSS meteorology can be widely applied in many fields, e.g., nowcasting, severe weather monitoring and data assimilation.

Kurzfassung

Der Wasserdampf in der Atmosphäre spielt eine wichtige Rolle in meteorologischen Anwendungen. Die globalen Positionierungssysteme (GNSS) liefern wetterunabhängige und präzise Beobachtungen. Die Anwendung der existierenden GNSS-Infrastrukturen für die Atmosphärensondierung ist ein kostengünstiger Weg, den atmosphärischen Wasserdampf mit hoher Genauigkeit abzuleiten. Beobachtungen von GNSS-Bodennetzen enthalten Informationen über die zeitliche und räumliche Wasserdampfverteilung. Deshalb hat das GeoForschungsZentrum Potsdam (GFZ) ein Wasserdampftomographiesystem entwickelt, um die 3D-Verteilung der Wasserdampfmenge in der Troposphäre über Deutschland abzuleiten. Eingabedaten für die Wasserdampftomographie sind die troposphärischen Datenprodukte von ca. 300 Bodenstationen die vom GNSS-Prozessierungssystem des GFZ bereitgestellt werden, wobei die Prozessierung momentan auf GPS-Daten beschränkt ist. Die wichtigsten Produkte sind die troposphärische Laufzeitverzögerung in Zenitrichtung (ZTD), der integrierte Wasserdampf (IWV) über den Stationen und die troposphärischen Laufzeitverzögerungen in Richtung zu den GPS-Satelliten (STD).

Die Genauigkeit der STDs ist ein wichtiger Faktor für die Qualität der Wasserdampf-Tomographie. Die GNSS-Prozessierungssoftware EPOS (Earth Parameter and Orbit system Software) des GFZ stellt nur begrenzte Informationen über die Genauigkeit der STDs bereit. Deshalb wurden Wasserdampf-Radiometerdaten über ein Vierteljahr verwendet, um sie mit GPS-STDs zu vergleichen und die Genauigkeit der STDs abzuschätzen. Durch den Vergleich der GPS-STD-Beobachtungen mit denen des Radiometers konnte gezeigt werden, dass inhomogene atmosphärische Strukturen zuverlässig durch die STDs wiedergegeben werden. Insgesamt bestätigt die Validierung die hohe Genauigkeit der aus den GNSS-Daten geschätzten STDs.

Ein wesentliches Ziel dieser Arbeit ist es, die Wasserdampftomographie zu verbessern und atmosphärische Wasserdampfprodukte mit guter Qualität abzuleiten. Ein neuer tomographischer Algorithmus, der auf einem Kalman-Filter basiert, wurde daher in das bestehende Tomographiesystem implementiert. Der Kalman-Filter liefert ein 3D-Feuchtefeld mit einer zeitlichen Auflösung von 2,5 Minuten und die zugehörigen Fehler-Kovarianz-Matrizen. Die Fehler-Kovarianz-Matrizen der STD-Beobachtungen und des zeitlichen Propagators wurden im Vorfeld bestimmt. Die Ergebnisse wurden mit denen anderer tomographischer Rekonstruktionsverfahren (MART) und mit Radiosondenprofilen verglichen.

Die Qualität der tomographischen Rekonstruktionen hängt nicht nur vom Fehler der STD-Beobachtungen, sondern auch von einer Reihe anderer Faktoren ab. Wesentlich ist unter anderem die räumliche Abdeckung der Schrägsichten und deren relative räumliche Verteilung bzw. die Verteilung der Schnittpunkte. Deshalb sind unabhängige Beobachtungen für die Validierung der rekonstruierten Feuchtefelder unerlässlich. In dieser Arbeit wurden die vom Deutschen Wetterdienst (DWD) bereitgestellten Radiosondenprofile eines ganzen Jahres zur Validierung der Tomographie genutzt. Die rekonstruierten Feuchtefelder hatten eine horizontale Auflösung von 50 km und eine vertikale Auflösung von 500 m. Diese Felder wurden für

den Vergleich auf die Radiosondenprofile interpoliert. Ausserdem wurde die Anzahl und Verteilung der STDs in der Nähe der Radiosonden-Stationen für die einzelnen Profile untersucht. Die Ableitung der statistischen Verteilung der Differenzen zwischen dem tomographisch rekonstruierten Feuchtefeld und den Radiosonden-Beobachtungen wurde zunächst unter der Annahme unabhängiger Einzelbeobachtungen durchgeführt. Darüber hinaus wurde in dieser Arbeit ein neues Verfahren zur Quantifizierung der Übereinstimmung vollständiger Profile entwickelt. Durch die Berücksichtigung der Gestalt des vollständigen Profils können wesentlich genauere Aussagen getroffen werden, als durch den statistischen Vergleich von punktweisen Beobachtungen. Diese Methode ist ein wesentliches Hilfsmittel für die weitere Entwicklung der Wasserdampftomographie.

Weiterhin wurden die längsten verfügbaren GPS-IWV-Zeitreihen analysiert. Inzwischen liegen GPS-Daten über Zeiträume von mehr als 10 Jahren vor, die eine Zeitreihenanalyse zulassen und für zukünftige klimatologische Untersuchungen interessant sind. Für den Zeitraum von 2002 bis 2012 wurden IWV-Trends für alle verfügbaren deutschen GPS-Stationen bestimmt. Darüber hinaus wurden regionale Trends für verschiedene geographische Regionen ermittelt. Die hierfür entwickelten Verfahren werden für meteorologische Untersuchungen zu räumlichen und zeitlichen Variationen des Wettergeschehens und für klimatologische Studien benötigt.

Insgesamt haben die Untersuchungen gezeigt, dass die ZTD-, IWV- und STD-Produkte die Menge und Verteilung des troposphärischen Wasserdampfes verlässlich wiedergeben. Insbesondere kann die zeitliche und räumliche Wasserdampfverteilung mit Hilfe der Wasserdampftomographie bestimmt werden. Die Qualität der rekonstruierten Feuchtefelder wurde mit Hilfe von Radiosondenprofilen abgeschätzt und es hat sich ergeben, dass in vielen Fällen eine gute Übereinstimmung vorliegt. Es wurde jedoch auch deutlich, dass eine Weiterentwicklung der Tomographie erforderlich ist.

Die zukünftige Entwicklung der GNSS führt zu einer Zunahme der Sendesatelliten und Bodenstationen. Parallel hierzu werden die Prozessierungsverfahren kontinuierlich weiterentwickelt, so dass sich die Voraussetzungen für die Wasserdampftomographie in naher Zukunft wesentlich verbessern werden. Mit der Verfügbarkeit längerer Zeitreihen werden auch die Trendanalysen deutlich aussagekräfiger. Insgesamt kann davon ausgegangen werden, dass die Anwendungen der GNSS-Meteorologie weiter zunehmen werden, z.B. für die Kurzfristvorhersage, zur Untersuchung von Extremwetterereignissen oder in der Datenassimilation für regionale und globale Wettervorhersagen.

Acknowledgments

This work was performed within the Helmholtz Research Network integrated Earth Observation System (HELMHOLTZ-EOS). Many thanks to Jens Wickert for his support and encouragement of my work and research. Thanks a lot to Michael Bender for his advice on questions and valuable suggestions, for continuous scientific guidance and assistance to complete the thesis.

I would like to thank Prof. Roman Galas for the mentoring at the university with valuable suggestions for the thesis, Prof. Robert Weber for the remarks on the written thesis and GNSS and Prof. Harald Schuh for his suggestions and support.

I feel very grateful to Galina Dick for providing tropospheric delays, to Torsten Schmidt for inquiry of the ECMWF data, to Nico Müller for providing part of the software code for the trend analysis, to Maorong Ge for the helpful discussions, to Antonia Faber and Stefan Heise for advice on English language. Thanks to Zhiguo Deng, Markus Ramatschi and Robert Heinkelmann for exchanging of ideas.

Next to my colleagues at GFZ my thanks goes to the Cologne group for providing WVR data of the COPS campaign. German Weather Service is thanked for providing radiosonde and synoptic data.

Thanks to the co-workers at the GFZ for my PhD time in Potsdam I spent with you and a big thanks to my family for the support. During the time of writing I received support and help from many people.

Contents

List of Symbols

$\bar{x}$	Arithmetic mean
$\mathbf{A}$	Design matrix
$\mathbf{C_{nn}}, \mathbf{C_{ss}}$	Covariance matrix of the noise and signal
$\mathbf{F}$	Propagation matrix
$\mathbf{G}$	Kalman gain matrix
$\mathbf{m}$	Observation vector
$\mathbf{n}$	State vector
$\mathbf{P_k}$	Covariance matrix of the state vector
$\mathbf{R}$	Observation error covariance
$\delta t_r, \delta t^s$	Clock bias of the receiver and satellite
δ	Postfit phase residual
Δ_{IWV_z}	Difference zenith IWV
Δ_{SIWV^r}	Relative difference SIWV
Δ_{SIWV}	Difference SIWV
$\delta_{trop}, \delta_{ion}$	Tropospheric and ionospheric corrections
ϵ	Elevation angle
ϕ	Latitude
Φ_r^s, L_r^s	Phase difference between the receiver and reference carrier
ρ_r^s	Geometric distance between the satellite and receiver
σ	Standard deviation
ξ	Remaining error
A_i	Monthly anomalies
c	Speed of light in vacuum
e	Partial pressure of water vapor
e_0	Surface partial pressure of water vapor
f, λ	Frequency and wavelength
G_N, G_E	Delay gradient parameter in the northern and eastern direction
H	Scale height
h	Height above sea level
IWV_z	Zenith IWV
m_h, m_w	Hydrostatic and wet mapping functions
M_i	Monthly mean
n, N	Refraction index and refractivity
N_r^s	Integer ambiguity
N_w, N_h	Wet and hydrostatic refractivity
P_0, T_0	Surface pressure and temperature
P_d	Partial pressure of dry air
P_r^s	Pseudorange
R_v	Specific gas constant for water vapor

S, S_0	Signal path and geometric path
s_i	Subpath in grid cell i
t	Time
T, P, rh	Temperature, Pressure, Relative humidity
T_m	Mean temperature of atmosphere
u_i	Weight
x_b	Biweight mean
x_m	Median

Acronyms

3D	3-Dimensional
4D-Var	4-Dimensional data assimilation
aLMo	alpine Local Model in Switzerland, Meteo Swiss
ALW	Atmospheric integrated Liquid Water
ART	Algebraic Reconstruction Technique
ASL	Above Sea Level
AWATOS	Atmospheric WAter vapor TOmography Software
CDMA	Code Division Multiple Access
COPS	Convective and Orographically induced Precipitation Study
COSMO	COnsortium for Small-scale MOdeling
DIAL	DIfferential Absorption Lidar
DOY	Day Of Year
DWD	German Weather Service (Deutscher Wetterdienst)
ECMWF	European Center for Medium-range Weather Forecasts
EIG EUMETNET	Economic Interest Grouping EUropean METeorological services NETwork
EPOS	Earth Parameter and Orbit system Software
FDMA	Frequency Division Multiple Access
FOC	Full Operational Capability
GCOS	Global Climate Observing System
GFZ	German Research Center for Geosciences
GLONASS	Russian Global Navigation Satellite System
GMF	Global Mapping Function
GNSS	Global Navigation Satellite System
GNSS4SWEC	Advanced Global Navigation Satellite Systems tropospheric products for monitoring Severe Weather Events and Climate
GPS	Global Positioning System
GRUAN	GCOS Reference Upper Air Network
HATPRO	Humidity And Temperature PROfiler
HyMeX	Hydrological cycle in Mediterranean EXperiment
IERS	International Earth Rotation and Reference Systems Service
IGS	International GNSS Service
IPPC	Intergovernmental Panel on Climate Change
IWV	Integrated Water Vapor
Lidar	Light Detection and Ranging
MAD	Mean Absolute Deviation

MART	Multiplicative Algebraic Reconstruction Technique
MCS	Master Control Station
MEO	Medium Earth Orbit
NMF	Niell Mapping Function
NWP	Numerical Weather Prediction
PPP	Precise Point Positioning
PRN	PseudoRandom Noise
PWV	Precipitable Water Vapor
RINEX	Receiver Independent Exchange Format
RMS	Root Mean Square
RS	Radiosonde
SAPOS	Satellite Positioning Service of the German Land Surveying Agencies
SART	Simultaneous ART
SHD	Slant Hydrostatic Delay
SIWV	Slant Integrated Water Vapor
STD	Slant Total Delay
SWD	Slant Wet Delay
US	United States
UTC	Universal Time Coordinated
VLBI	Very Long Baseline Interferometry
VMF	Vienna Mapping Function
WVR	Water Vapor Radiometer
ZHD	Zenith Hydrostatic Delay
ZTD	Zenith Total Delay
ZWD	Zenith Wet Delay

1 Introduction

In atmospheric processes, water vapor plays a major role at all scales, from the global climate to micro-meteorology. Its capability to transport the latent heat and moisture through the atmosphere is especially important for weather and climate (Hofmann-Wellenhof et al., 2008). Water vapor is lighter than air and triggers convection currents that can lead to clouds, which have a strong effect on the radiation budget. Water vapor is the most important greenhouse gas, which causes the warming of the atmosphere. Recently, the costs of natural disasters such as floods, droughts, and storms have increased drastically all over the world. Most of them were weather-related disasters.[1] Therefore, the continuous monitoring of water vapor on local, regional, and global scales is very important for severe weather monitoring, weather forecasting, and climate change modeling.

The term *GNSS* is the general name given to all navigation systems and which are used to determine the precise position, velocity, and time. Several countries have started to develop their own satellite navigation systems. The current operational GNSS are the United States (US) GPS and the Russian Global Navigation Satellite System (GLONASS). In the near future the European Galileo and the Chinese Beidou will also be fully deployed. Using the observations of existing geodetic GNSS networks to estimate water vapor information in the atmosphere is cost-efficient and rapidly developed. Since the introduction of the GNSS technique for measuring atmospheric water vapor by Bevis et al. (1992), several ground-based GNSS networks are in operation to provide spatiotemporally resolved information of water vapor (Wolfe and Gutman, 2000; Gendt et al., 2004; Karabatić et al., 2011). The Zenith Total Delay (ZTD), the Integrated Water Vapor (IWV), and the Slant Total Delay (STD) derived from GNSS observations are commonly accepted atmospheric observations for meteorological applications. Indeed, the IWV was proven to have an accuracy better than 2 mm using GPS satellite data (Bevis et al., 1992; Emardson et al., 1998; Köpken, 2001; Martin et al., 2006).

IWV and ZTD estimates do not provide any information on the vertical distribution of water vapor. The Slant Integrated Water Vapor (SIWV) derived from the slant path delay has been used instead of IWV in reports by Ware et al. (1997), Braun et al. (2001, 2003). WVRs can measure the SIWV with high accuracy and are usually used to validate GPS-SIWV. GPS-SIWV estimations are more strongly affected by observation and processing errors than the IWV, because the SIWV error cannot be reduced by averaging over time and multiple satellites (Braun et al., 2001, 2003). An application of the slant measurements is to reconstruct 3D water vapor fields with tomographic techniques, based on a dense GNSS receiver network (MacDonald et al., 2002; Bender et al., 2011b). GPS delays based on undifferenced phase observations (Flores et al., 2001; Hirahara, 2000) or double difference observations (Troller et al., 2006; Lutz et al., 2010) have been used in numerous studies to demonstrate the potential of the GNSS tomography. In France, a GPS tomography system using a least squares approach was applied in the ESCOMPTE field comparison (Champollion et al., 2005). In Switzerland a nationwide GNSS tomography

[1] `www.worldwatch.org/natural-catastrophes-2012-dominated-us-weather-extremes-0`

system called Atmospheric WAter vapor TOmography Software (AWATOS) was established and provides 3D water vapor fields for the preparation of assimilation into the alpine Local Model in Switzerland, Meteo Swiss (aLMo) (Troller et al., 2006). This system (Perler, 2011) is Kalman filter-based and uses GNSS double differenced data. In Germany, a water vapor tomography system was developed at the German Research Center for Geosciences (GFZ) (Bender et al., 2011a) using the Algebraic Reconstruction Technique (ART).

Some problems connected to the tomography technique became apparent. Studies (Troller et al., 2006; Perler, 2011) have shown differences between balloon soundings and tomographic solutions, as well as those computed by a numerical weather model and tomographic solutions. Therefore, the quality of the tomographic reconstructions require improvement. Because the quality of the GNSS tomography is influenced by a number of factors, independent observations are required to validate the quality of the 3D humidity field. Radiosonde (RS) data are often used to evaluate the capabilities of GNSS tomography (Gradinarsky and Jarlemark, 2004).

The continuous GNSS observations since the 1990s provide the possibility to analyse water vapor trends. Different studies to measure trends in IWV and ZTD data have been performed, e.g., Gradinarsky et al. (2002) investigated IWV trends over Sweden for the years 1993-2001, where they found positive trends of 0.1-0.2 $kg/(m^2y)$. Nilsson and Elgered (2008) studied IWV data for the same region but over a different time period, 1996-2006, and found trends between -0.02 $kg/(m^2y)$ and 0.1 $kg/(m^2y)$ with accuracy in the oder of 0.04 $kg/(m^2y)$. Other studies (Jin et al., 2007; Jin and Luo, 2009) used both ZTD and IWV data from a large number of globally distributed GPS sites to estimate trends. The largest differences in the mean IWV between summer and winter were found in mid-latitudes, especially in the northern hemisphere. A comparison of ZTD trends from GPS and Very Long Baseline Interferometry (VLBI) was done by Steigenberger et al. (2007), showing that the trends estimated with the two techniques differ significantly. This demonstrated that the estimated trend is very sensitive to artifacts such as different sampling rates and the remaining systematic effects within the individual techniques.

However, different studies derive different results based on various data sets, and this represents a need to combine the existing observational networks with consistent quality for climate research. To meet this requirement, the GCOS Reference Upper Air Network (GRUAN) will provide long-term, high-quality data to determine climatic trends and to constrain and validate data from space-based remote sensors.[2] GRUAN is an international reference upper air observing network, which was established by the Global Climate Observing System (GCOS). The GRUAN Lead Center is located at the Lindenberg Meteorological Observatory (DWD), Germany. The GRUAN GNSS precipitable water (GNSS-IWV) task team was established in summer 2010 and ground-based GNSS-IWV was identified as a Priority 1 measurement for GRUAN. The goal of the GNSS-IWV task team is to develop explicit guidance in hardware, software, and data management practices to gather GNSS-IWV measurements of consistent quality at all GRUAN sites.[3] The review current status of GNSS

[2] `www.wmo.int/pages/prog/gcos/index.php?name=GRUAN`
[3] `www.dwd.de` (search GRUAN Home)

instruments is documented and data guidance (e.g., type and temporal resolution of the ground-based GNSS data) will be developed. Then the GNSS data will be obtained with the consistent reprocessing at GFZ for climatological applications.

Furthermore, to improve the capabilities from concurrent developments in both the GNSS and meteorological communities, the new European COST Action *Advanced Global Navigation Satellite Systems tropospheric products for monitoring Severe Weather Events and Climate (GNSS4SWEC)* started in May 2013 with 41 institutions and 28 participating countries.[4] The main aim of this action is to synergize the three GNSS systems (GPS, GLONASS, and Galileo) to develop new, advanced tropospheric products, to exploit the full potential of multi-GNSS water vapor estimates on a wide range of temporal and spatial scales, for real-time water vapor monitoring, severe weather forecasting, and climate research.

In addition, many national and international research and operational programmes have been undertaken before, such as Hydrological cycle in Mediterranean EXperiment (HyMeX)[5], Gfg^2 project[6] and Economic Interest Grouping EUropean METeorological services NETwork (EIG EUMETNET) GNSS water vapor programme[7]. All of them explore GNSS applications in different fields, e.g., for quantification of the hydrological cycle, global environmental Earth observation and global Earth observation systems.

A close collaboration with all the existing research projects is intended. Both the GRUAN precipitable water task team and the COST Action GNSS4WEC will expand the international framework already in place with other European programmes to facilitate global collaboration, knowledge and data exchange. The COST Action works in collaboration with the GRUAN IWV task team as well as those at IGS, EUREF etc. to obtain consistent GNSS-IWV time series. The high quality reprocessed long-term GNSS data will improve the climate trend analysis, and the near real-time data will be assimilated into NWP models. On the other hand, the meteorological data from NWP can be used as input in GNSS processing algorithms to improve signal propagation modeling, thereby improving the accuracy of GNSS positioning, navigation and timing services. With the combined efforts from both atmospheric and geodetic communities, the nowcasting of severe weather events will be improved to reduce the risk of loss of life and damage to national infrastructure.

This thesis focuses on atmospheric water vapor derived from GPS measurements and their applications in meteorology. STDs, which contain the information on the vertical distribution of water vapor, are estimated by the Earth Parameter and Orbit system Software (EPOS) at GFZ. Using the GPS-STDs, the wet refractivity fields have been reconstructed with tomographic techniques. To check the accuracy of the input STDs and the quality of the derived tomography, validation studies have been made using independent data sets including WVR and RS. When the tropospheric products with Multi-GNSS (GPS, GLONASS, Galileo, Beidou) are available, the methods discussed in this thesis are applicable to all GNSS observations. The ZTDs

[4] www.cost.eu/domains_actions/essem/Actions/ES1206
[5] www.hymex.org
[6] www.gfg2.eu
[7] egvap.dmi.dk

and IWVs include the information on the horizontal distribution of water vapor. The methods have been developed to analyze the IWV time series per region or station, which is the goal of cooperation with GRUAN project and COST Action for long-term climatological studies. Within the selected periods the IWV trends have been derived.

The main objectives of this work are:

1) Evaluate the quality of STD derived from EPOS. EPOS provides limited information about the STD error because there are numerous related factors for its estimation. The accuracy of the STD that derived from GPS measurements is very important for monitoring water vapor as input observations for GPS tomography. Therefore, three months of the independent WVR data are used to estimate the accuracy of the STDs.

2) Analyze the water vapor time series of German stations for meteorological applications. More than 10 years of ground-based GPS data are available at GFZ. In partnership with GRUAN and COST Action projects, GFZ will provide higly accurate reprocessed GPS data for meteorological applications. These methods of deriving the meteorological parameters, such as trends and the water vapor amount, must be developed for climatology.

3) Improve the tomography software at GFZ and validate the results. A new Kalman filter method is implemented in the tomography software package. Furthermore, a validation method using RS data is developed to determine the quality of the derived wet refractivity field. This method is beneficial to evaluating the tomographic capability to resolve water vapor in the troposphere. In addition, the number and configuration of slant delays is also taken into account during validation.

Chapter 2 reviews atmospheric constituents, structure and observation methods to determine atmospheric water vapor, including a short introduction to numerical weather models and data assimilation. This is to provide an overview of the advantages and disadvantages of different water vapor measurements.

Chapter 3 introduces the fundamentals of GNSS meteorology. The basic principles of GPS ground-based data processing and the definition of the tropospheric delay are described, in addition to the connection between atmospheric quantities and GPS signal delays. An overview of the processing software EPOS used at GFZ is given.

Chapter 4 presents the validation results of GPS- and WVR-SIWV. Here, the three months of systematic WVR hemisphere scans are available. The STD, obtained by EPOS at GFZ, is converted into SIWV for the validation. The accuracy of the GPS-SIWV is estimated with the help of the WVR data. Several possible influencing factors (elevation angles, Atmospheric integrated Liquid Water (ALW), the amount of water vapor and weather situations) on the measurements are discussed.

Chapter 5 is dedicated to the assessment of the application of GNSS products in climate research and other related fields. With a special focus on the monthly averaged IWV, the daily, monthly and annual means can be calculated per station or regionally. Based on those statistics, linear trends are estimated for stations or

regions using the least squares method. In addition, a comparison beween GPS-IWV and IWV taken from a numerical weather model (ERA-Interim) is presented. With the chosen period 2002-2012, a trend analysis of GPS-IWV time series of German GPS stations is given as an example. For a regional analysis, the total amount of water vapor above the given region is estimated and regional and temporal variations are investigated.

Chapter 6 presents different methods (MART and Kalman filter) to reconstruct the 3D water vapor field. The tomography based on Kalman filter method is developed in this work and the Kalman filter is updated every 2.5 min with new observations. The error covariance matrices of the observations, the states and the uncertainty of the propagation are given in the tests. The result of the Kalman filter algorithm is shown together with results obtained with the MART method. In order to assess whether the GPS tomography is sufficiently accurate to describe the spatial and temporal distribution of water vapor, German RS data are used for validation. RS data of 2007 are available for the validation. The wet refractivity field of the tomography with about 50 km horizontal resolution and 500 m vertical resolution using the MART method is reconstructed at the ascent time of the RS data. A new validation technique considering the shape of the whole profile is used for the validation (Shangguan et al., 2013) and the number and distribution of STDs are investigated for each profile before the validation. Then all the profiles are studied with the help of the defined parameters for whole profiles. In contrast to point-by-point validation, the use of the defined parameter for whole profiles shows more visible and reliable results of the validation.

Chapter 7 presents the main conclusions and an outlook for future research.

2 Water vapor in the atmosphere

2.1 The atmosphere and the importance of water vapor

The atmosphere, surrounding the Earth surface and under the influence of gravitational attraction, consists of a shell of gases (nitrogen, oxygen, argon, water vapor, and a number of trace gases) as well as suspended solids. The atmospheric density decreases thinner from the Earth surface to the outer space. From the surface upwards it can be divided into troposphere, stratosphere, mesosphere, and thermosphere depending on the vertical variation of temperature (Fig. 2.1).

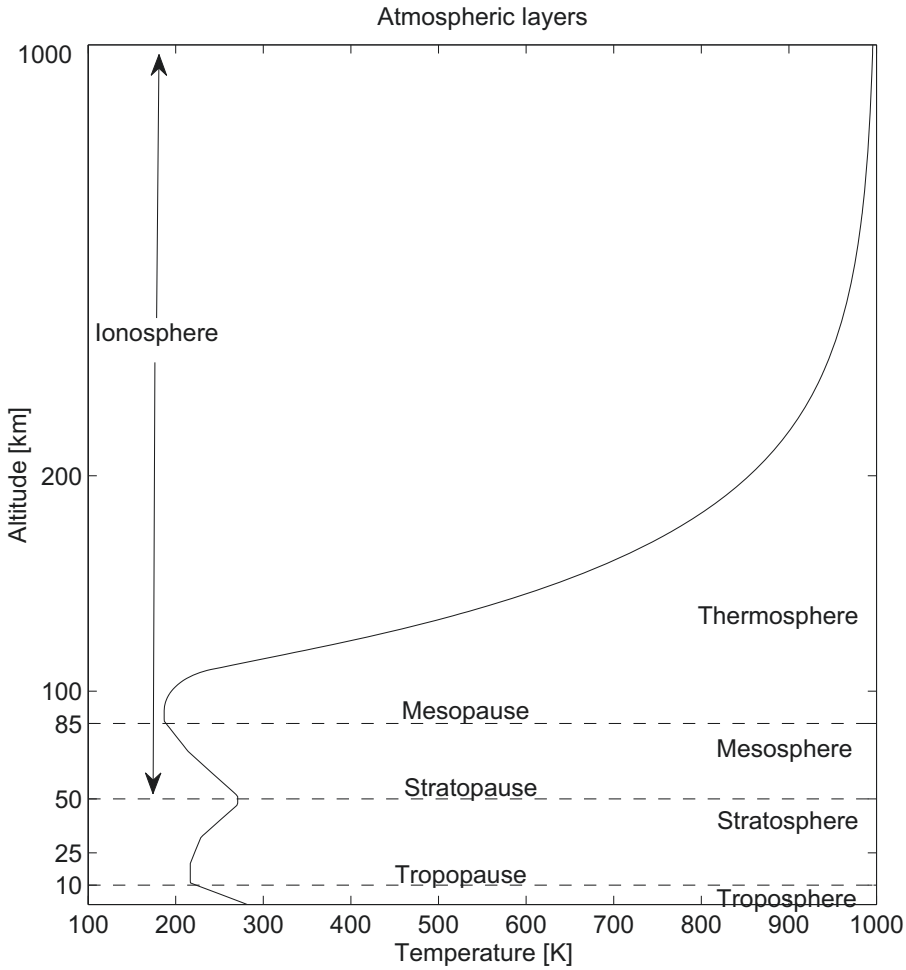

Figure 2.1: Vertical structure of the atmosphere and the vertical temperature profile. (US standard atmosphere)

The troposphere is warmed up by the radiation emitted from the Earth surface. With the decrease of air density, the temperature decreases from the surface to the upper atmosphere at an average lapse rate of about 6.5 K/km (Wallace and Hobbs, 2006). This decrease of temperature becomes weaker and finally reverses over the tropopause. The upper limit of the troposphere (tropopause) depends on the latitude, and is about 17 km at the equator and 10 km in the polar regions.

The temperature increases with the altitude in the stratosphere because the stratospheric ozone strongly absorbs the ultraviolet radiation from the sun. This heating from the absorption of the ultraviolet radiation by ozone reaches the maximum at about 50 km (stratopause). The temperature decreases again in the mesosphere and drops to the minimum at the mesopause. From the mesopause upwards, the temperature increases extremely through the thermosphere. This warming of the atmosphere is caused by the absorption of solar radiation, the dissociation of diatomic nitrogen and oxygen molecules and ionization (Wallace and Hobbs, 2006).

Another possible classification of the atmospheric structure can be made by the degree of ionization. In this approach the atmosphere is divided into the neutral atmosphere (troposphere and the lower stratosphere) and the ionosphere (50 km to 1000 km). Above the stratosphere, there is no ozone layer, which could absorb the radiation emitted by the sun. The solar radiation produces a significant ionization in this region. The free electrons in the ionosphere significantly affect the propagation of electromagnetic radiation. For GNSS signals, the ionosphere is a dispersive medium. Its effect on the propagation of the GNSS signal depends on the frequency and ionization. In the relative positioning over very short baselines the ionospheric delay can be neglected. Hence the ionospheric delays for the receivers with short baselines to the same satellite would be very similar and can be eliminated by differencing observations. For undifferenced observations, the first order ionospheric delay effects can be removed completely by combining two different carrier measurements on both L-band frequencies. The neutral atmosphere is not dispersive. Although both the ionosphere and the neutral atmosphere affect the propagation of radio signals, the effects are quite different. Unlike the ionosphere, the propagation of radio signals in the neutral atmosphere is frequency-independent. The index of refraction depends on air pressure, temperature, and water vapor content and it is difficult to model the index of refraction due to the dynamic behavior of tropospheric conditions (Seeber, 2003).

The atmosphere protects life on Earth by absorbing the ultraviolet radiation from the sun and keeps the lower atmosphere warmer than in the case of non-atmosphere planets by the so called *greenhouse effect*. Water vapor is the primary greenhouse gas, though it accounts for only 0-5 % by volume of the atmosphere. The water vapor distribution varies considerably both spatially and temporally, with a range of more than three orders of magnitude (Wallace and Hobbs, 2006). Most water vapor is located within the lowest few kilometers. The troposphere contains about 80 % of the mass of the atmosphere and nearly all the water vapor and aerosols (Wallace and Hobbs, 2006). About 50 % of the total atmospheric water vapor is located within the boundary layer, i.e. a layer up to about 1.5 km above the surface, less than 5-6 % of the water vapor can be found above 5 km (Seidel, 2002). The stratosphere contains less than 1 % of the total atmospheric water vapor (Seidel, 2002).

Besides the greenhouse effect, water vapor also plays an important role in the weather and climate through its phase changes between the gas, liquid, and solid states. The phase changes of water vapor lead to the formation of clouds, which strongly reflects the solar radiation to the outer space and absorbs long wave radi-

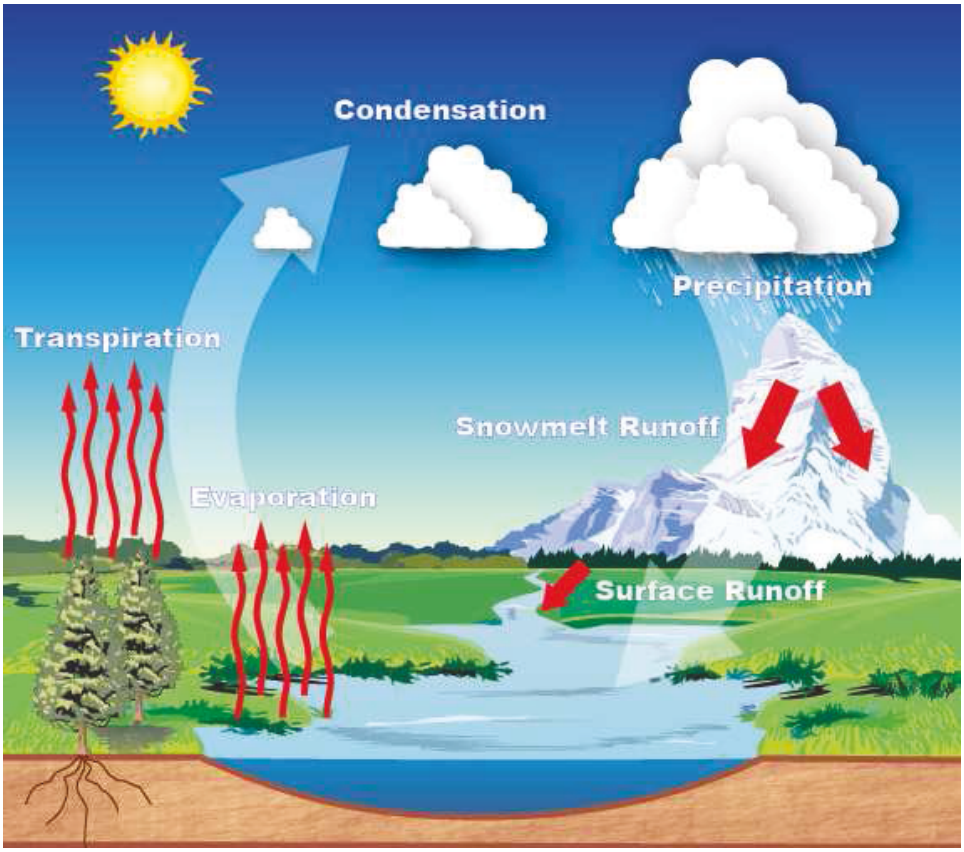

Figure 2.2: Hydrologic cycle. (`www.srh.noaa.gov/jetstream/atmos/hydro.htm`)

ation emitted from the surface. Because of the large concentration differences and the phase changes of water vapor, the relative humidity is usually used in measurements. The relative humidity is defined by the ratio in percentage of the partial pressure of water vapor in the mixture to the saturated vapor pressure (Andrews, 2010).

Figure 2.2 is the general hydrologic cycle, which dominates the distribution of the water resources in different regions. However, until recently there is still not enough observations available for every process of the hydrologic cycle, especially for the processes related to the water in the gas phase. These processes include the resources of water vapor such as evaporation, transportation, and the redistribution of water vapor by the transportation in the atmosphere.

2.2 Methods to detect the atmospheric water vapor

In atmospheric processes water vapor plays an important role for climate change and has a great spatial and temporal variability, not only in vertical but also in horizontal direction (Fig. 2.3).

There is a network of surface stations (synoptic stations) operated by weather services, which provide humidity data. Information about the vertical distribution

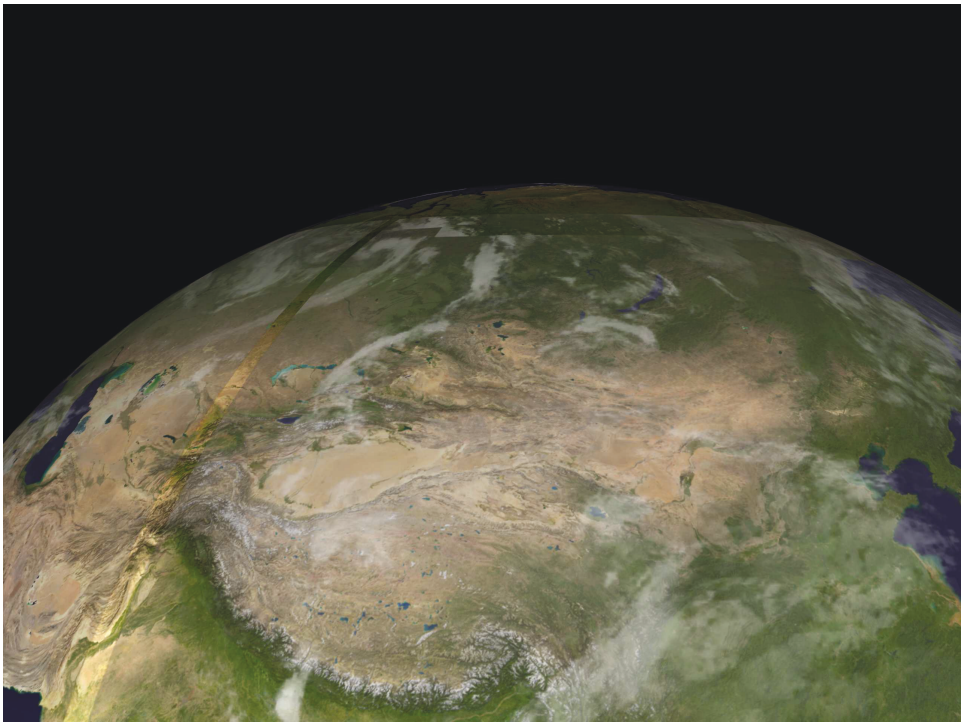

Figure 2.3: Motion of water vapor in the Earth's atmosphere above Asia collected from the Global Online Enrollment System series of Earth-observing satellites. (`svs.gsfc.nasa.gov/vis/a000000/a002600/a002652/index.html`)

of water vapor is obtained by radiosondes and satellite data. A variety of ground-based remote sensing techniques have been developed, e.g., ground-based GPS, Lidar (Light detection and ranging) (Han et al., 1994), GPS radio occultation (Wickert et al., 2005), VLBI (Very Long Baseline Interferometry) (Steigenberger et al., 2007). The focus of this work is on GPS ground-based atmosphere observations and their validation, which is described in detail in the next chapters. Instruments providing the humidity data used in this work and new techniques are described in the following sections.

2.2.1 Radiosonde

Radiosondes (RSs) are balloon-borne instruments that send temperature, relative humidity and pressure data measured along the line of the sounding to the ground station using radio signals (WMO, 2008). They can provide vertical profiles of water vapor, temperature, and pressure up to an altitude of approximately 30 km. In many countries RS networks have been set up to meet the needs of operational weather forecasting, climatological data bases, and meteorological research programmes. Nevertheless, RSs are launched typically between 1 to 4 times a day (synoptic times: 0, 6, 12, and 18 Universal Time Coordinated (UTC)). Their high cost limits the spatial (several hundred km at best) and temporal (about twice a day) resolution of the observations. Insufficient water vapor data are a major source of errors in short-term (<24h) forecasts of precipitation (Rocken et al., 1993). Time

Figure 2.4: Radiosonde from DWD (German Weather Service) carrying different sensors for LUAMI Campaign (2008).

series from weather balloons have existed since the late 1930s.[8] These long time series are used in climatology, e.g., estimating long-term trends and changes in the climate. Although advantages of in situ measurements that provide high vertical resolution are obvious, RS measurements also show very inhomogeneous effects like the use of different sensors and observation times with different evaluation strategies in different countries (Garand et al., 1992). However, RS data are the most important source of information for the numerical weather models.

2.2.2 Water vapor radiometer

Ground-based water vapor radiometers measure the background microwave radiation emitted by atmospheric water vapor and can determine the integrated water vapor content along a given line of sight with high temporal resolution (WMO, 2008). In parallel WVRs can measure the atmospheric integrated liquid water (ALW) content. To achieve the water vapor information, the sky brightness temperatures at two or more frequencies are measured (Bevis et al., 1992). However, the radiometer can be constructed with very different specifications in terms of frequency, bandwidth, integration time, angular resolution, and accuracy. The standard dual-channel WVR measures at two frequencies, one close to the 22.235 GHz water vapor line and the other in a window region at higher frequencies (e.g., 31.4 GHz) (Rose et al., 2005). The accuracy of the WVR depends on the choice of frequencies and the absolute accuracy in brightness temperatures. To determine the atmospheric water vapor, calibrations of the instrument are necessary. WVR observations cannot be

[8] `www.ua.nws.noaa.gov`

Figure 2.5: Water vapor radiometer (HATPRO) at GFZ.

determined during heavy rainfall and close to the sun because no sky brightness temperature can be measured in these cases (Pacione et al., 2001). In addition, the measurements could be blocked by the surroundings (obstacle, landforms), which should also be taken into account in the observation geometry. Furthermore, relatively few WVRs are used in the world due to the high cost.

2.2.3 Very long baseline interferometry

The VLBI technique was originally developed in radio astronomy to obtain structure of radio sources. Since the 1970s, the VLBI data has been recorded for geodetic purposes. VLBI measures the arrival time difference of signals at distant telescopes on the Earth from an astronomical radio source by cross correlation (Whitney et al., 1976). The most commonly radio sources are active galactic nuclei of type quasars or radio galaxies. From long time series of measurements, atmospheric, geodynamic, and astronomical parameters can be derived to monitor the earth rotation, the climate change and the tectonic plate motion etc. With precise positions of the radio telescopes, all the Earth orientation parameters can be determined by VLBI. In the near future, the next-generation system will have an accuracy of 1 mm in position and 0.1 mm/y in velocity (Schuh and Böhm, 2013). In geodetic VLBI approach, the atmospheric water vapor can be obtained by estimating the troposphere path delay (Heinkelmann et al., 2007). The troposphere path delay is a product of the zenith delay and an elevation-dependent mapping function, similar to GPS. VLBI antennas with a very precise surface are required to collect the weak signals from quasars. It needs a larger diameter of the antenna or larger distance between antennas because the signals weaken gradually as they travel from cosmic quasars to Earth. In addition, the structure of the telescopes has to be high mechanically stable and high slewing speed. Only a few stations are operational in the world because of its high cost to build and sustain.

2.2.4 Lidar

Light Detection and Ranging (Lidar) is a remote sensing technology that transmits laser pulses of radiation at visible or near-visible wavelengths to illuminate a target and the backscattered radiation is measured using telescopes (Andrews, 2010). Lidar sensors can be used in airborne, space borne, and ground remote sensing. The vertical distribution of water vapor in the lower atmosphere can be determined by advanced lidar methods namely the DIfferential Absorption Lidar (DIAL) and Raman lidar. The Raman lidar uses the rotational-vibration Raman scattering from water vapor and nitrogen molecules to determine the water vapor mixing-ratio profiles. The derived Raman lidar estimates have to be calibrated, e.g., with RS data. Because of low backscatter efficiency, Raman lidars are usually restricted to night-time. The water vapor DIAL uses intensive narrow-band laser pulses at two closely adjacent wavelengths, in order that water vapor will only absorb one of them (Vogelmann and Trickl, 2008). Water vapor profiles are retrieved by comparing the differential absorption in the two backscattered signals. The DIAL can also work in daytime in comparison to Raman lidar.

Lidar technique has proven to be a reliable measurement of water vapor profiles with high accuracy in the vertical (Wirth, 2012). The aerosol distribution and ozone profiles can also be obtained by the lidar technique, which are also very important for atmospheric research.[9]

2.3 Numerical weather prediction models and reanalysis data

Numerical Weather Prediction (NWP) models are computer models which combine a numerical representation of the atmospheric physics. A large variety of meteorological observations is used in order to describe the atmosphere dynamics and to compute weather forecasts. In contrast to the observation systems described so far, a NWP does not lead to new observations but provides modeled optimal combination of all available observations under the *constraint* of the atmospheric physics. These results are presented in consistent 3D fields of the atmospheric state variables which are often equally valuable for validation studies as the original observations. A number of global and regional forecast models are operated worldwide, using current weather observations from weather stations or satellite data as input. NWP models are based upon the physical laws of fluid dynamics, thermodynamics, and conservation laws. A set of differential equations is solved to estimate the temporal and spatial variation of the atmospheric state variables, such as air pressure, temperature, wind speed, and humidity. The nonlinear partial differential equations cannot be solved analytically (Strikwerda, 2007). Therefore, numerical methods are used to obtain approximate solutions. For this purpose, the temporal evolution of the model variables is computed on a regular spaced 3D grid, which stretches from the ground to upper layers of the atmosphere. The length of the time step within the model is related to the distance between two neighboring grid points and is chosen to maintain numerical stability (Pielke, 2002). The numerical effort for solving

[9] `www.nasa-usa.de/centers/langley/news/factsheets/LASE.html`

the model equations increases with the number of grid points. As the performance of even the most powerful supercomputers is limited, the resolution of the model output is restricted.

There are both high resolution regional models with horizontal resolutions between 2 km and 10 km and global models with lower resolutions between 10 km and 50 km. The global models are used for the medium-range forecasts (more than 2 days) and climate simulations (Kalnay, 2003). The regional models with higher resolution are used for short-range forecasts (1-3 days). On the other hand, the regional models need accurate boundary conditions, which are provided by the global models. Several major NWP centers e.g., in Germany (`www.dwd.de`), in the US (`www.ncep.noaa.gov`), and in the United Kingdom (`www.met-office.gov.uk`) operate global and regional models.

2.3.1 Data assimilation

A NWP needs to solve an initial value problem, i.e. the initial state of the atmosphere has to be known. In an ideal case meteorological observations would provide sufficient information. However, modern NWPs work with rather dense 3D grids consisting of more than 10^8 grid points and it is impossible to observe all state variables on each grid point. It is therefore necessary to combine model fields from the latest forecast with the current observations in order to obtain a complete set of state variables which is as close as possible to the real state of the atmosphere. This task is referred to as *data assimilation* and the atmospheric state obtained in this way is called an *analysis*. Estimating the atmospheric state from a limited number of erroneous observations leads to a similar problem as the GNSS tomography because an ill-posed inverse problem with insufficient input data has to be solved. The observations have different characteristics and an irregular distribution in space and time. Therefore, the observed data alone are not sufficient to determine the initial state, due to huge data gaps especially over the oceans, lack of knowledge about the actual humidity field and error in the observations. For example, the measured wind does not correspond exactly to the calculated temperature and air pressure from wind conditions. Inconsistent initial condition is one of the reasons why the weather forecasts are not always correct. In order to improve the forecast, data assimilation works on the basis of incomplete and potentially faulty observations in association with the use of the model forecast. It transports information from regions of dense data to poor data regions with the help of observation information from the past (Kalnay, 2003). The risk of data assimilation is that the analysis does not describe exactly the reality due to the inclusion of the prior estimates of the model state. When the prior estimates are very different from reality, analysis based on them cannot be optimal. It especially affects areas with few observations, in which the prior estimates dominate the analysis results (Stull, 2000). Various assimilation algorithms have been developed such as optimal interpolation, 3D-variational data assimilation, 4-Dimensional data assimilation (4D-Var) and ensemble Kalman filter methods.

With the increased power of super computers, the use of more accurate methods for data assimilation and more available data the numerical weather prediction will be continually improved.

2.3.2 ECMWF reanalysis data

The European center for medium-range weather forecasts (ECMWF) is an intergovernmental organization supported by 34 states.[10] The ECMWF develops and operates its own global model with a 4D-Var assimilation system. It provides operational medium- and extended-range forecasts (up to 15 days). The ECMWF also operates a data center which stores large amounts of all available global meteorological observations. Based on this huge data set, long-term model runs covering tenths of years are carried out with the latest model versions. These *reanalyzes* provide consistent global time series of past atmospheric states and are the basis for numerous investigations ranging from validation studies to climate research. Two major reanalysis ERA-15 and ERA-40 have been extensively used. The interim reanalysis project ERA-Interim is the latest global atmospheric reanalysis produced by the ECMWF, which covers the period from 1989 to present. It is a more extended reanalysis to replace the old reanalysis. The ERA-Interim products have not only better horizontal and time resolution and more experienced data quality control but also more additional parameters such as the humidity and cloud parameters.[11]

[10] `www.ecmwf.int`

[11] `www.ecmwf.int/research/era/do/get/era-interim`

3 GNSS meteorology

As discussed in previous chapters, there is a need for water vapor observations with high spatial and temporal resolution. Some techniques (e.g., RS, VLBI) have difficulties to provide data with high temporal and spatial resolution at the same time. Some (WVR, Lidar etc.) are highly dependent on weather conditions, while others may be not practical considering the poor temporal resolution, e.g., GPS radio occultation. Besides the technical aspects, economic factors have to be considered.

With this requirement, attempts were made to utilize the observations of existing geodetic GPS networks. In previous years many scientists have been interested in measuring atmospheric water vapor with tomography techniques using ground-based GPS data. However, the quality of the result can be affected by many factors (the coverage, number, and accuracy of the observations etc.). Independent observations (e.g., RS, WVR) are applied to improve the GPS water vapor tomography.

With the rapid development of the GNSS (not only GPS), atmospheric observations will be soon available for GNSS water vapor tomography. GNSS atmospheric observations have similar accuracy as conventional observations, GNSS is completely independent from the weather and time and is also very cost-efficient, requiring only GNSS receivers. Therefore, GNSS is a powerful tool to sound the atmosphere with its low cost, all-weather, near real-time, high temporal, and spatial resolution. European meteorological services, e.g., EIG EUMETNET, use GPS delays (shortly GNSS delays) and water vapor estimates for operational weather forecasts. The data are provided in near real-time by different GNSS analysis centers.

In this chapter, an overview of GNSS as well as its basic data processing principles are summarized. GNSS radio waves are influenced by the atmosphere while passing it and the meteorological quantities can be derived from GNSS observations. The methods and tropospheric models used in GNSS processing are explained. In addition, there is a short introduction about the GFZ EPOS package, which provides GNSS tropospheric products used in this study.

3.1 Overview of the GNSS

GNSS is the general name given to all navigation systems (e.g., GPS, GLONASS, Galileo, Beidou). Since the first global positioning system (Transit) developed by the American Navy in the 1960s, the new GNSS began to develop quickly and became widely applicable in different fields to determine the precise position, velocity, and time. The major GNSS systems are the American GPS and the Russian GLONASS. The European Galileo and Chinese Beidou are still in development. Other regional navigation systems in Japan, India are also planned or under development. More details about GPS are described in section 3.1.1.

GLONASS consists normally of 24 satellites. Currently there are 29 satellites in orbit.[12] All the GLONASS satellites operate at an altitude of about 19,100 km with

[12] `www.glonass-ianc.rsa.ru` (15th August 2013)

64.8 ° inclination to the equator and a revolution period of 11 h 15 min 44 s. 8 satellites are evenly spaced by an angle of 45° in each of three orbital planes. In the next generation of GLONASS, Code Division Multiple Access (CDMA) modulation is used together with Frequency Division Multiple Access (FDMA). The first modernized satellite GLONASS-M has been operational since 2003 and the first satellite of the new GLONASS-K generation has been launched in 2011. The next generation of GLONASS called GLONASS-KM is being planned. Since its Full Operational Capability (FOC) 1996, GLONASS satellites emit the standard accuracy signal modulated onto the carrier frequency G1 (1602 MHz) and the high-accuracy signal modulated on two carrier frequencies G1 and G2 (1246 MHz). A standard-accuracy signal has been added to G2 since GLONASS-M satellites. In addition, the GLONASS-K satellites will provide a third carrier frequency G3 (1204.704 MHz).

Galileo, which is built by the European Commission and European Space Agency, is the first global positioning system under civilian control. A full constellation of 30 Galileo navigation satellites (27 operational and 3 spare) in Medium Earth Orbit (MEO) at an altitude of 23,222 km will be evenly spaced in three orbit planes with 56° inclination to the equator and an orbit period of one revolution equal 14 h 4 min 45 s. The first four in-orbit validation satellites were launched on October 21, 2011 and October 12, 2012 respectively. The two latest satellites will be launched in the summer of 2014.[13] Different services will be provided by Galileo such as the free open service, the commercial service, Public Regulated Service, and the Search and Rescue service.

The Chinese Beidou is planning to offer services on a global scale with 37 satellites (5 geostationary + 27 MEO + 5 inclined geosynchronous) around 2020. The five geostationary satellites are located at longitude 58.75°E, 80°E, 110.5°E, 140°E, and 160°E. The inclined geosynchronous orbit satellites have an altitude of 35,785 km with 55° inclination. The 27 (24 operation + 3 spare) MEO satellites will have an average altitude of 21,500 km in three orbital planes with 55° inclination. 14 satellites are operational now, covering central Asia and China. More details about the Beidou system can be found online at `www.beidou.gov.cn`.

Currently up to 12 GPS satellites can be observed simultaneously in Europe. When fully operational (GPS, GLONASS, and Galileo), the number of the observed satellites can be increased to about 30 (even 40 including Beidou) in the future. For the 3D humidity field derived from GNSS observations the increasing number of GNSS satellites and ground stations will lead to a more homogeneous coverage of tropospheric slant paths in space and time.

3.1.1 GPS introduction

GPS was originally developed to provide position and time information for navigation and timing. Over the past 20 years, applications of GPS technologies have been developed in many other areas such as plate tectonics, deformation of the Earth crust, glaciology, the determination of the electron density of the ionosphere

[13] `www.esa.int/Our_Activities/Navigation` (May 07 2014)

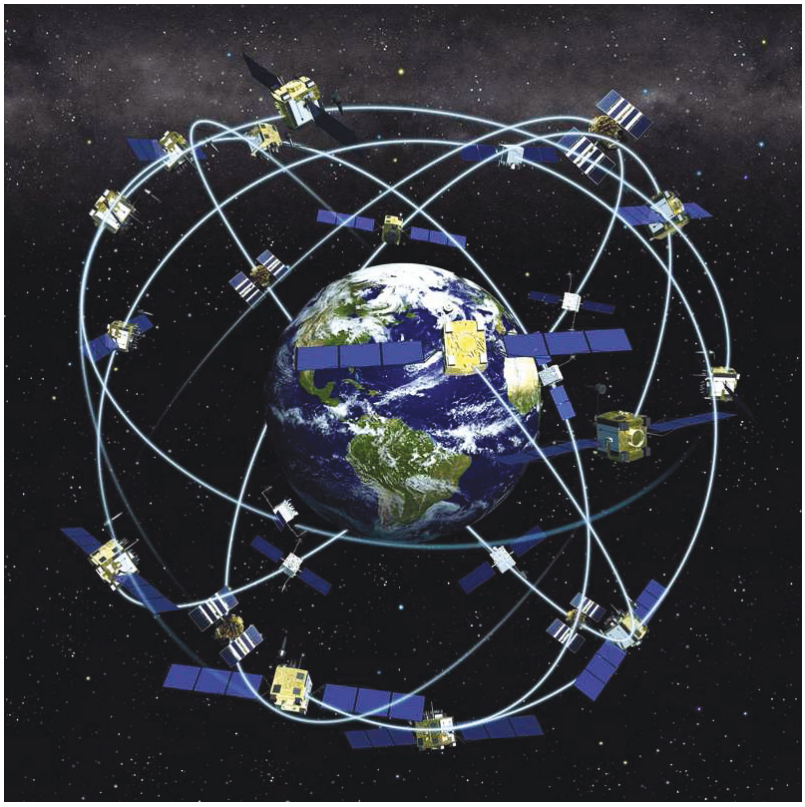

Figure 3.1: GPS satellite constellation. (`www.insidegnss.com/aboutgps`)

for space weather, monitoring of ocean surface with GNSS Reflectometry and GNSS meteorology.

GPS is based on a constellation of 32 satellites in orbit with an altitude of approximately 20,200 km.[14] Its FOC was achieved in 1995 with 24 operational satellites, which are arranged into six equally-spaced orbital planes with a 55° inclination (Fig. 3.1). The orbit period is approximately 11 h 58 min. Because of the limited life span of satellites, the GPS modernization process started with the launch of the first Block IIR-M satellite in September 2005. Since then a second civilian signal (L2C) is transmitted for enhanced system performances. Moreover, the first GPS Block IIF satellite was launched in May 2010 with a third civil signal (L5C). The next generation of GPS Block III is currently under development. Recently, 31 operational GPS satellites are in orbit. The orbital configuration ensures that at least four satellites are observed at anytime and anywhere on the Earth surface, as this is required for the determination of the point position and the receiver clock correction.

To ensure the health and accuracy of the satellite constellation, the GPS control segment is operational continuously (Fig. 3.2). It consists of a Master Control Station (MCS), an alternate MCS, 12 command and control antennas, and 16 monitoring stations. The monitoring stations track all satellites as they pass over, collecting code/carrier measurements, navigation signals, and atmospheric data. These data are received by the MCS and utilized to compute the satellite orbit. Finally, the

[14] `www.gps.gov/systems/gps/space` (August 16, 2013)

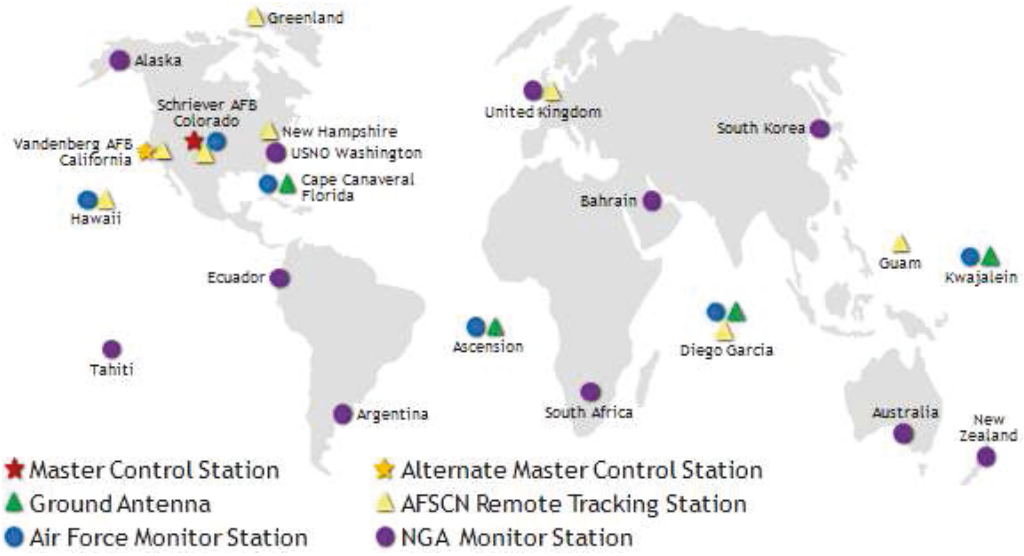

Figure 3.2: GPS control segment. (`www.gps.gov/systems/gps/control`)

MCS generates the navigation data message and upload it to the satellite via ground antennas.

The user can receive the satellite-transmitted signals with a GPS receiver. Based on these signals, the position of the receiver could be calculated. The principles of GPS measurements as well as the basics of GPS processing are present in the following sections. In the following chapters, important terminology and associations are explained in more depth.

3.1.2 Basic GPS observations

GPS satellites transmit signals on three carrier frequencies L_1 ($f_1 = 1575.42\,\text{MHz}$), L_2 ($f_2 = 1227.60\,\text{MHz}$), and L_5 ($f_5 = 1176.45\,\text{MHz}$), which are modulated by the chip sequences called PseudoRandom Noise (PRN) codes. The chip sequences are binary values (zeros and ones) with random character, but which can be identified clearly (Seeber, 2003). Each GPS satellite is equipped with a high accurate atomic clock with a fundamental frequency of 10.23 MHz. The GPS carrier frequencies are derived as integer multiple of this fundamental frequency. The measured distance between the satellite and the receiver on ground is defined as the pseudorange. The pseudorange from code measurements could be calculated from measured travel time of the signal from the satellite s to the receiver r (Teunissen and Kleusberg, 1998). Besides the clock corrections of the satellite and receivers (δt^s, δt_r), there are other error sources, such as the ionospheric correction ($\delta^s_{r,ion}$) and tropospheric correction ($\delta^s_{r,trop}$) in the pseudorange:

$$P^s_r = \rho^s_r - (\delta t_r - \delta t^s) \cdot c + \delta^s_{r,ion} + \delta^s_{r,trop} + \xi \tag{3.1}$$

where c denotes the speed of light in vacuum and ξ are the remaining terms (e.g., measurement noise, multipath delay, the relativity correction, and the receiver- and satellite hardware biases). δt^s can be modeled by a polynomial with the coefficients

determined by the control segment being transmitted in the navigation message. δt_r is unknown and must be determined for each observation epoch. The instrumental accuracy of measurements is up to 1 % of the chip length, therefore, it depends on the code type used and is of the order of dm (Hofmann-Wellenhof et al., 2008).

On the other hand, the instrumental accuracy of the carrier phase measurement is assumed to be better than 1 % of the wavelength and is of the order of 1.5 mm level (Hofmann-Wellenhof et al., 2008). The phase difference between the receiver carrier wave and a reference carrier generated in the receiver can be expressed in cycles:

$$\Phi_r^s(t_r) = \frac{\rho_r^s}{\lambda} + f \cdot (\delta t_r - \delta t^s) + N_r^s - \frac{\delta_{r,ion}^s}{\lambda} + \frac{\delta_{r,trop}^s}{\lambda} + \frac{\xi}{\lambda} \tag{3.2}$$

where N_r^s denotes the initial carrier phase ambiguity term, which is an integer number of wavelength. λ is the carrier wavelength. The frequency f and the wavelength λ have the relation of $c = \lambda \cdot f$. Multiplying the above equation by λ the carrier phase measurement is expressed in units of meter:

$$L_r^s(t_r) = \rho_r^s + c \cdot (\delta t_r - \delta t^s) + \lambda \cdot N_r^s - \delta_{r,ion}^s + \delta_{r,trop}^s + \xi. \tag{3.3}$$

It should be noted that the sign of the ionospheric correction in code and carrier phase is opposite. It is because of the time delay of the code sequence (group velocity with which energy travels) and of the phase advance (phase velocity) in the dispersive ionosphere (Leick, 2004).

3.1.3 Linear combination

The basic GPS observables are the code and the carrier phase. A major part of the GPS errors and biases can be removed by linear combinations of the GPS dual frequency observables. With two carriers (f_1, f_2) and one code modulated on each of the two carriers, the code ranges P_1, P_2, and the carrier phases L_1, L_2 could be measured. There are many different linear combinations such as the geometry-free combination, the Wide-lane combination, and the Narrow-lane combination. The ionosphere-free combination is introduced as an example (see Eqs. 3.4). In Eq. 3.1/3.3 the first order (up to 99.9 %) ionospheric effect on the GPS observables can be largely mitigated by the ionosphere-free combination:

$$\begin{aligned} L_3 &= \frac{1}{f_1^2 - f_2^2} \cdot (f_1^2 L_1 - f_2^2 L_2) \\ &= \rho_r^s - c \cdot (\delta t_r - \delta t^s) + \frac{c \cdot f_1 \cdot N_{r,1}^s - c \cdot f_2 \cdot N_{r,2}^s}{f_1^2 - f_2^2} + \delta_{r,trop}^s + \xi_{L_3} \\ P_3 &= \frac{1}{f_1^2 - f_2^2} \cdot (f_1^2 P_1 - f_2^2 P_2) = \rho_r^s - (\delta t_r - \delta t^s) \cdot c + \delta_{r,trop}^s + \xi_{P_3}. \end{aligned} \tag{3.4}$$

Typically, the Precise Point Positioning (PPP) technique uses code and carrier phase measurements in the ionosphere-free combination to remove the ionospheric delays. However, its negative effect is the higher noise of the combined observations L_3. Another disadvantage is that integer nature of carrier phase ambiguity is lost and

no direct integer solution for the combined ambiguity fixing exists. The GPS data processing package EPOS uses the L_3 combination to estimate the tropospheric delay as well as station coordinates and receiver clock biases (see section 3.4 for details).

3.1.4 Precise point positioning

As described in section 3.1.2, the positioning accuracy is limited by the accuracy of satellite orbits and clocks and the ionospheric and tropospheric corrections. The PPP (Zumberge et al., 1997) uses the undifferenced observations with code and carrier phase and provides precise products. PPP has been widely used in different areas such as the crustal deformation monitoring (Hammond and Thatcher, 2005; Calais et al., 2006), in the determination of low Earth satellites orbits (Zhu et al., 2004), for the precise positioning of mobile objects (Zhang and Andersen, 2006) and also in the near real-time GNSS meteorology (Rocken et al., 2005).

The precise satellite orbit and satellite clock corrections for PPP are provided by the International GNSS Service (IGS). Among all the products, the final product has the best quality but it is only provided with a delay of some few days. Therefore, the most accurate PPP can be achieved in post-processing mode using the final products. The remaining errors are the receiver clock error, the tropospheric delay and the ambiguities, which could be solved by a sequential least squares adjustment or Kalman filtering.

The tropospheric products could also be generated by network solution using undifferenced observations where satellite clocks are estimated as additional parameters (Ge et al., 2006). Compared to the PPP, the network solution needs long processing time but precise satellite clocks are not required as a pre-condition. The PPP approach has the advantage of reducing the effects due to systematic error at a reference site inherent to the network solutions (Emardson et al., 2000) as it does not need to take the correlation between stations into account, i.e., the solution of each station is independent. Therefore, it allows GPS processing of hundreds or thousands stations in parallel because the processing time increases only linear with the number of stations (Seeber, 2003).

3.1.5 Differenced observations

An alternative to the PPP is the relative positioning method based on double difference observations. Here, the errors can be largely mitigated by forming differences between observations or linear combinations. Thereby, the common information presents in the undifferenced observations can be eliminated or reduced. The differences between observations from stations or satellites or epochs can be built (Fig. 3.3).

The single difference and the double difference are commonly used. The single difference is the difference of the signals at two stations k and l observing the same

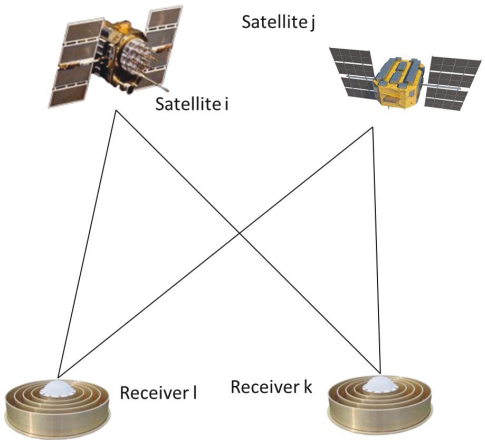

Figure 3.3: Double difference method with observations at receiver l and k from GPS satellites i and j.

satellite i:

$$\begin{aligned} \Delta L^i_{kl} &= L^i_k - L^i_l = \Delta\rho^i_{kl} + c\cdot\Delta\delta t_{kl} - \Delta\delta^i_{kl,ion} + \Delta\delta^i_{kl,trop} + \lambda\cdot\Delta N^i_{kl} + \xi^i_{kl} \\ \Delta P^i_{kl} &= P^i_k - P^i_l = \Delta\rho^i_{kl} + c\cdot\Delta\delta t_{kl} + \Delta\delta^i_{kl,ion} + \Delta\delta^i_{kl,trop} + \xi^i_{kl}. \end{aligned} \tag{3.5}$$

In Eqs. 3.5 the satellite clock error terms are eliminated. Ionospheric and tropospheric effects can be canceled or largely reduced by forming the single difference, especially for neighbored stations (Xu, 2007). The distance between two stations is referred to as the baseline. The double difference is the difference of two single differences related to two observed satellites i and j and receivers k and l as:

$$\begin{aligned} \nabla\Delta L^{ij}_{kl} &= \Delta L^i_{kl} - \Delta L^j_{kl} = \nabla\Delta\rho^{ij}_{kl} - \nabla\Delta\delta^{ij}_{kl,ion} + \nabla\Delta\delta^{ij}_{kl,trop} + \lambda\cdot\nabla\Delta N^{ij}_{kl} + \xi^{ij}_{kl} \\ \nabla\Delta P^i_{kl} &= \Delta P^i_{kl} - \Delta P^j_{kl} = \nabla\Delta\rho^{ij}_{kl} + \nabla\Delta\delta^{ij}_{kl,ion} + \nabla\Delta\delta^{ij}_{kl,trop} + \xi^{ij}_{kl}. \end{aligned} \tag{3.6}$$

In Eqs. 3.6 the satellite clock error as well as the receiver clock error is eliminated. The GPS measurements are usually stored in the receiver and later these data can be merged with observations recorded at a reference receiver using a post-processing software. Double differences are commonly used for remote sensing of atmospheric water vapor due to their high accuracy results with integer ambiguity fixing. However, only relative observations with code and carrier phase are used in the double difference methods and a correlation between stations exists. A baseline longer than 500 km is necessary to reduce the correlation between the estimated parameters or sophisticated decorrelation technique must be applied (Xu et al., 2013; Jin et al., 2010). The EPOS is based on undifferenced observations, but with double difference observations used for ambiguity fixing.

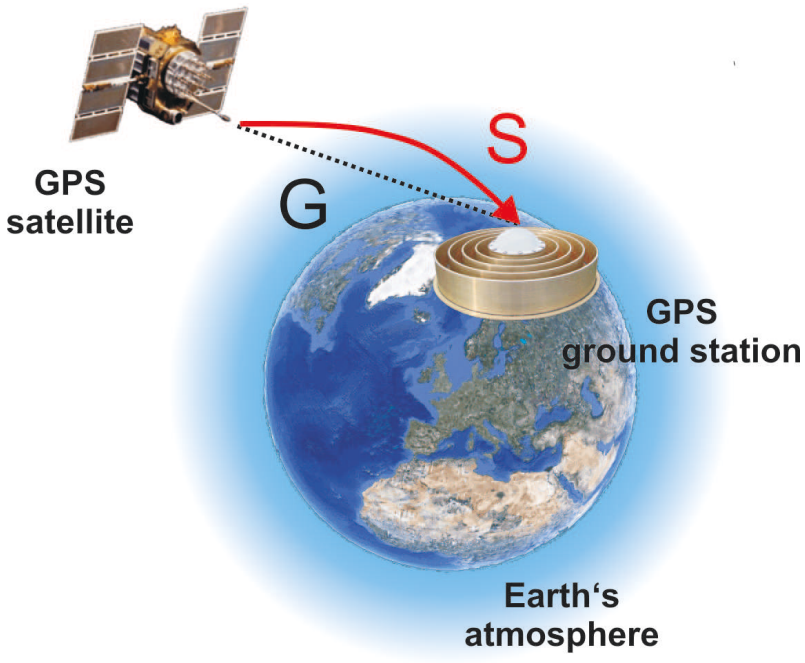

Figure 3.4: Ray bending in the atmosphere. S is the actual signal path and G is the geometric path.

3.2 Propagation of radio waves in the atmosphere

The propagation of radio signals in the atmosphere is related to the refractive index. The time difference, between the signal travel with and without atmosphere, is called path delay. Unlike dispersive ionosphere delay eliminated by combination of several frequencies, the troposphere delay cannot be eliminated due to the non-dispersive character of the troposphere. The delay caused by the neutral atmosphere is denoted as the tropospheric path delay:

$$\delta_{trop} = \int_S n ds - \int_{S_0} ds = \int_S (n-1) ds + (\int_S ds - \int_{S_0} ds) \tag{3.7}$$

where S is the signal path, S_0 is the geometric path, and n is the tropospheric refraction index. The first term is the microwave delay caused by the slower propagation and the second term is the geometric delay caused by the ray bending (Fig. 3.4). The S is again the actual signal path, G is the geometric path, and the geometric delay equals (S-G). Instead of the small n, the refractivity N is used ($N = (n-1) \cdot 10^6$). As a consequence, the equation turns into:

$$\delta_{trop} = 10^{-6} \int N ds + (S - G). \tag{3.8}$$

The tropospheric delay depends on the pressure, humidity, and temperature. It can be split into a hydrostatic (dry) and non-hydrostatic (wet) part. About 90 % of the tropospheric delay is caused by the dry air. The wet delay depends on the water vapor.

$$\delta_{trop} = 10^{-6} \int (N_h + N_w) ds + (S - G) \tag{3.9}$$

The geometric delay is much smaller than the first term and the significant geometric delay occurs only at low elevation angles (below 10°) (Mendes, 1998) whereas at the zenith it is about zero. The tropospheric path delay approximates the integration of the first term. According to Smith and Weintraub (1953) and Davis et al. (1985), the wet and hydrostatic component can be expressed as:

$$N_h = k_1 \frac{P_d}{T} \tag{3.10}$$

$$N_w = k_2 \frac{e}{T} + k_3 \frac{e}{T^2} \tag{3.11}$$

where P_d and e are the partial pressures of dry air and water vapor, respectively and T is the absolute temperature. The physical constants k_1, k_2, and k_3 are empirically determined (Bevis et al., 1994):

$$k_1 = 77.60\,\mathrm{KhPa}^{-1}, k_2 = 70.4\,\mathrm{KhPa}^{-1}, k_3 = 373,900\,\mathrm{K}^2\mathrm{hPa}^{-1}.$$

GNSS uses radio waves from GNSS satellites to determine the tropospheric path delay. In this thesis, the main focus is laid on the tropospheric delays from GPS signals.

3.3 Tropospheric delay models

The GPS signal delay along each single satellite receiver path is called Slant Total Delay (STD). It can be separated into the Slant Hydrostatic Delay (SHD) and the Slant Wet Delay (SWD), which is estimated using mapping functions and the zenith delay:

$$STD = SHD + SWD = m_h \cdot ZHD + m_w \cdot ZWD \tag{3.12}$$

where m_h and m_w are the hydrostatic and wet mapping functions, respectively. The Zenith Hydrostatic Delay (ZHD) and Zenith Wet Delay (ZWD) are the delays caused by the hydrostatic part and water vapor in zenith direction.

Based on this model, the STD derived from the GPS signal can be expressed as a combination of different estimates (Bender et al., 2011a):

$$STD = m_h \cdot ZHD + m_w \cdot [ZWD + \cot(\epsilon)(G_N \cos(\alpha) + G_E \sin(\alpha))] + \delta \tag{3.13}$$

where G_N and G_E are the delay gradient parameters in the northern and eastern direction. ZHD and ZWD are the hydrostatic and wet zenith delay, m_h and m_w are the hydrostatic and wet mapping functions, ϵ is the elevation angle, α is the azimuth and δ is the postfit phase residual.

3.3.1 Mapping functions

The mapping function depends on the elevation angle ϵ. A simple mapping function is given by:

$$m = \frac{1}{sin(\epsilon)}. \tag{3.14}$$

The predominantly used mapping functions is the Niell Mapping Function (NMF), which is expressed by the latitude ϕ, height Above Sea Level (ASL) h, the elevation angle ϵ of the observing site and time t:

$$m = \frac{1 + \frac{a}{1+\frac{b}{1+c}}}{\sin(\epsilon) + \frac{a}{sin(\epsilon)+\frac{b}{\sin(\epsilon)+c}}} + h\Delta m(\epsilon) \tag{3.15}$$

where the coefficients a, b, c and $\Delta m(\epsilon)$ differ for the wet mapping function and hydrostatic mapping function, which can be found in Niell (1996). For the hydrostatic mapping function the parameter a at ϕ and t can be calculated as follows:

$$a = a_{avg}(\phi) + a_{amp}(\phi) \cdot \cos(2\pi \frac{t - T_0}{365.25}) \tag{3.16}$$

where T_0 is the adopted phase shift of 28 days, which is obtained when all data from the northern hemisphere were fit together, and $a_{avg}(\phi)$ and $a_{amp}(\phi)$ are linearly interpolated from tabulated values. Parameter b and c can be calculated in the same way. The height corrections for the hydrostatic mapping function is given by:

$$\Delta m(\epsilon) = \frac{1}{\sin(\epsilon)} - \frac{1 + \frac{a_{ht}}{1+\frac{b_{ht}}{1+c_{ht}}}}{\sin(\epsilon) + \frac{a_{ht}}{sin(\epsilon)+\frac{b_{ht}}{\sin(\epsilon)+c_{ht}}}}. \tag{3.17}$$

All tabular values a_{ht}, b_{ht}, and c_{ht} are described by Niell (1996). The disadvantage of the NMF is the assumption of antisymmetric southern and northern hemispheres in time.

The best description of the spatial and temporal distribution of atmospheric temperature and humidity is provided by NWP models (see section 2.3). Recent developments of determining the mapping function coefficients a, b, and c use information from global NWP models. The Vienna Mapping Function (VMF) (Böhm and Schuh, 2004), based on the analysis of VLBI data optimizes the determination of the mapping function coefficients from the European Center for Medium-range Weather Forecasts (ECMWF) model data. The VMF is available in near real-time as time series of coefficients a, b, and c with a temporal resolution of six hours.

An alternative to the NMF and VMF is the Global Mapping Function (GMF). The coefficients of the GMF are obtained from spherical harmonics of the VMF parameters on a global grid (Böhm et al., 2006). Similar to NMF, the GMF requires only the station coordinates and the yearly day as input parameters. The regional height biases and annual errors of the NMF are significantly reduced with the GMF. However, the accuracy of the GMF is lower than that of the VMF.

3.3.2 Zenith delays

To obtain the ZHD in Eq. 3.12, different models can be used. Most of them have no significant difference by just choosing different refractivity constant. Therefore, only two important modeling strategies were introduced here. The most commonly

used model for the ZHD was introduced by Saastamoinen (1972), which is indicated in the following formula (Davis et al., 1985):

$$ZHD = \left(0.0022768 \pm 0.00000059 \, \frac{\mathrm{m}}{\mathrm{hPa}}\right) \frac{P_0}{1 - 0.0026\cos(2\phi) - 0.00028\,\mathrm{km}^{-1}h} \tag{3.18}$$

where P_0 is the surface pressure in hPa and h is the height ASL in meter.

Another choice for the ZHD is the Hopfield model (Hopfield, 1969), which uses a quartic model:

$$ZHD = 77.6 \cdot 10^{-6} \frac{P_0}{T_0} \frac{40136 + 148.62(T_0 - 273.15)}{5}. \tag{3.19}$$

The ZHD is computed as a function of the surface temperature T_0 in K and pressure P_0 in hPa. The two models differ in the gravity modeling and the choice of the refractivity parameter.

The ZWD, which is much smaller than the ZHD, varies generally much stronger in space and time. For this reason it is more difficult to determine. Most of the models are based on the analysis of RS ascents. A commonly used model for ZWD is the Saastamoinen model (Saastamoinen, 1972):

$$ZWD = 0.0022768 \, \frac{\mathrm{mK}}{\mathrm{hPa}} \cdot \frac{(\frac{1255}{T_0} + 0.05)e_0}{1 - 0.0026\cos(2\phi) - 0.00028\,\mathrm{km}^{-1}h} \tag{3.20}$$

where e_0 is the surface partial pressure of water vapor in hPa.

Due to the complexity to get high accurate ZWD it is usually considered as an unknown parameter in the GPS processing. Then, the ZWD or SWD is calculated using the following equations:

$$ZWD = ZTD - ZHD \tag{3.21}$$
$$SWD = STD - SHD. \tag{3.22}$$

3.3.3 Derived quantities

According to Bevis et al. (1994) the SWD/ZWD can be converted into SIWV/IWV:

$$IWV = \Pi \cdot ZWD \tag{3.23}$$
$$SIWV = \Pi \cdot SWD \tag{3.24}$$

where the conversion parameter Π is a function of the weighted mean temperature of the atmosphere (T_m):

$$\Pi = \frac{10^6}{\rho R_v (\frac{k_3}{T_m} + k_2')}. \tag{3.25}$$

In Eq. 3.25 following parameters are used:

$$
\begin{aligned}
R_v &= 461.525\,\frac{\mathrm{J}}{\mathrm{kgK}} \text{ the specific gas constant for water vapor} \\
k_2' &= 22.1\,\mathrm{KhPa}^{-1}, k_3 = 373900\,\mathrm{K}^2\mathrm{hPa}^{-1} \text{ are the empirical parameters} \\
\rho &= 1000\,\mathrm{kgm}^{-3} \text{ is the density of liquid water} \\
T_m &= 70.2 + 0.72 \cdot T_0 \text{ is the weighted measured temperature.}
\end{aligned}
$$

T_m is estimated from the surface temperature T_0. The error of T_m is about 4.7 K, which corresponds to a relative error of less than 2 % by analyzing a data set of 8718 RS profiles in two years from 13 stations in the US (Bevis et al., 1992). SIWV gives the amount of water vapor along the signal path. SIWV in the zenith direction is referred as IWV. The Precipitable Water Vapor (PWV) is the IWV scaled by the density of water.

3.4 Tropospheric products estimated using EPOS at GFZ

Nowadays, there are several GPS software packages like GAMIT (Herring et al., 2010), Bernese (Dach et al., 2007) and GIPSY (Zumberge et al., 1997) available for geodetic and atmospheric applications. At GFZ, EPOS (EPOS-8) (Gendt et al., 1998) was developed to process GPS undifferenced observations. An overview of the main components of EPOS is shown in Fig. 3.5. The PPP function of EPOS is used for this study because of its efficient analysis of GPS data from a large number of stations. ZTD, STD, and IWV are tropospheric products of EPOS. ZTD and IWV data have been available from the GFZ since 2002 with an accuracy of 6-13 mm and 1-2 mm, respectively (Gendt et al., 2004). Since 2007, STDs are available with a sampling rate of 2.5 min providing 6-12 GPS slant delays per station and epoch. Currently there are about 300 stations from Germany and neighboring countries which are operationally processing water vapor information resulting in hourly data sets of about 50,000 STDs. The data records are collected and processed with a total delay of up to 1.5 hours at GFZ in near real-time.

GPS data

In the data preprocessing the Receiver Independent Exchange Format (RINEX) raw data from GPS stations with a sampling rate of 30 seconds is checked and prepared for the analysis. The cut-off elevation angle of 7° is used to select the data. A regional network, with about 300 GPS stations in Germany, was set up in previous years (Fig. 3.6). Most stations belong to the network Satellite Positioning Service of the German Land Surveying Agencies (SAPOS) (`www.sapos.de`) and some stations from the German Federal Agency for Cartography and Geodesy (BKG). For these stations (Fig. 3.6) the tropospheric products are generated.

Meteo data

As shown in Fig 3.5 the meteorological surface data (pressure, temperature, and relative humidity) at the stations are necessary for the conversion of the tropospheric

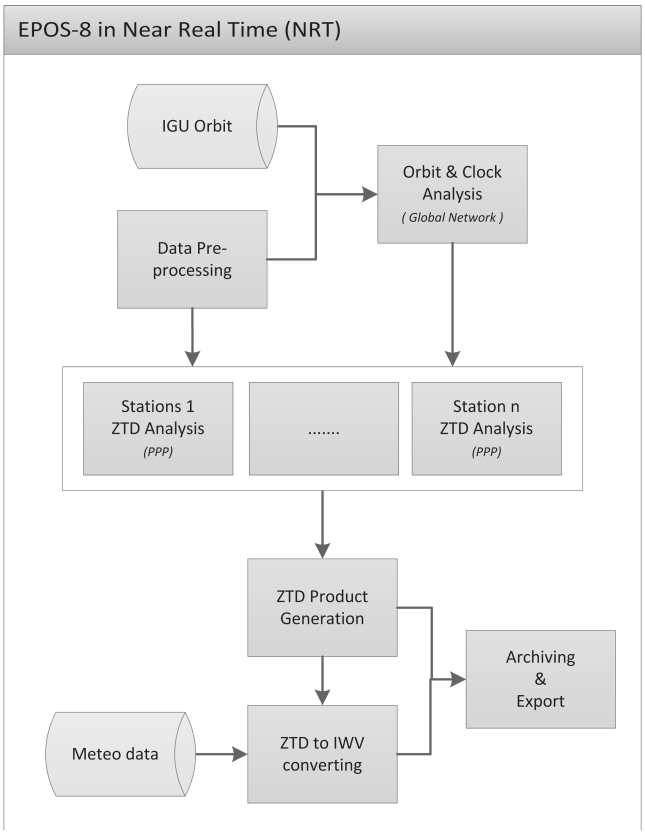

Figure 3.5: Flow diagram for the main components of the EPOS (Deng et al., 2012).

delays into IWV. For some stations equipped with meteosensors, precise measurements (meteorological data with a sampling rate of ten minutes) are available. For most stations the necessary pressure and temperature data have to be interpolated, using the hourly synoptic data of about 2,000 sites (as of 2012) provided by the German Weather Service (Deutscher Wetterdienst) (DWD). For each site the smallest surrounding station triangle is used for a linear interpolation, with corrections for the height difference. The pressure and temperature can be interpolated with an error of ± 1 hPa and ± 1 K.

Tropospheric product generation

EPOS parameter estimation is based on least squares adjustment of undifferenced code and carrier phase observations with proper weights scaled according to the observation elevation. PPP mode is used to retrieve ZTD, IWV, and STD products for each station. Corrections such as tidal effects are modeled according to the current International Earth Rotation and Reference Systems Service (IERS) conventions 2003 (`www.iers.org`) and ocean loading effects are modeled at all stations based on FES2004.[15]

Tropospheric delays are corrected using the Saastamoinen model for the ZTD and the mapping function (GMF and earlier NMF). The remaining tropospheric impact is parameterized as a stochastic process with zenith delays every 15 min at each

[15] `www.aviso.oceanobs.com/en/data/products/auxiliary-products/global-tide-fes2004-fes99/description-fes2012.html`

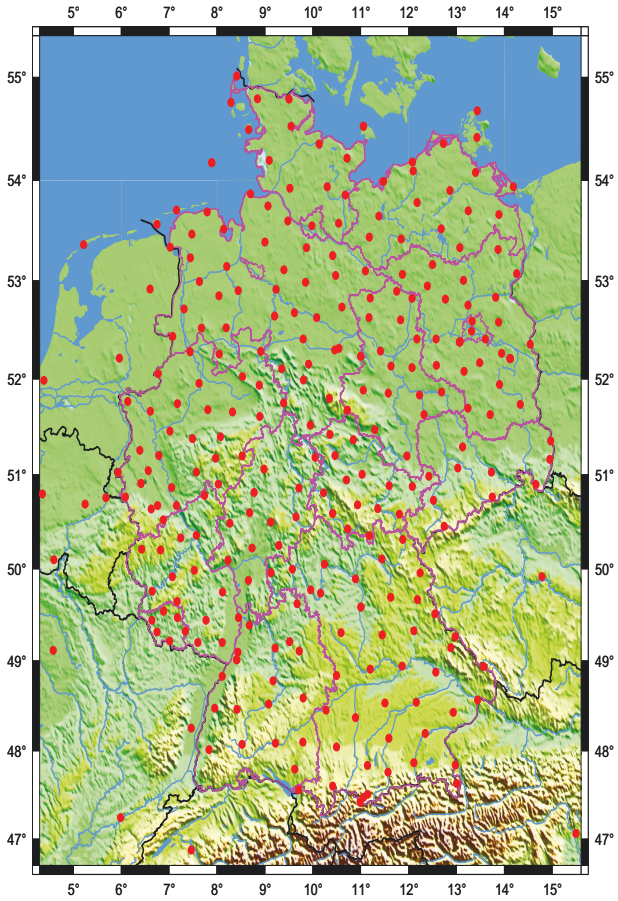

Figure 3.6: Map with 353 GPS receiver sites (red dots) in Germany (as of 2013). The violet lines indicate the borders of the 16 German federal states. The majority of the stations (about 270) is operated by SAPOS.

station and to be estimated in the data processing. Because the antisymmetric mapping function in the southern and northern hemispheres, the estimated gradients are used to determine the tropospheric gradient. Gradients in east and north direction are estimated every hour. The data are processed using a 12 hour sliding window shifted with one hour steps. With the additional meteorological data the estimated ZTDs can be converted to IWVs. Tropospheric products are produced by EPOS in both near real-time and post-processing mode. For the near real-time clock estimation the IGS ultra-rapid products are used as base and are improved by making use of some permanent stations around Germany. The IGS products provide satellite orbits and clocks based on the data of the global stations. Using IGS products as a pre-condition and the data from permanent stations of German sites, the satellite clock can be calculated with a better accuracy particularly for German regions. The stations are scheduled in different processes or computers and processed parallel. As soon as the IGS final products are available, the data are also analyzed in a post-processing mode using daily data batches to obtain the products with the highest accuracy.

4 GPS slant validation experiments with WVR observations

As shown in Fig. 3.6, a dense network of GPS receivers is operated by SAPOS in Germany. For each station, STD observations are calculated and stored with the elevation and azimuth angles of all visible GPS satellites. The derived STDs can be used by the water vapor tomography and for data assimilation in numerical weather models. Therefore, the accuracy of STDs is important for the quality of the reconstructed 3D humidity field. However, the GPS processing provides limited information about the accuracy of STD and independent observations are required to evaluate it. In this chapter, results of the comparison and evaluation of measurements of the SIWV derived from GPS-STDs and WVR are described and discussed.

4.1 Data sources

To validate the quality of the GPS-STD, the GPS derived SIWVs are compared with the corresponding WVR observations at the station GFZ0 in the Murg Valley (Murgtal) Black forest from October 5 to December 31, 2007. The observations used here were obtained in the Black Forest low-mountain regions in southwestern Germany in 2007 and are within the framework of the Convective and Orographically induced Precipitation Study (COPS) (Wulfmeyer et al., 2008). GFZ provided continuous series of GPS data and observations of temperature, pressure and humidity to the meteorological community during COPS. COPS applied a unique combination of in situ and remote sensing instruments to study convective and orographically induced precipitation in 2007.[16] By making use of these data the observations from different experiments are an ideal source for validation studies to check the consistency.

WVR

The 14-channel microwave radiometer HATPRO (Humidity and Temperature Profiler) was collocated with the GPS receiver GFZ0 (48.54°N, 8.40°E, 511.0 m ASL) in 2007 and it was operated by the University of Cologne . The data were processed and supplied to the GFZ. The HATPRO is an instrument to identify the spatial and temporal distribution of clouds and water vapor. The technical specifications and calibration methods of the HATPRO are described by Rose et al. (2005). The derived SIWV and ALW accuracies are better than 0.7 kg/m^2 and 20 g/m^2, respectively (Kneifel et al., 2009). The HATPRO, which was placed 2 m higher than the GPS station antenna, performed continuously full hemispheric scans of SIWV and ALW with 10° steps in azimuth and 10.8° steps in elevation. The observations below an elevation angle of 14.4° were not used due to the orography. The scanning began with azimuth angle 180° and elevation angle scan from 14.4° to 90°. Then the azimuth angle was changed to 170° and an elevation angle scan began from 90° back to 14.4°. The same elevation scans (14.4° - 90° - 14.4°) were repeated for each azimuth step of 10° from 180° to 0° and forward from 350° back to 180°. The

[16] www.cops2007.de

scanning sequence for one whole scan can be seen in Fig. 4.1. The duration for one whole hemisphere scan varied from 11 min to 23 min. Due to calibration problems on November 14, the data were lost.

GPS

The German GPS network was temporarily extended with a considerably number of stations in the COPS region in 2007. For the COPS period the GPS data were carefully reprocessed with a temporal resolution of 2.5 min for STDs and 15 min for ZTDs and IWVs by GFZ. The quality of the available data and the remaining gaps were analyzed carefully during the reprocessing and afterward most gaps in the time series could be filled. As a result, a considerably extended data set of all available GPS stations in the COPS region from June 2007 to November 2007 is available. The data of the station GFZ0 from this reprocessed data set are used for the validation study. The GPS receiver at the station GFZ0 is located at (48.54°N, 8.40°E, 508.83 m ASL).

Interpolation

To compare GPS and WVR data, the SIWV taken along the same line of sight is required. However, there are only few observations with the same elevation and azimuth available from GPS and HATPRO. Therefore, an interpolation of WVR data is used for the comparison. Before the interpolation is carried out, the WVR data are mapped to the zenith direction with the wet GMF:

$$IWV_{z,WVR} = \frac{SIWV_{WVR}}{m_w}. \tag{4.1}$$

As can be seen in Fig. 4.1, the scanning began with the azimuth angle 180° and the elevation angle 14.4°. The scanning sequence consisted of elevation scans (14.4° - 90° - 14.4°) which repeated for each azimuth step of 10°. However, not all the data are suitable for the comparison. Most gaps at low elevation angles in the scanning are caused by obstacles and orography (Fig. 4.1). The observations around the sun position must be omitted, because the sun could considerably exaggerate the signals. Furthermore, the WVR data points with an large ALW were not used. ALW is an important observation measured by WVR and it has an effect on the measurement of WVR (Crewell and Löhnert, 2007). If the ALW is too large, ALW can distort the measurement of the brightness temperature. As a consequence, the measured WVR-SIWV can be extremely high (Fig. 4.2). In addition, a shortcoming of the WVRs data quality can also be caused by the deleterious effect of rain or condensation of water on the optics, which causes erroneous brightness temperatures. These lead to the extremely high values of measured water vapor observations during periods of rain or clouds (Niell et al., 2001). In order to exclude influences from clouds or rain, only cases with ALW smaller than 1 kg/m^2 are used for all comparisons. On the other side, GPS is essentially insensitive to liquid water (Solheim et al., 1999). Consequently, ALW cannot be observed by GPS.

In total about 22.3 % of the original WVR data are rejected because of environmental influences (e.g., obstacle, orography, and rainfall). When the GPS observations are located in such gaps, the WVR data are not interpolated for validation.

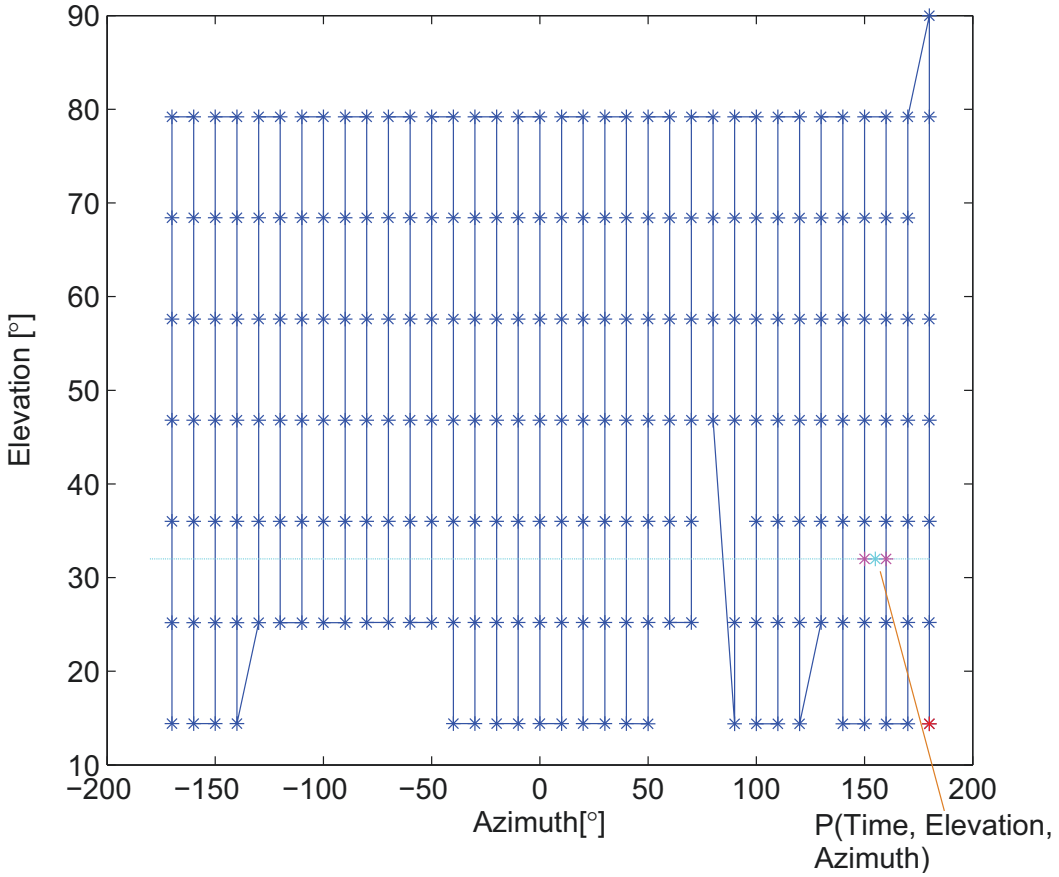

Figure 4.1: Interpolation of WVR-SIWV derived IWV_z. The scanning sequence follows the blue line and the red point is the start point of the scan. P is the interpolated point with the time, elevation, and azimuth of measured GPS data.

For every measured GPS observation information with given time, elevation, azimuth a SIWV is available. As an example, for one GPS measured observation (point P in Fig. 4.1) the WVR-SIWV is interpolated in several steps:

1) For each scan, first two adjacent azimuths are found, between which the GPS azimuth is located. The spline interpolation of time and the IWV_z of WVR data with the GPS elevation at these two adjacent azimuths is performed. For each scan two interpolated values are obtained (two magenta points in Fig. 4.1).

2) Based on these interpolated values of each scan from the last step, the time and the IWV_z for each scan are linear interpolated with GPS azimuth between the two adjacent azimuths. Then one interpolated value is obtained for each scan (see cyan point in Fig. 4.1).

3) For each GPS observation two adjacent scans are located. Then the two interpolated values in these two scans from the last step are extracted. When the time difference of these two interpolated values is greater than 25 min, the interpolation is stopped to take into account of approximately 23 min scanning time. Otherwise, the IWV_z is linear interpolated with the time between these two interpolated values.

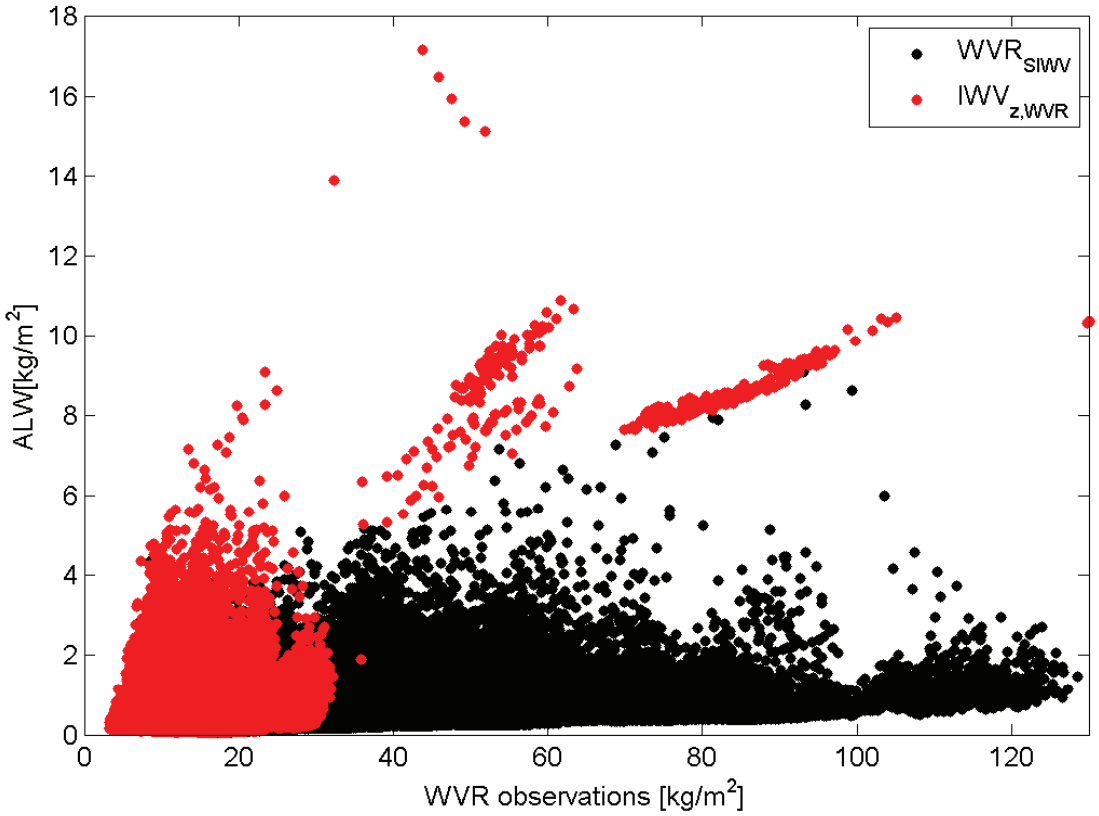

Figure 4.2: Relation between measured SIWV_{WVR}, $\mathrm{IWV}_{z,WVR}$, and Atmospheric integrated Liquid Water (ALW). Black points are measured SIWV_{WVR} data and the gray points are $\mathrm{IWV}_{z,WVR}$ (SIWV_{WVR} mapped to zenith). The extremely high values are caused by large ALW.

Finally, the interpolated IWV_z are mapped back into slant path using the GMF. In total about 59.6 % of the GPS data are validated against interpolated values from the HATPRO.

4.2 Comparison between GPS and WVR data

In total 194,489 observations are validated for a period of three months. The GPS-STDs are converted into GPS-SIWV using the methods described in section 3.3. The GMF is used. For ZHD the Saastamoinen and the Hopfield model are used for the comparison. The GPS-SIWVs (see section 3.3.3) are derived separately with two models and compared with the WVR-SIWVs. The SIWV differences, the IWV_z differences, and the SIWV relative differences are calculated:

$$\Delta_{SIWV} = SIWV_{GPS} - SIWV_{WVR} \tag{4.2}$$

$$\Delta_{IWV_z} = IWV_{z,GPS} - IWV_{z,WVR} \tag{4.3}$$

$$\Delta^r_{SIWV} = 100\frac{SIWV_{GPS} - SIWV_{WVR}}{SIWV_{WVR}}. \tag{4.4}$$

The corresponding standard deviation and Root Mean Square (RMS) are also analyzed:

$$\sigma_j = \left(\frac{1}{n-1} \sum_{i=1}^{n} (\Delta_j^i - \bar{\Delta}_j)^2 \right)^{0.5} \tag{4.5}$$

$$RMS_j = (\frac{1}{n} \sum_{i=1}^{n} |\Delta_j^i|^2)^{0.5} \tag{4.6}$$

$$\bar{\Delta}_j = \frac{1}{n} \sum_{i=1}^{n} \Delta_j^i \tag{4.7}$$

where n is the number of observations and j indicates the differences according to Eqs. 4.2, 4.3 or 4.4.

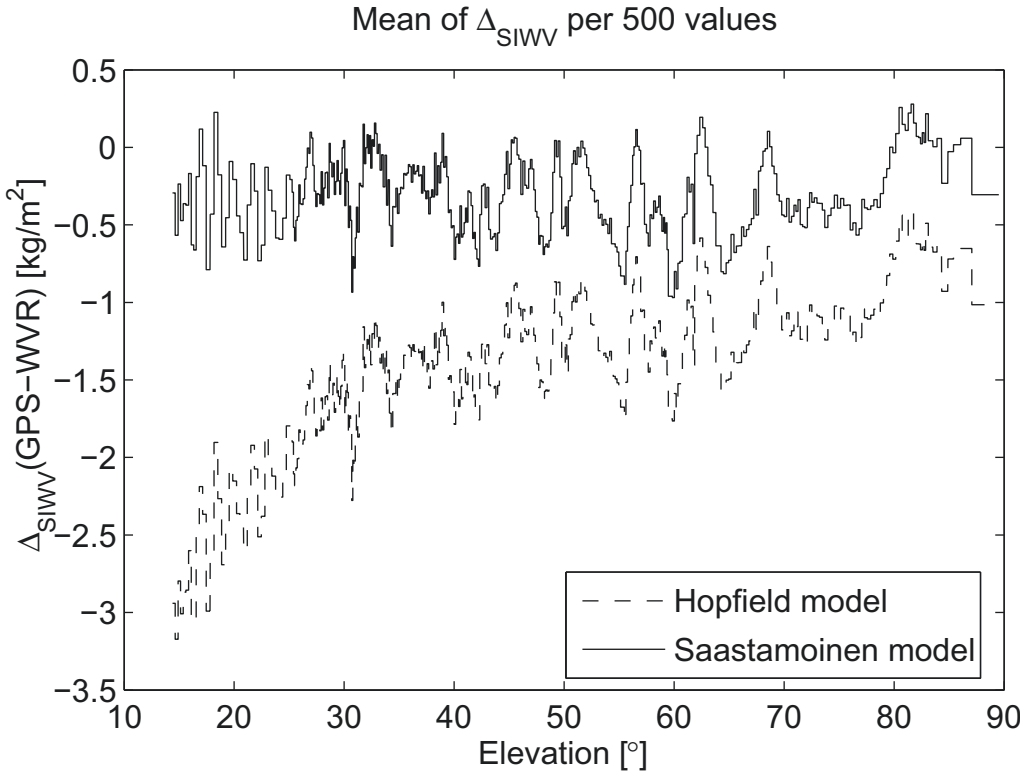

Figure 4.3: Comparison of the SIWV_{GPS} derived from Saastamoinen and Hopfield ZHD models with SIWV_{WVR} from October 5 to December 31, 2007.

Figure 4.3 shows that the bias of Δ_{SIWV} derived with Saastamoinen model are smaller than those using the Hopfield model, especially at low elevation angles. Other studies (Mendes, 1998; Schüler, 2001) have also shown that larger bias of the Hopfield model due to the assumption of a constant temperature lapse rate, unmodeled gravity variation, variation of the mean dry molar mass etc. Due to its high accuracy, the Saastamoinen model is commonly used as ZHD model. The comparison of the two ZHD models indicated better results with the Saastamoinen model and is chosen for the validation.

The statistical results for the whole period are shown in Tab. 4.1.

[kg/m^2]	Δ_{SIWV}	Δ_{IWV_z}
mean	-0.31	-0.22
σ	1.89	1.21
RMS	1.92	1.23

Table 4.1: Statistics for the comparison of SIWV and IWV$_z$ using Saastamoinen model for ZHD estimation. Number of observations: 194,489; σ: Standard deviation; RMS: Root mean square.

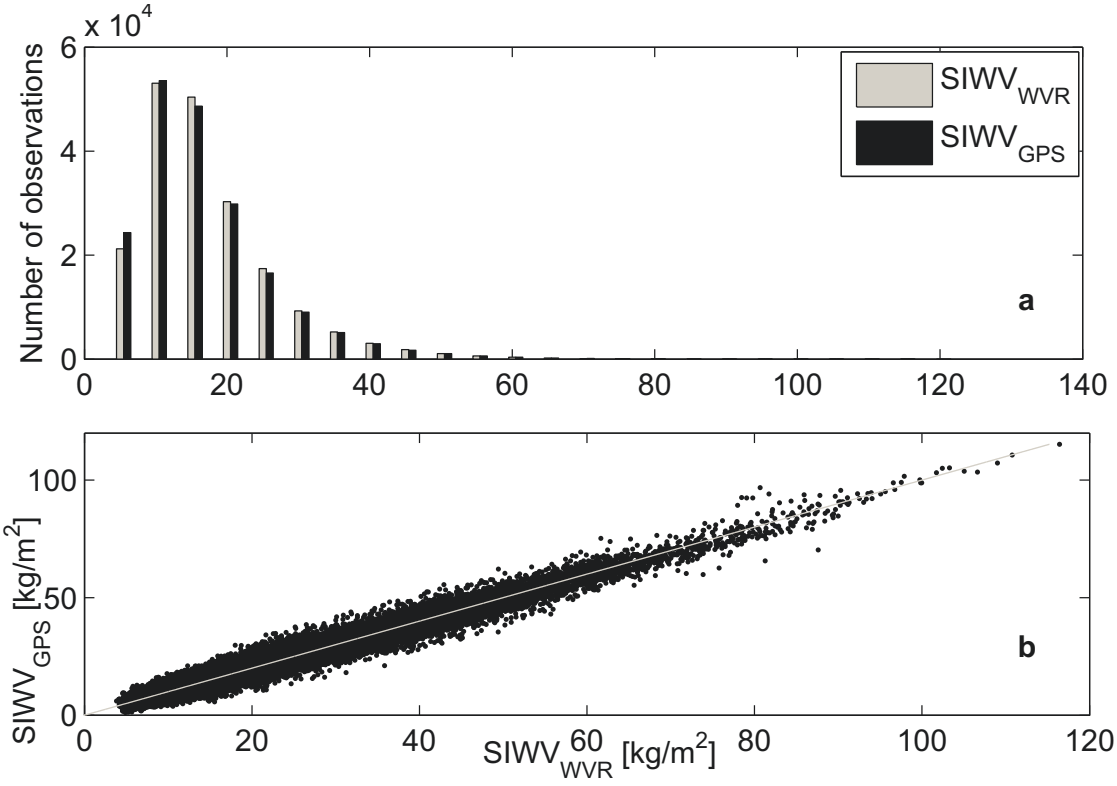

Figure 4.4: Histogram for the distribution of SIWV data every 5 kg/m^2 (a); Scatterplot of SIWVs from WVR vs. GPS for October 5 - December 31, 2007 (b).

The mean value of the SIWV$_{GPS}$ (16.47 kg/m^2) is slightly smaller than that of SIWV$_{WVR}$ (16.78 kg/m^2). Figure 4.4 (a) shows the histogram for the distribution of SIWV data for intervals of 5 kg/m^2. About 41.57 % of the Δ_{SIWV} are positive and 58.43 % negative. There are more observations with smaller SIWV$_{GPS}$, which agrees with the larger average of SIWV$_{WVR}$. About 92 % of Δ_{SIWV} fall in the range of (-3.93 kg/m^2, 2.74 kg/m^2) with a standard deviation of 1.89 kg/m^2. 49.18 % of the Δ_{SIWV} are above the mean -0.31 kg/m^2 and 50.82 % below the mean value. According to Fig. 4.4 (a), it is obvious that more SIWV$_{GPS}$ observations are in the range of 0$\sim$10 kg/m^2. One possible reason for the negative bias could be the underestimation in the SIWV$_{GPS}$. However, it shows a need to check whether the bias depends on the amount of water vapor, which will be further discussed in section 4.3.2.

Figure 4.4 (b) shows scatterplots of GPS and WVR data at station GFZ0. The best

linear fit between the two data sets is given by:

$$SIWV_{GPS} = 0.99 \cdot SIWV_{WVR} - 0.11. \tag{4.8}$$

The square of the correlation coefficient is 0.99. The IWV_z has a smaller difference and square of the correlation coefficient 0.98. In addition, the σ_{IWV_z} and RMS_{IWV_z} are smaller than σ_{SIWV} and RMS_{SIWV}, especially at low elevation. The SIWV values are more variable than IWV_z. According to different requirements, IWV_z or SIWV could be chosen for the analysis.

4.2.1 Accuracy analysis of the GPS estimates

WVR-SIWV

The accuracy of the $SIWV_{WVR}$ depends to, a large extent, on the used frequencies and the absolute accuracy of the brightness temperatures. The HATPRO is using 7 channels from 22.335 GHz to 31.4 GHz and has an accuracy about 0.7 kg/m^2. Typically the frequencies close to 22.2 GHz are more sensitive to water vapor and the frequencies around 30 GHz are more sensitive to liquid water. Invalid observations are caused by obstacles, orography, rainfall, and ALW more than 1 kg/m^2. The ALW accuracy depends on the frequency combination, brightness temperature measurement accuracy and observation angle and is between 15 g/m^2 and 25 g/m^2 (Rose et al., 2005).

GPS-SIWV

The $SIWV_{GPS}$ can be estimated from the STD using meteorological observations (see section 3.3.3):

$$SIWV_{GPS} = \Pi(STD - m_h ZHD). \tag{4.9}$$

The accuracy of the derived $SIWV_{GPS}$ is affected by the error of the mapping function, the error of the ZHD model, and the error of the observations. The uncertainty of the wet mapping function at 5° elevation angle is 0.5 % and the uncertainty of the hydrostatic mapping function at 5° elevation is approximately 1 % as determined by Niell (1996). At $\epsilon = 15°$ the mapping function error for the ZWD is negligible (Niell et al., 2001). Because the lowest elevation angle is 14.4° in the WVR measurements the mapping function error here is negligible. However, there are more factors contributing to these errors. The accuracy of the derived $SIWV_{GPS}$ depends to a large extent on the errors of the GPS-STDs:

$$\frac{\partial SIWV}{\partial STD} = \Pi. \tag{4.10}$$

The Saastamoinen model for the ZHD is generally considered almost error free (Janes et al., 1991). The main error source in the ZHD calculation is the error of pressure observations:

$$\frac{\sigma_{ZHD}}{\sigma_P} \approx 2.276\,\text{mm/hPa}. \tag{4.11}$$

The accuracy of the measured pressure with meteosensors of the type Vaisala PTU200 is 0.1 hPa. In the conversion from slant delays to SIWV, the error of the conversion

	observation errors	$\epsilon = 90°$ $m_h = 1$	$\epsilon = 14.4°$, $m_h = 3.95$	interval
$\Pi\sigma_{STD}$	$\sigma_{ZTD} = 6\,\mathrm{mm}$	1 mm	4 mm	0∼4 mm
$\frac{SIWV}{T_m}\sigma_{T_m}$	σ_{T_m} =4.7 K	<2 %	<2 %	<2.4 mm
$\Pi 2.276 m_h \sigma_P$	σ_P =0.1 hPa	0.04 mm	0.16 mm	0∼0.16 mm
σ_{SIWV}	$\sigma_{\Delta_{SIWV}}$ =1.92 kg/m^2	-	-	∼1.79 kg/m^2

Table 4.2: Effects of important error sources in the determination of water vapor from GPS observations.

factor Π is also important. The relative error of the Π approximates the relative error of the mean temperature of the atmosphere T_m:

$$T_m = \frac{\int (e/T)\, dh}{\int (e/T^2)\, dh} \tag{4.12}$$

where e is the partial pressure of water vapor in hPa, T is the absolute temperature in K and h is the height ASL in meter. Another possibility is the calculation of T_m using the surface temperature T_0 with an empirically determined function instead of the temperature profile (see Eqs. 3.25). An accuracy of 4.7 K, corresponding to a relative error less than 2 % was determined for this method by Bevis et al. (1992, 1994).

$$\frac{\sigma_\Pi}{\sigma_{T_m}} \approx \frac{\Pi}{T_m}. \tag{4.13}$$

Using the Eq. 4.13 the results from the error propagation of Eq. 4.9 are given by:

$$\sigma^2_{SIWV} = \Pi^2(\sigma^2_{STD} + \sigma^2_{ZHD}) + \frac{SIWV^2}{\Pi^2}\sigma^2_\Pi = \Pi^2(\sigma^2_{STD} + m_h^2 2.276^2 \sigma^2_P) + \frac{SIWV^2}{T_m^2}\sigma^2_{T_m} \tag{4.14}$$

where the maximum conversion factor $\Pi = 0.17$ is used for the error estimation and the σ_{SIWV} is in mm. The comparison between GPS and WVR data indicates a small bias in these three months. The important error sources for the determination of water vapor from GPS observations are described in Tab. 4.2. The ZTDs have an accuracy of 6-13 mm (Gendt et al., 2004). The surface temperatures were used to calculate T_m. The STD error increases with decreasing elevation. In Tab. 4.2 the estimated errors in SIWV at lowest elevation angle 14.4° and highest elevation angle 90° are shown. The σ_{T_m} is estimated roughly according to Bevis et al. (1992, 1994).

In accordance to Eq. 4.2 and the validation results in Tab. 4.1, the accuracy of SIWV can be estimated by

$$\sigma_{\Delta_{SIWV}} = \sqrt{\sigma^2_{SIWV_{GPS}} + \sigma^2_{SIWV_{WVR}}} \tag{4.15}$$

where $\sigma_{\Delta_{SIWV}} = 1.92\,\mathrm{kg/m^2}$ and $\sigma_{SIWV_{WVR}} = 0.7\,\mathrm{kg/m^2}$, which can be a little worse with interpolation. The obtained $\sigma_{SIWV_{GPS}}$ is ∼1.79 kg/m^2.

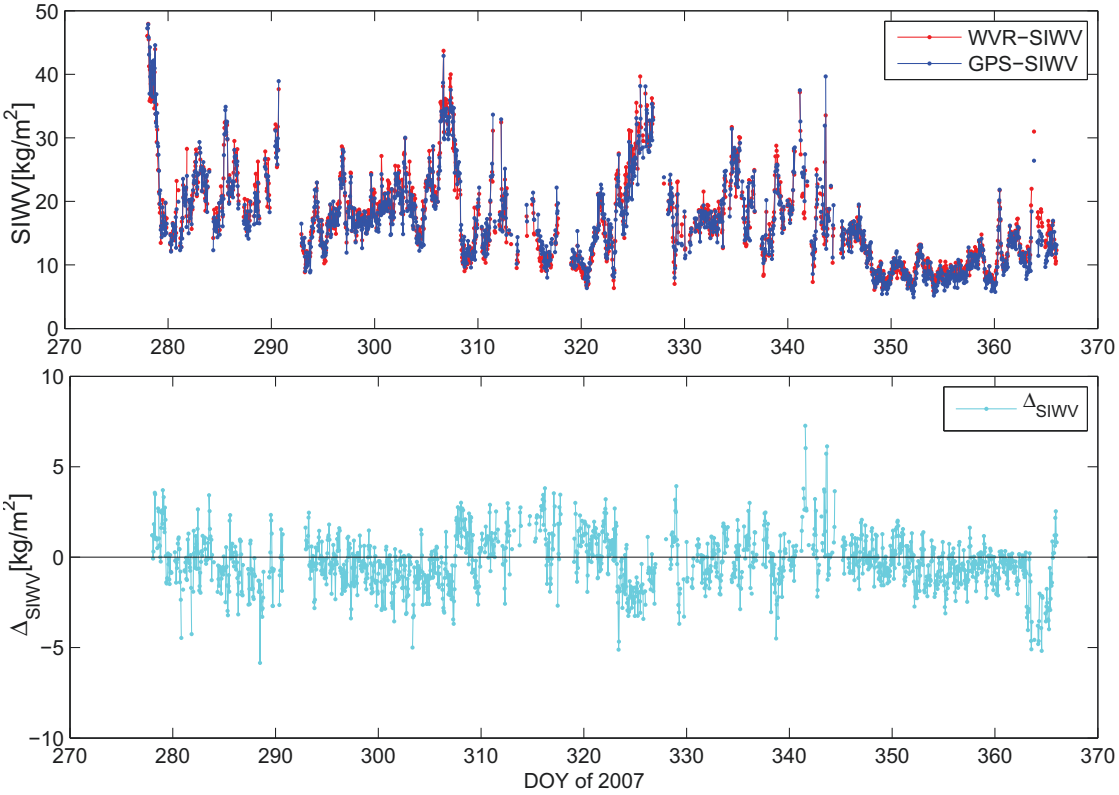

Figure 4.5: Hourly mean SIWV derived from GPS (blue), WVR (red), and their differences Δ_{SIWV} (cyan) from October 5 to December 31, 2007.

4.2.2 Results

The overall impression of the validation is that the GPS-SIWV are consistent with WVR observations on average, but when all observations are shown, it is difficult to see the change of Δ_{SIWV} because there are too many observations at the same time. Taking hourly means, the small differences between GPS and WVR can be identified. An overview of the hourly mean data is shown in Fig. 4.5.

The time gap on day 318 (November 14) is due to a calibration of WVR. The WVR data on this day were very divergent and could not be used. Other gaps were due to rejected data with an ALW more than $1\,\mathrm{kg/m^2}$ and rainfall. In general, the observations of GPS and WVR match well. However, the Δ_{SIWV} shows irregular temporal variations over several weeks with long periods of rather small variations and fast transitions. For example, from day 320 to 322 the hourly mean differences have large positive values. In contrast, the hourly mean differences on day 323 to 325 change from large positive values to negative values. Changes between negative and positive values recur with time. Regarding the GPS processing strategy, i.e. PPP processing of single stations in near real-time, it is difficult to understand the rather long period of these variations.

Therefore, attempts are made to correlate the SIWV differences with atmospheric parameters which usually vary with periods of days and weeks. This is presented in the next section.

Statistic data according to elevation angles

elevation	n	$\bar{\Delta}_{SIWV}$[kg/m^2]	$\bar{\Delta}^r_{SIWV}$[%]	$\sigma_{\Delta_{SIWV}}$[kg/m^2]	$\sigma^r_{\Delta_{SIWV}}$[%]
14.4°-20°	9683	-0.31	-0.96	3.32	11.51
20°-30°	27606	-0.28	-1.11	2.35	12.05
30°-40°	38756	-0.24	-1.06	1.99	12.85
40°-50°	33645	-0.37	-2.33	1.72	13.35
50°-60°	31239	-0.4	-3.16	1.57	13.88
60°-70°	23064	-0.39	-3.35	1.48	14.39
70°-80°	19751	-0.38	-3.53	1.38	14.37
80°-90°	10745	0.06	1.24	1.27	13.58

Table 4.3: Elevation dependency of Δ_{SIWV} comparison: Most of observations were obtained at elevation angles between 20° and 80°. The σ_{SIWV} increase in this range and the σ^r_{SIWV} are almost equivalent, which shows the similar quality at different elevation angles.

4.3 Discussion

As mentioned above, the validation results show discrepancies within the data of several days. To analyze these discrepancies, the relation between the Δ_{SIWV}, IWV$_z$, and the meteorological data are studied in this section. In addition, the elevation angle, which is an important parameter in the data processing, is also considered.

4.3.1 Dependency of bias on the elevation

The elevation angle plays an important role in the data processing. In GPS data processing, low elevation observations are typically more corrupted by multi-path effects and antenna phase center calibration errors (Braun et al., 2001). In addition, the error of the mapping function is also elevation-dependent (Davis et al., 1985). Therefore, the relation between the Δ_{SIWV} and the elevation angle is studied here.

Figure 4.6 shows the dependency of Δ_{SIWV} on the elevation angle. The standard deviation of Δ_{SIWV} decreases with the increasing elevation angles. In Tab. 4.3 the statistic data for Δ_{SIWV} and Δ_{IWV_z} as well as the relative deviation Δ^r_{SIWV} are shown. The $\bar{\Delta}_{SIWV}$ and $\bar{\Delta}^r_{SIWV}$ are similar at different elevation ranges except for the elevation range of (80°, 90°). However, the number of observations above 80° is less than in other 10° intervals. In addition, the SIWV values at high elevation are typically smaller than at low elevations. Therefore, the bias with fewer observations at high elevation is more sensitive to the very large or small values. The $\sigma_{\Delta_{SIWV}}$ decreases slightly with the increasing elevation up to 80°, which is also shown in Fig. 4.7 (a). In contrast, $\sigma_{\Delta_{IWV_z}}$ has opposite tendency. In Fig. 4.7 (a) the $\sigma_{\Delta_{SIWV}}$ decreases indisputably from 3 kg/m^2 to 1.3 kg/m^2 with increasing elevation angle, but a small increase in the $\sigma_{\Delta_{IWV_z}}$ is shown with increasing elevation angle. Simultaneously, the $\sigma_{\Delta^r_{SIWV}}$ is almost equally good at different elevation angles (Fig. 4.7 (b)). Therefore, the σ_{SIWV} is only relative dependent on the elevation angles, because the variations $\sigma^r_{\Delta_{SIWV}}$ are moderately equivalent at different elevation angles.

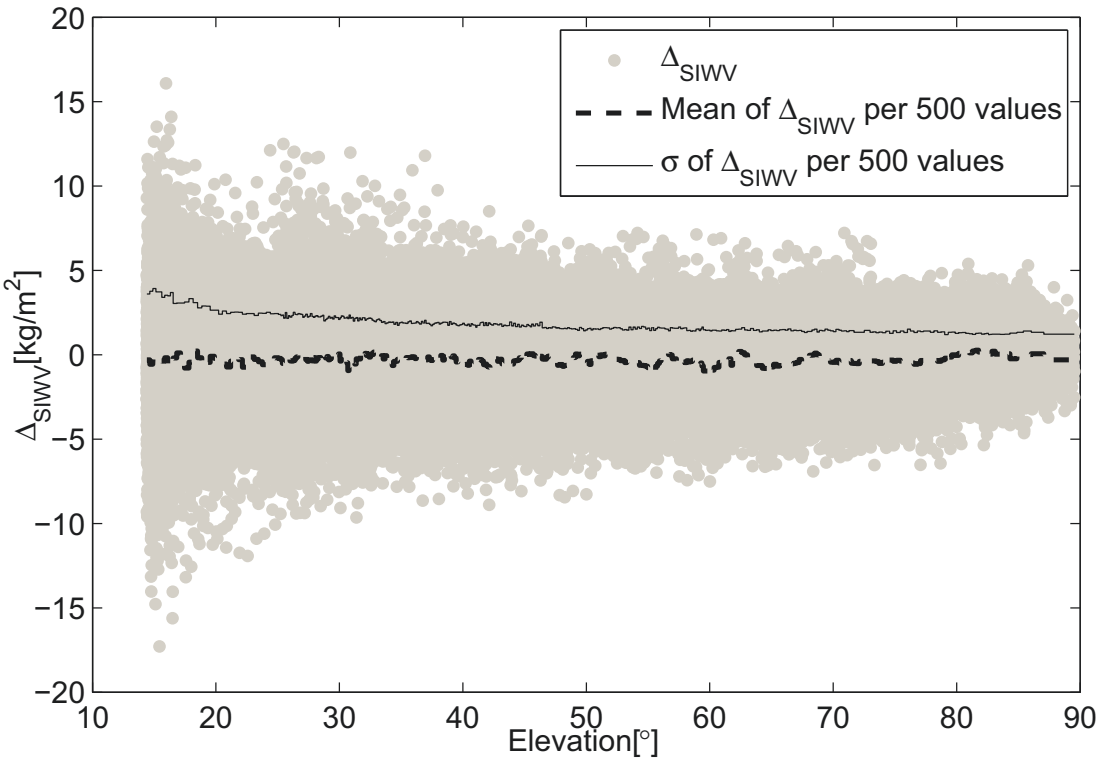

Figure 4.6: Relation between elevation and Δ_{SIWV} (gray points). The dashed line is the mean value of every 500 values and the full line is its standard deviation.

4.3.2 Dependency of bias on the amount of water vapor

As discussed in section 4.2, there is a need for the investigation of the SIWV differences between GPS and WVR at times with different amount of water vapor, especially at very dry or wet conditions. To represent the amount of water vapor, the IWV_z derived from WVR data with Eq. 4.1 is used. A check of the relation between IWV_z and the bias of Δ_{SIWV} is established. Normally the IWV_z are below 60 kg/m^2 in Germany. As shown in Fig. 4.8 (a), the bias of Δ_{SIWV} varies slightly with the IWV_z. The majority of positions observed in the last three months of 2007, the IWV_z varied between 5 kg/m^2 and 25 kg/m^2 (Fig. 4.8 (b)), which is smaller than the half of the IWV_z range in Germany. In this range the Δ_{SIWV} decrease slightly accompanied with a slightly increase of $\sigma_{\Delta_{SIWV}}$.

For more humid conditions the WVR observes somewhat smaller SIWV than GPS leading to a bias 1.5 kg/m^2 at IWV_z = 25 kg/m^2. The $\sigma_{\Delta_{SIWV}}$ is approximately 1.5 kg/m^2. However, there are few large IWV_z values in autumn and winter and large IWV_z values show up mostly in October 5 (Fig. 4.9). The IWV_z on October 5 varied in the range [14.41 kg/m^2, 30.79 kg/m^2]. Particularly between 22 kg/m^2 and 28 kg/m^2 the increase of the bias is very strong.

It should be kept in mind that the measurements are made during the autumn and winter and that the number of large IWV_z values are not sufficient here. To identify

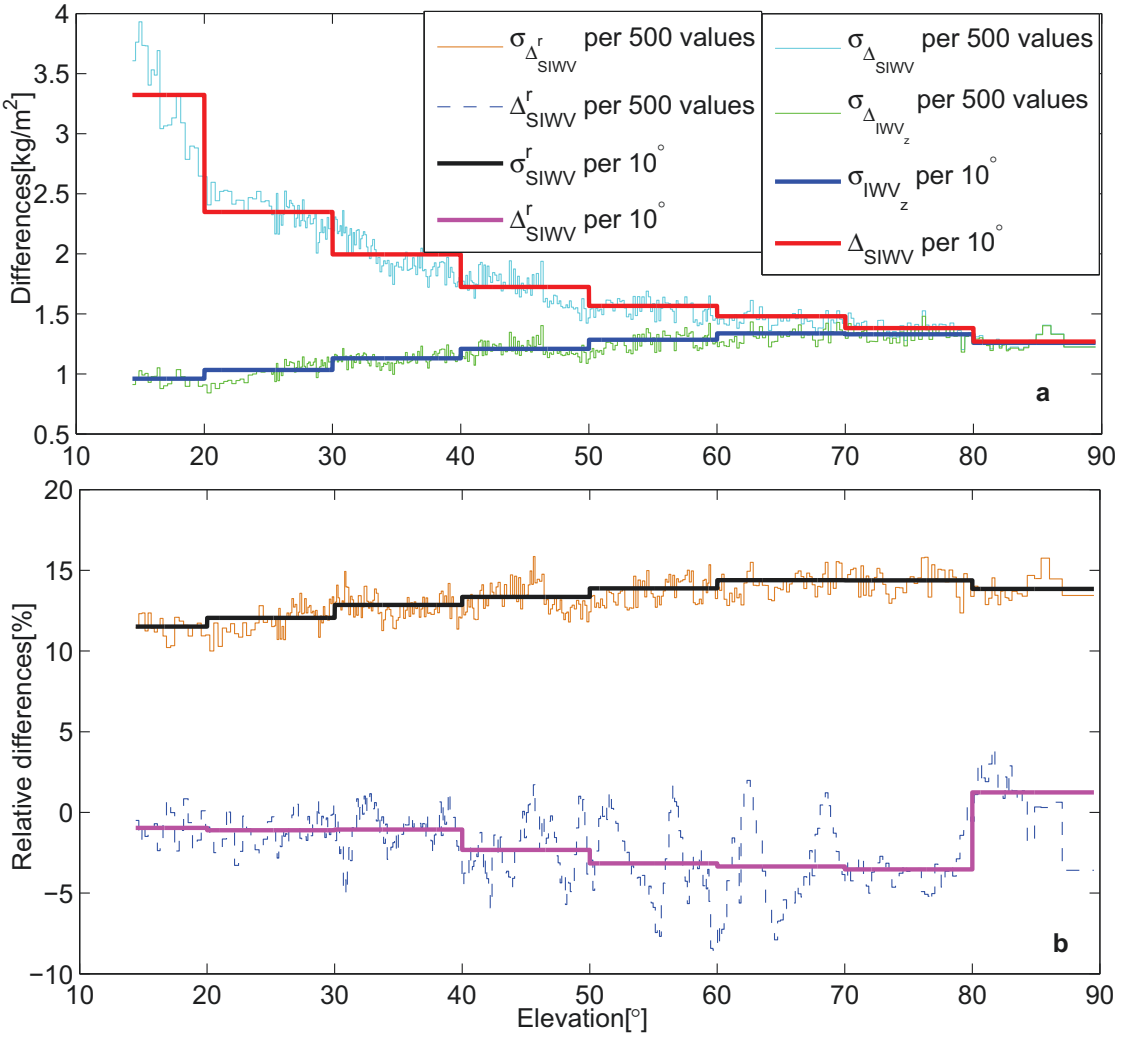

Figure 4.7: Standard deviation of SIWV differences ($\sigma_{\Delta_{SIWV}}$) and IWV$_z$ differences ($\sigma_{\Delta_{IWV_z}}$) (a); Relative SIWV differences (Δ^r_{SIWV}) and their standard deviation ($\sigma_{\Delta^r_{SIWV}}$) (b).

the dependency on the very wet conditions more data with large IWV$_z$ values are required.

For very dry conditions, the days December 17 to December 19 were chosen (Fig. 4.10). The IWV$_z$ in these three days are all below 8.5 kg/m^2. The bias and standard deviation of the Δ_{SIWV} change only slightly. The mean of Δ_{SIWV} is only a small negative value near 0. In contrast to Fig. 4.9 many more observations with small IWV$_z$ are shown in the histogram. No clear dependency between the bias and IWV$_z$ is found.

Therefore, it could be concluded that the total amount of water vapor in the atmosphere has no significant influence on the bias of Δ_{SIWV} for IWV$_z$ below 15 kg/m^2. Since the number of observations above IWV$_z$ = 15 kg/m^2 is rather small (15.18 %) here, more observations in summer are required to make statistically analyses of these soundings.

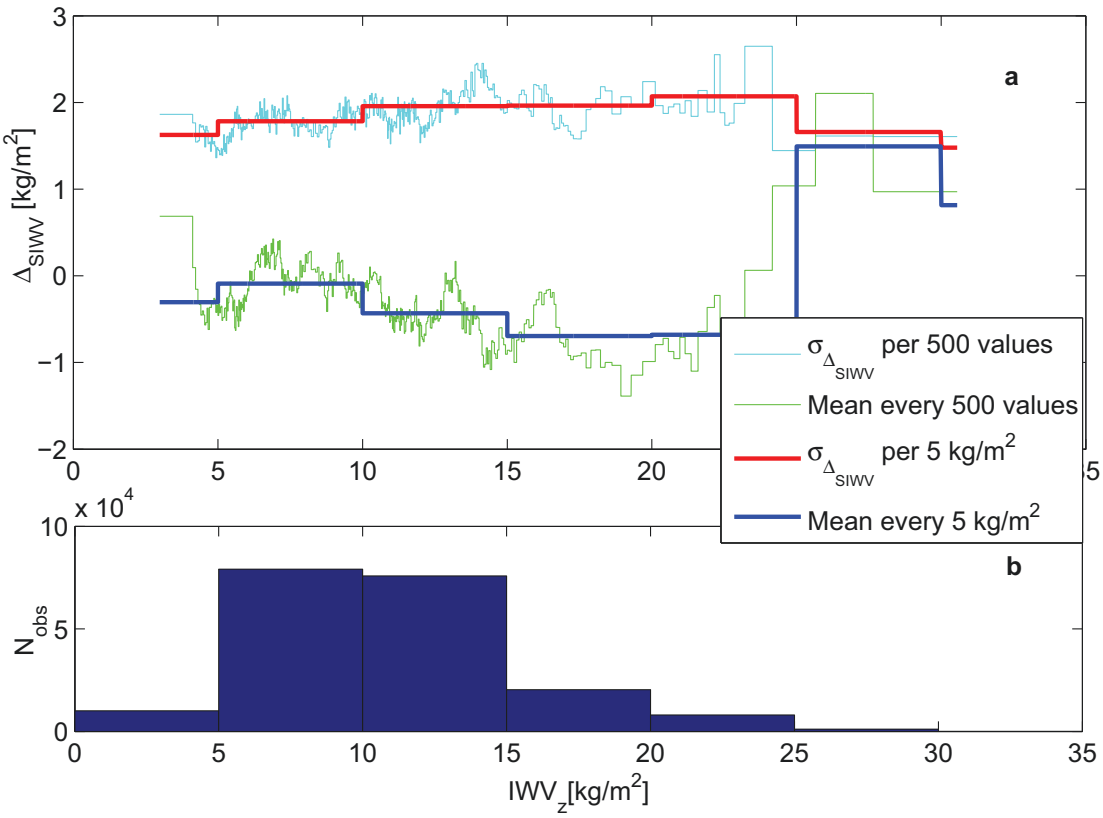

Figure 4.8: Mean of SIWV differences (Δ_{SIWV}) every 500 values and every 5 kg/m^2 IWV$_z$ and their corresponding standard deviation $\sigma_{\Delta_{SIWV}}$ as a function of IWV$_z$ (a); Histogram of the corresponding data distribution (b).

4.3.3 Dependency of bias on the weather situation

From the meteosensor located near the GPS antenna GFZ0, Pressure (P), temperature (T) and relative humidity (rh) were collected. The pressure and temperature used to calculate the SHD for estimating the SIWV$_{GPS}$ could have an effect on the estimated SIWV (Tab. 4.2). The scatterplots between rh, T, P and Δ_{SIWV}, Δ^r_{SIWV}, SIWV$_{GPS}$ are shown in Fig. 4.11.

In Fig. 4.11, middle, the SIWV$_{GPS}$, Δ^r_{SIWV}, and Δ_{SIWV} change stronger with the variation of pressure than those of temperature and relative humidity. It is difficult to find the dependency between pressure and Δ_{SIWV} with the strong variability. In contrast, Δ^r_{SIWV} and Δ_{SIWV} have a negative bias at low temperatures and smaller fluctuation at high temperatures (Fig. 4.11, bottom).

In Fig. 4.11, top, the relation between Δ_{SIWV}, Δ^r_{SIWV} as well as the GPS-SIWV and rh is shown. Most of the observations are with a rh of more than 38 %. There is a negative bias with rh smaller than 38 %. The GPS-SIWVs are also very small in this range. However, nearly all of the observations with rh smaller than 38 % are located on December 29. Further studies are essential to verify the relation between the large negative bias and weather situation at low humidity. The time series are shown in Fig. 4.12.

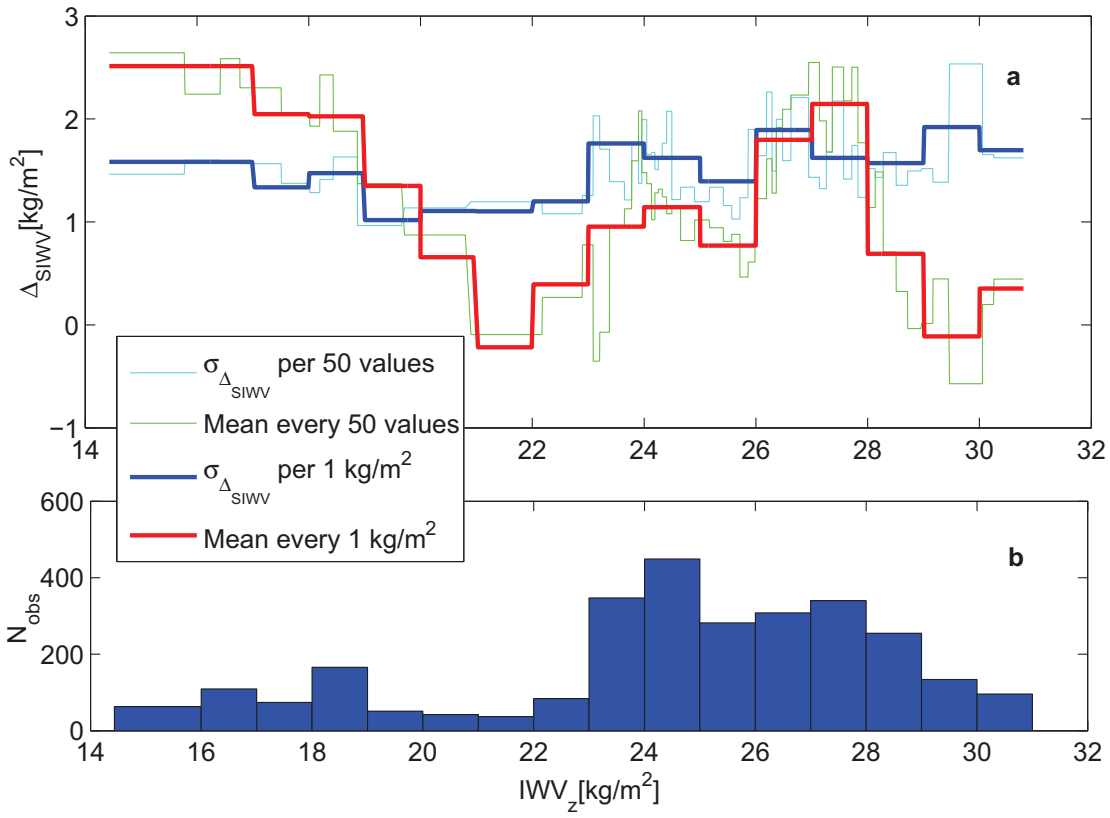

Figure 4.9: SIWV differences (Δ_{SIWV}) as a function of the IWV$_z$ and their standard deviation (a); Histogram of the corresponding data distribution on October 5, 2007 (b).

As can be seen in Fig. 4.12, at noon the temperature is at highest and the rh is at lowest. The Δ_{SIWV} and Δ^r_{SIWV} do not change much. On December 29 the rh minimum appears and the hourly mean of differences around this time are smallest. The temperature and ALW also have a local maximum (vertical line in Fig. 4.12). It could be assumed that the strong change of weather situation has an effect on the result. However, this sudden change happens only on one day. More data with low rh are necessary for the research. The correlation between the Δ_{SIWV} and the weather situation is low. No clear relation between the weather situation and the differences is found. More data in summer are required for further studies.

GFZ continually operates a WVR (HATPRO) since October 2012 in Potsdam. With the new WVR at GFZ, the SIWV can be directly compared to GPS. By selecting the satellite tracking mode, the WVR measures the SIWV directly in satellite direction. For the tracking, the RINEX navigation files are essential to determine the satellite positions. Then the radiometer can periodically scan a number of visible GPS satellites. This allows validations of the measured SIWV values against the GPS values without interpolation. The first result made by Heise et al. (2013) is shown in Fig. 4.13 with the mean -0.39 kg/m^2 and σ = 3.05 kg/m^2 of Δ_{SIWV}. However, the location of WVR HATPRO at GFZ is on the roof of the building. No obstacle is around the instrument and the cut-off elevation is 7°, which is much smaller than 14.4° at GFZ0. The standard deviation and the bias are larger with the lower cut-

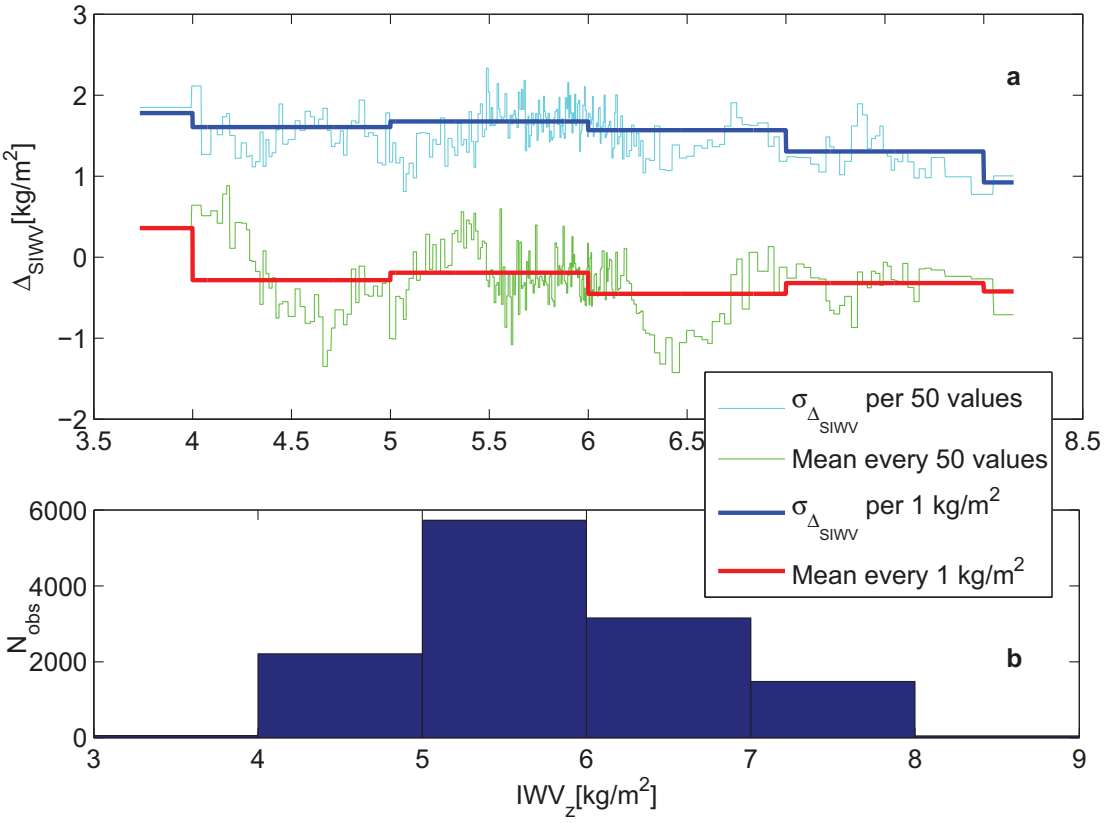

Figure 4.10: SIWV differences (Δ_{SIWV}) (from left to right) as a function of the IWV$_z$ and their standard deviation (a); Histogram of the corresponding data distribution from December 17 to 19 (b).

off elevations. In addition, the ALW limit of 2 kg/m^2 is used compared to 1 kg/m^2 for GFZ0 comparison. Considering the above reasons, the result obtained with interpolation in this thesis is comparable with the result from the satellite tracking mode. In the near future long time series including data from summer and winter periods will be collected by the new WVR HATPRO at GFZ. Then the data would be used for the further studies, to investigate the temporal variations in Δ_{SIWV} with periods of several days.

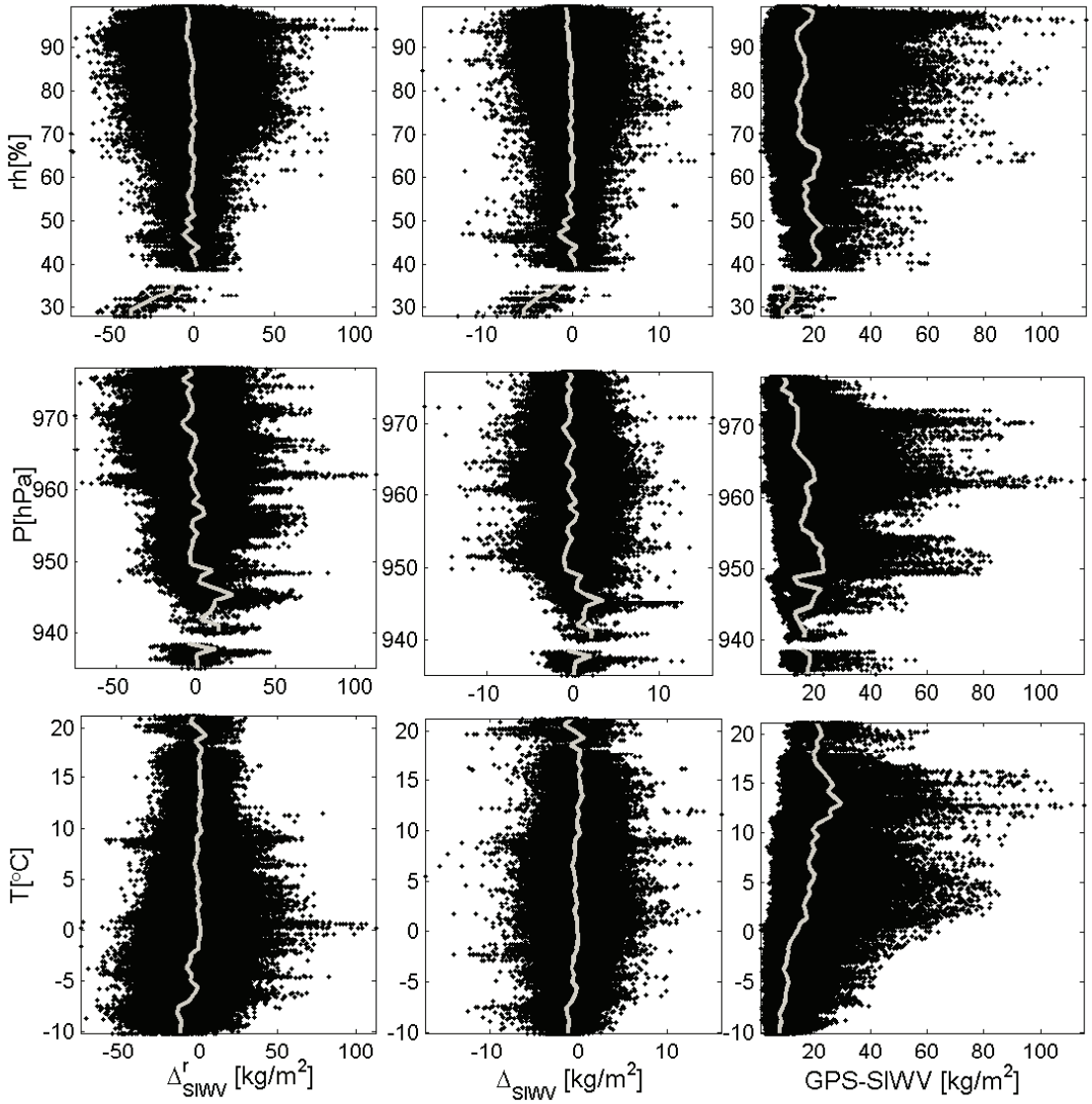

Figure 4.11: Relative differences of SIWV (Δ^r_{SIWV}) (left column), differences of SIWV (Δ_{SIWV}) (middle column), SIWV$_{GPS}$ (right column) as a function of relative humidity (rh) (top row), pressure P (middle row), temperature T (bottom row). The mean values of observations are indicated by the gray lines.

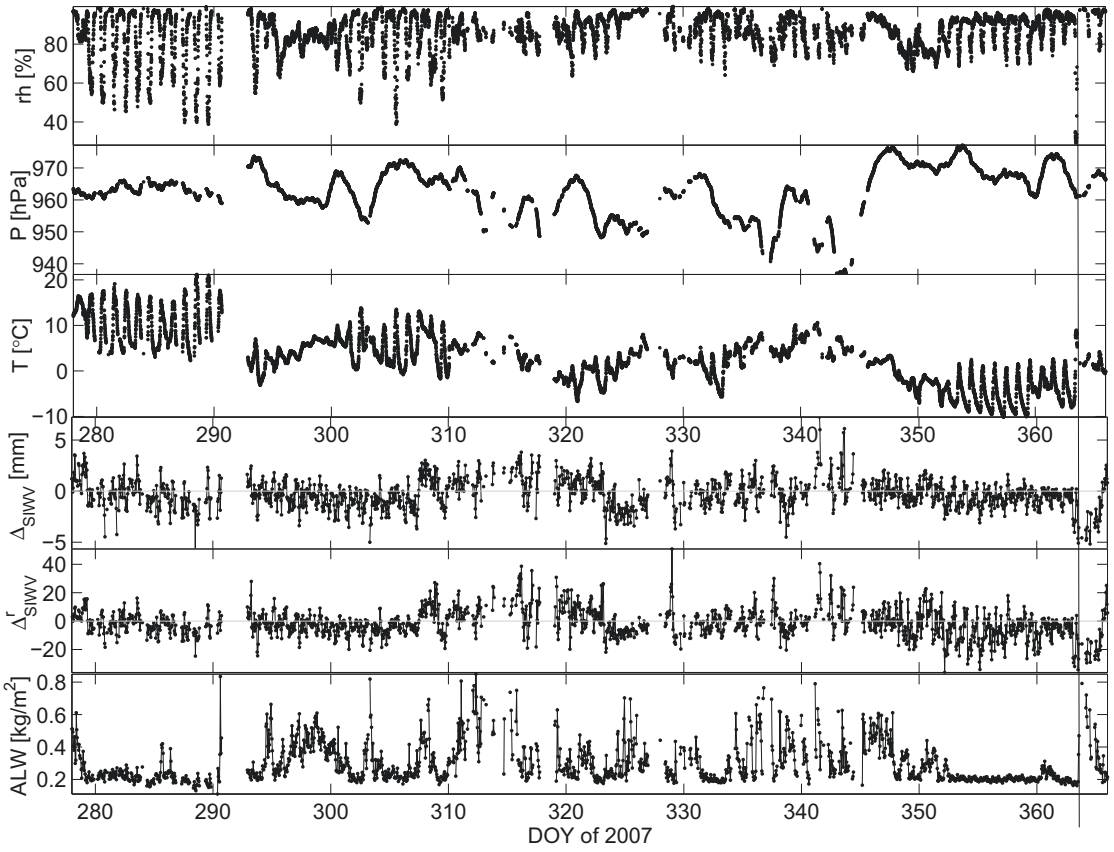

Figure 4.12: Relative humidity (rh), Pressure (P), Temperature (T), hourly mean of differences SIWV (Δ_{SIWV}) and relative differences SIWV (Δ^r_{SIWV}), ALW as a function of time. The vertical line marks data on December 29 with rh minimum.

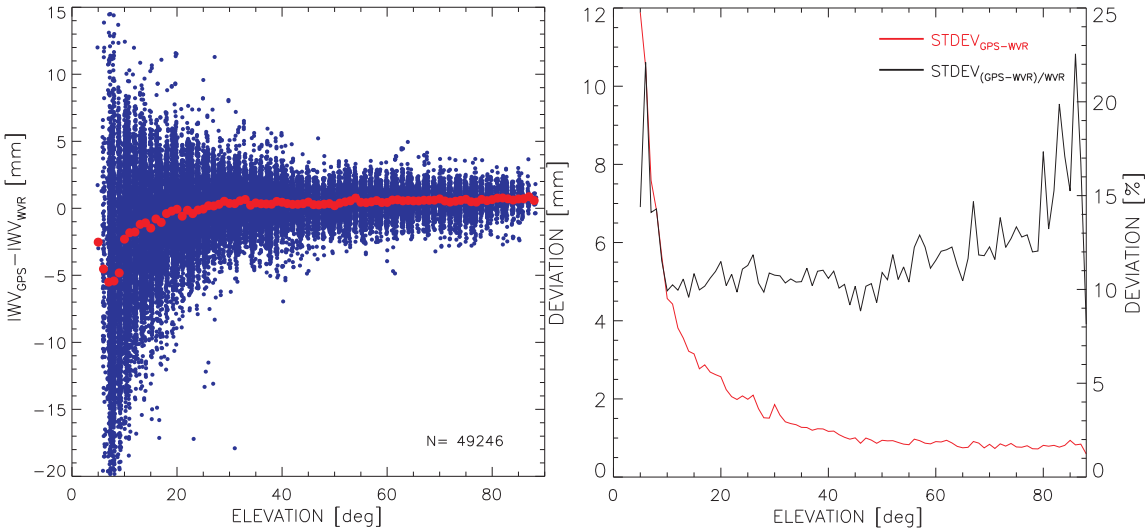

Figure 4.13: SIWV comparison between GPS and WVR located at the roof of GFZ building A17 obtained with a new WVR running in satellite tracking mode for DOY 001-090, 2013. All data with rainflag or liquid water content above $2\,\mathrm{kg/m^2}$ are excluded and the cut-off elevation is 7°. Left: Elevation dependency of GPS-WVR deviation, red dots show the mean deviation and IWV in the figure is equivalent to SIWV in this figure. Right: Elevation dependency of the mean absolute (red line) and relative (black) standard deviation (Heise et al., 2013).

5 Analysis of water vapor time series for Germany

At present, several operational GPS networks are available worldwide for providing information of water vapor in the atmosphere which makes the trend analysis possible. The running of GRUAN and GNSS4SWEC projects are aimed to provide advanced tropospheric products with consistent quality for the climate research. The analysis of water vapor time series of German stations is described in this chapter. The analysis strategy developed here can be applied to each reprocessed IWV data set in order to obtain the latest trend estimates. The data used in this chapter will be contribute to the above mentioned projects.

5.1 Available GPS data for water vapor in Germany

The tropospheric GPS delays have been measured since the end of 1998 for a subset of about 11 stations at GFZ. At the beginning of the GPS processing only a few stations were available. More and more GPS stations supplied data in the following years. The increasing number of stations, providing IWV, is shown in Fig. 5.1. All the data are processed using EPOS and are available as part of the operational GFZ near real-time atmosphere processing. For the trend analysis, the time period from

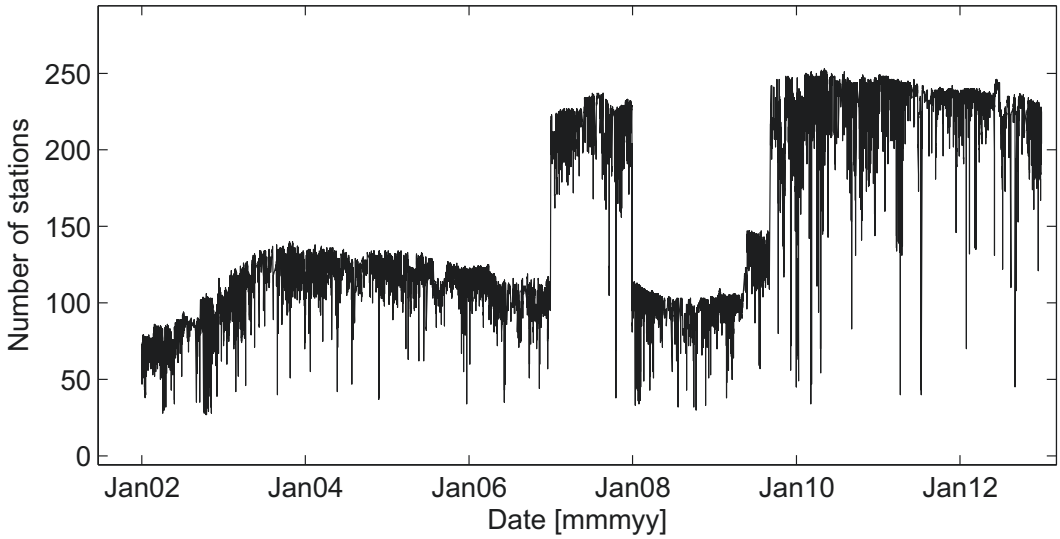

Figure 5.1: Number of GPS stations, which provide IWV data in and near Germany from 2002 to 2012: The number of stations increased temporary because of the COPS project in 2007; From the end of 2009 the stations used in the COPS project are available again and more new stations are added in the network.

2002 to 2012 is selected. Since 2000, tropospheric products containing the ZTD and IWV with a sampling rate of 30 min are generated operationally. However, the data acquired in the first two years (1998-1999) are not used due to long data gaps. During the years 2000 and 2001 there were still only few stations available. Since 2002, there are more GPS sites (about 90 stations) with continuous observations.

IWV time series of many stations do not cover the full period of 2002-2012. Temporarily, there were more GPS stations available in the year 2007 because of the COPS campaign (see section 4.1). Reanalysis of this time period filled the data gaps. Therefore, more accurate data of stations are available for 2007. When a new version of the EPOS became operational in 2007, the sampling rate was increased to 15 min. For this reason, a second period from 2007 to 2012 is chosen for the analysis.

For the long-term trend analysis in climate changes, a continuous record for at least 30 years is usually necessary (Intergovernmental Panel on Climate Change (IPPC) 2007). Nevertheless, the trend analyses of the IWV time series in the last 11 years provide valuable insights for the short-term temporal variations of the water vapor distribution above Germany. In this chapter, the IWV trends using GPS data from the German network from 2002 to 2012 period are studied and compared with numerical weather model's reanalysis products. The trends for different stations and regions are calculated separately.

5.2 Statistical methods

Climate research requires long time series of observations. GPS cannot yet provide such long time series but different analysis strategies can already be investigated using the currently available observations. The station Aschau (0264) in southern Bavaria is chosen as an example because of its comprehensive continuous data set since 2002. Figure 5.2 shows the time series of station Aschau. The data contains a strong seasonal cycle of water vapor. In winter the water vapor concentration (up to $15\,\mathrm{kg/m^2}$) is considerably below the summer level (up to $44.3\,\mathrm{kg/m^2}$). The regular annual cycle is overlayed with diurnal variations, which makes it reasonable to apply statistical averages before performing the analysis. Based on these data sets, statistical means are calculated. Three different estimation methods and their resistance against outliers are discussed. For the IWV time series outliers can be caused by measurement errors or unusual weather events and could have a large influence on the calculated mean values. The estimates can be strongly influenced by even very few outliers (Lanzante, 1996). For data analysis, the results from three methods are compared in order to obtain the most accurate results: the arithmetic mean, the median, and the biweight mean. The arithmetic mean is a classical method:

$$\bar{x} = \frac{1}{a}\sum_{i=1}^{a} x_i. \tag{5.1}$$

This method is not robust, because the arithmetic mean can be shifted with relatively few very large or small values (outliers). An alternative is the median, which is much more resistant against outliers than the arithmetic mean. The median is based on a list of observations sorted by the value of the observed variable (IWV), and it is given by the element in the middle of the listed observations:

$$x_m = \begin{cases} x_{\frac{a+1}{2}} & \text{a odd} \\ \frac{1}{2}\left(x_{\frac{a}{2}} + x_{\frac{a+1}{2}}\right) & \text{a even} \end{cases}. \tag{5.2}$$

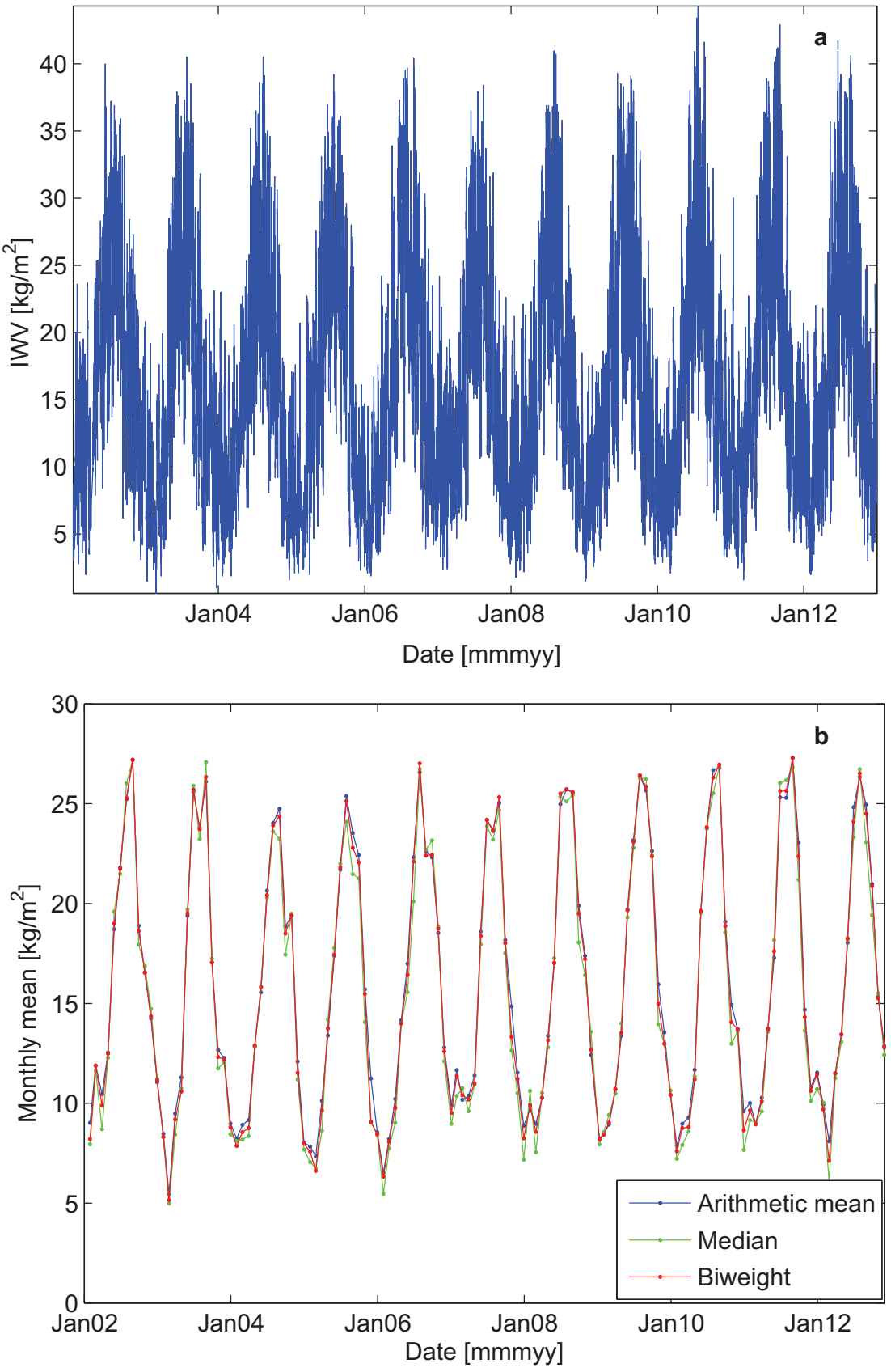

Figure 5.2: IWV time series at station 0264 in Aschau for the last 11 years (a), which are available at GFZ; Comparison of monthly averages: Arithmetic mean (blue), Median (green), Biweight mean (red) (b).

Specifically, in cases of the non-Gaussian distributions, the median is preferred to the arithmetic mean. A third method is the biweight mean, in which the average is calculated with weights for data points. With the help of median and the Mean Absolute Deviation (MAD) the biweight mean x_b can be computed with the following equations (Lanzante, 1996):

$$x_b = x_m - \frac{\sum_{i=1}^{N}(x_i - x_m) \cdot (1 - u_i^2)^2}{\sum_{i=1}^{N}(1 - u_i^2)^2} \tag{5.3}$$

$$u_i = \frac{x_i - x_m}{d \cdot MAD} \tag{5.4}$$

$$MAD = \text{median}|x_i - x_m| \tag{5.5}$$

where the constant d is a critical distance from the mean and needs to be defined according to the application. For the IWV analysis, the constant d is set to 7.5 and for any $|u_i| > 1.0$ set $u_i = 1.0$. The calculated x_b considers all available elements (Eq. 5.4), but the method is also robust against outliers. For those reasons, this method is widely used in the climatology and trend analysis (Gaffen and Ross, 1999; Ferro et al., 2005; Schmidt et al., 2010). In Fig. 5.2, the three methods are used to compute monthly means of the station 0264 in Aschau. The values of the biweight mean are as a rule between the values of the other two methods. The arithmetic mean equals simply the center of distribution and the median is a resistant statistic, having the middle value of the data. If the difference between arithmetic mean and median is large, the distribution is usually non-Gaussian. However, the median can be very inaccurate when there are large data gaps. In contrast the biweight mean is insensitive to larger sampling variability and more resilient in the presence of outliers and the only assumption is that the observations are distributed homogeneously (homogeneity) (Lanzante, 1996).

Based on the results of the comparison of the three averaging methods, the biweight mean is considered as the best method for the analysis of the selected water vapor data, due to its robustness. All mean values of GPS data used in this chapter are subsequently computed with this method.

5.3 Results for selected stations

About 300 stations are currently available, which provide ZTD and IWV data for Germany and the number grows each year. However, only few of them provide data for the whole period from 2002 to 2012.

Monthly mean anomalies derived from the mean value of each month are calculated. The monthly mean anomalies A_i are determined using the monthly mean M_i and the mean value M_a of individual months (January, February,...,December) in the whole period:

$$A_i = M_i - M_a \tag{5.6}$$

$$M_a = \frac{\sum_{m=1}^{m=n} M_a^m}{n} \tag{5.7}$$

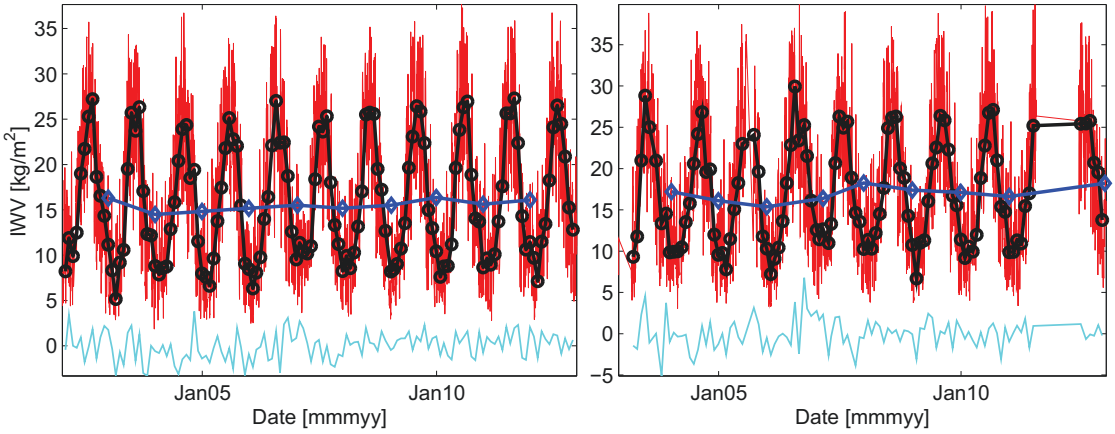

Figure 5.3: Daily (red), monthly (black), annual means (blue) and the monthly mean anomalies (cyan) of the 11 years IWV time series at station 0264 in Aschau (left) and station 0521 in Landau in der Pfalz (right).

where the index a refers to the month (a = January, February ... December), n is the number of years in the period and M_a^m is the mean value of the month a at the nth year. The summer anomalies cover the months June, July, and August and the winter anomalies the months December, January, and February.

Figure 5.3 shows the daily, monthly and annual means of the IWV and the derived monthly anomalies of the last 11 years. The seasonal variations of the water vapor are presented in Fig. 5.3. For the water vapor analysis, monthly mean anomalies are computed for the trend calculation for 11 years. No daily mean values are considered due to their dependence on the current weather conditions. Also annual mean values could be used to calculate anomalies for long-term trends. However, only 11 years of data are not long enough to obtain reliable annual anomalies. For the time period 2002-2012, the IWV monthly anomalies show a range of (-3.31 kg/m^2, 3.81 kg/m^2) for station 0264 and (-5.11 kg/m^2, 6.78 kg/m^2) for station 0273. In contrast, for the second time period 2007-2012, IWV anomalies show a range of (-7.4 kg/m^2, 7.37 kg/m^2) for station 0264 and (-10.06 kg/m^2, 6.87 kg/m^2) for station 0521. The anomalies based on the six years time series clearly show stronger variation.

To get an overview of the variation of the water vapor distribution above Germany, the annual means of all GPS stations are calculated. As an example, the IWV annual means for 2002 and 2010 are shown in Fig. 5.4. Only the annual means of stations with data gaps smaller than three months are calculated here. The number of stations increases from 62 in 2003 to 251 in 2010. The station number and density have a large influence on the results of the horizontal interpolation of regions. The annual mean IWV values of GPS stations are between 12.55 kg/m^2 and 18.52 kg/m^2 in 2002 and between 6.73 kg/m^2 and 20.29 kg/m^2 in 2010. More details within the water vapor distribution can be seen in 2010 rather than in 2002 due to more stations.

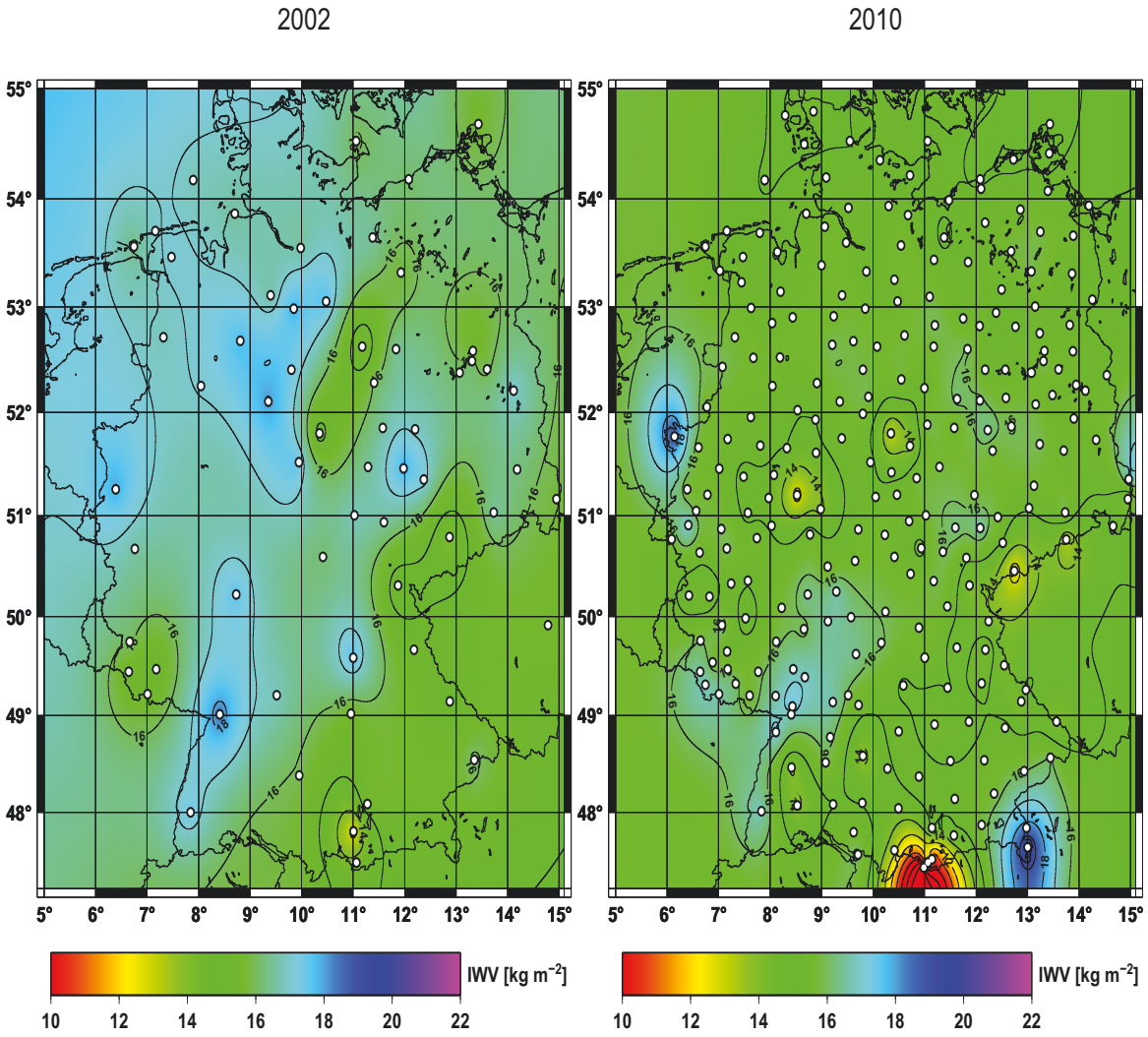

Figure 5.4: IWV annual mean values for 62 stations in 2002 (left) and for 251 stations in 2010 (right); White points are the GPS stations and the IWV values are interpolated between the stations.

5.3.1 Estimation of trends for selected stations

Based on long time series, different approaches can be selected to study the temporal and spatial variation of the water vapor distribution. IWV trend estimates are used for the long-term analysis of IWV. There is a number of different ways to quantify the trend.

Estimation using a Non-linear model

Before calculation of the trends from the IWV time series, the component for annual variations have to be investigated, especially if there are gaps in the time series. How many terms in a Fourier expansion are required to describe the annual variation of the IWV and can be investigated using the method Lomb-Scargle periodograms (William et al., 1996). The Lomb-Scargle periodogram is a method of least squares spectral analysis for unevenly spaced data (Scargle, 1982). The outputs of the Lomb-Scargle periodogram are the estimated frequency and the power spectrum for each

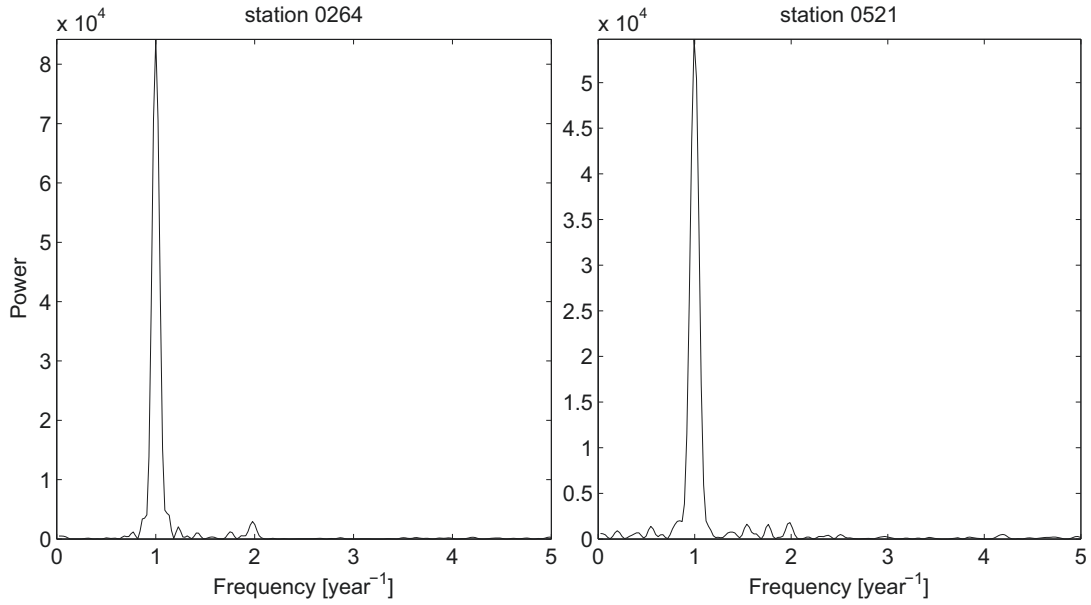

Figure 5.5: Lomb-Scargle periodograms for the IWV time series from station 0521 in Landau in der Pfalz and station 0264 in Aschau.

observation. Two examples are shown in Fig 5.5. A peak for the annual period is the most noticeable. It indicates that it is sufficient to use an annual term to describe the seasonal variations.

In order to quantify the trends from the GPS time series, a four parameter model can be used to fit the IWV time series:

$$y = IWV(t) = A_0 \cdot \sin(A_1 \cdot t) + A_2 + A_3 \cdot t \tag{5.8}$$

where t is the time in years, A_0 and A_1 are coefficients describing the amplitude and phase of the annual variations, respectively. A_2 and A_3 are the bias and linear trend of the IWV.

The time series are fitted with the non-linear four parameter equation (Eq. 5.8). The result can be divergent, if the initial values are not chosen carefully. The original time series and the fitted model are shown in Fig. 5.6. The two parameters A_2 and A_3 define a linear function (dashed line), which shows a slight increase in the IWV.

As demonstrated in Fig. 5.6 the fit follows the seasonal pattern. The fitting of the time series is uncertain, therefore, the linear least squares method is used on account of the linear method being much more robust than a non-linear four parameter fit.

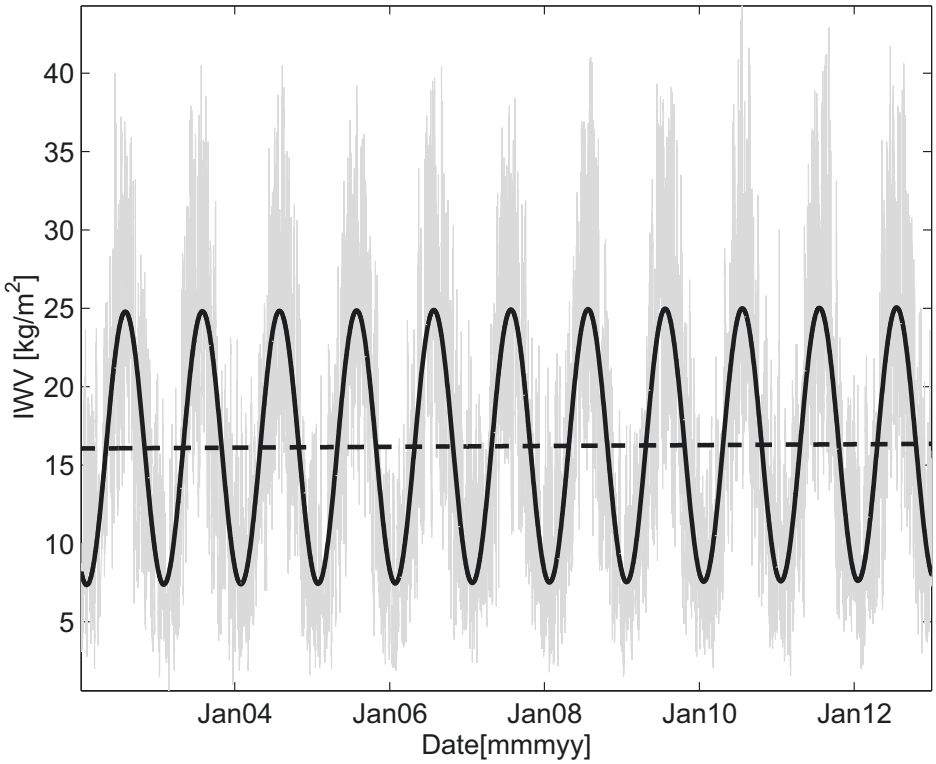

Figure 5.6: Four parameter fit for the station 0264 in Aschau for the last ten years (black line), the linear part of the fit (dashed line), and the time series data (gray line).

Estimation using a two parameter linear model

A linear model with two parameters is used to calculate the trend for each single station based on the monthly mean anomalies defined in Eq. 5.7 (Fig. 5.8):

$$y = a_0 + a_1 \cdot t \tag{5.9}$$

where t is the time in years and the coefficients a_0 and a_1 are estimated using the least squares adjustment. The Lomb-Scargle periodograms for the monthly means and monthly anomalies are also calculated (Fig. 5.7).

The Lomb-Scargle periodograms for monthly means show a peak at about one year, which is similar with the Fig. 5.5. However, no significant frequencies is found in the Lomb-Scargle periodograms for monthly anomalies. Therefore, only two parameters are used to calculate the linear trend.

The different trends are computed for each station: one trend over the entire period of time, the summer trend regarding only data in June, July, and August and the winter trend regarding only December, January, and February. One goal of the IWV trend analysis is to examine the evolution of the amount of water vapor above Germany for long periods. To achieve reliable results, only time series of 99 stations covering more than six years with data gaps smaller than three months are taken into account for the period 2002 to 2012. There are 258 stations covering a period of more than three years data with data gaps smaller than three months from 2007 to

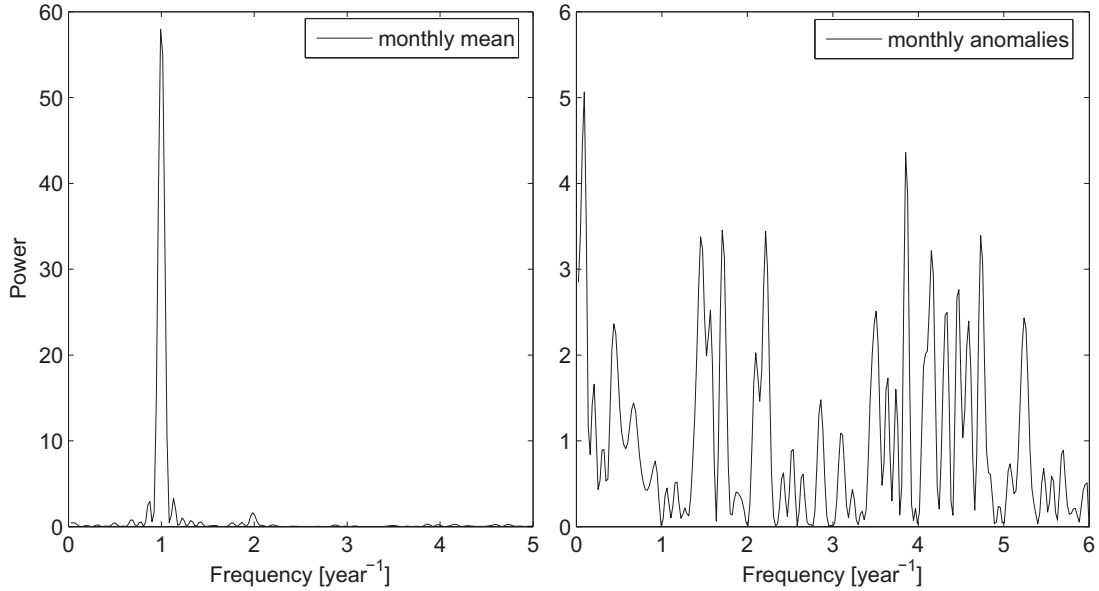

Figure 5.7: Lomb-Scargle periodograms for monthly means and monthly anomalies of station 0264 in Aschau.

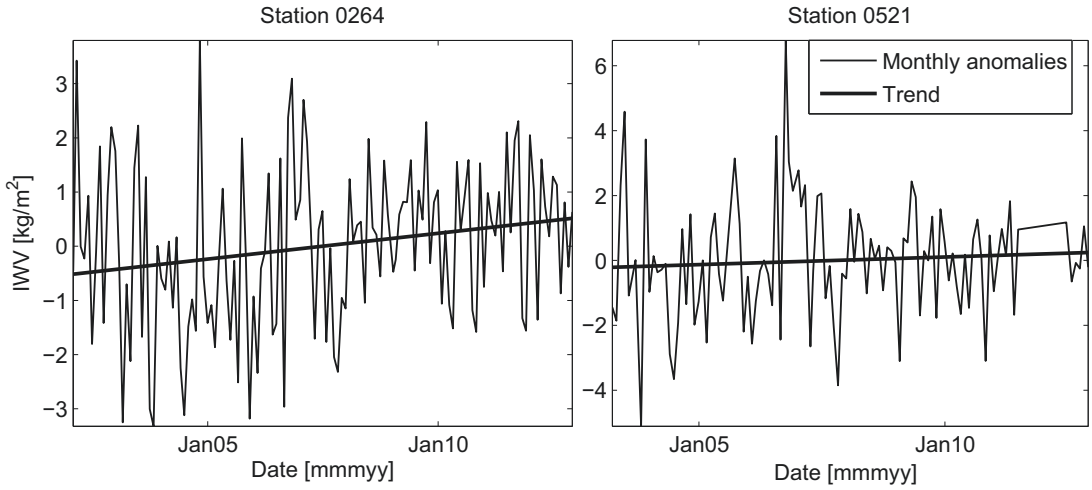

Figure 5.8: Calculated trends based on the monthly anomalies of station 0521 in Landau in der Pfalz and station 0264 in Aschau.

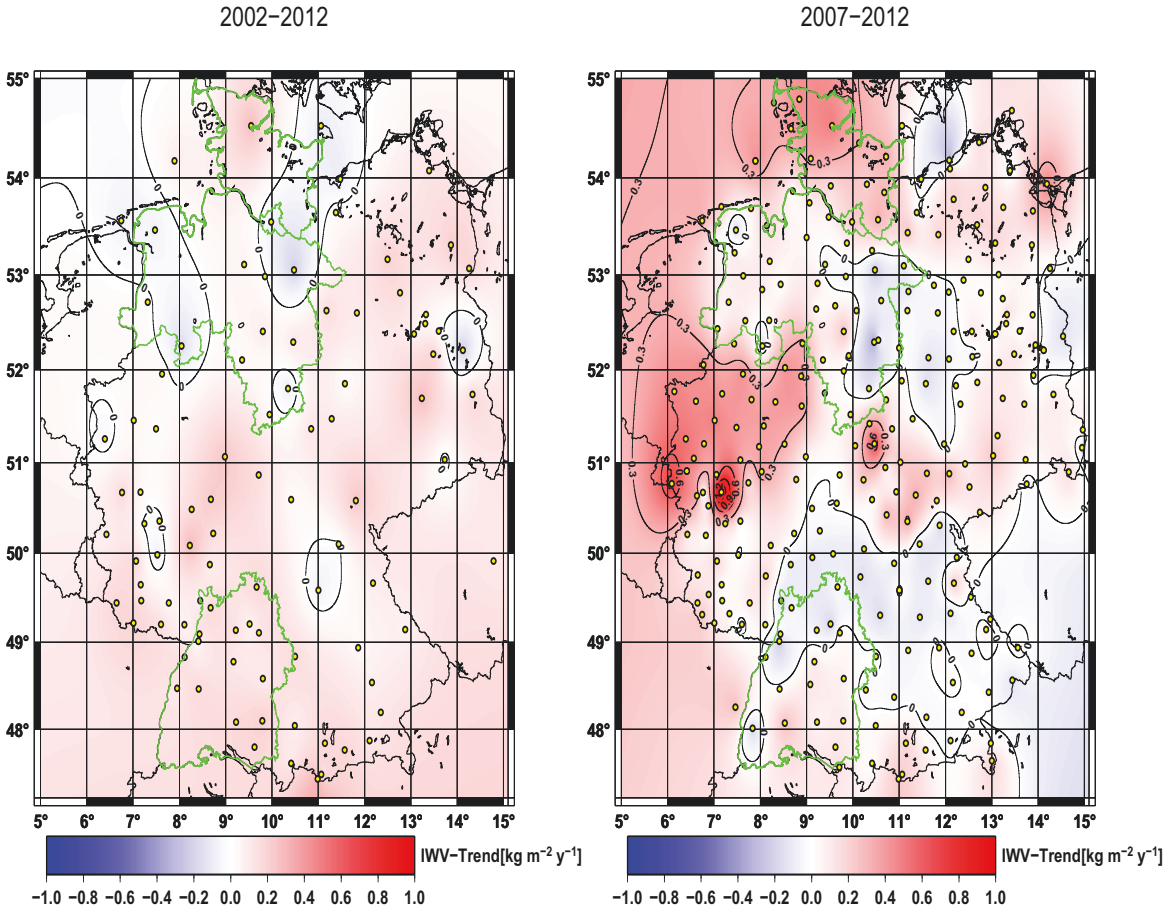

Figure 5.9: IWV trend map for the period from 2002 to 2012 (left), IWV trend map for the period from 2007 to 2012 (right); 99 stations (black circles) could be analyzed for the long period (left), 258 stations for the short period (right). The green lines indicate the federal states Schleswig-Holstein in the north, Niedersachsen in the middle and Baden-Württemberg in the south of Germany.

2012, which is more than two times of the 99 stations in the first period. The trends for both periods are shown in Fig. 5.9. The maps show IWV trend fields which are interpolated between the trends of the individual stations. The results show some discrepancies in the trends between the two periods. The trends based on the six years time series have a stronger variability and in some stations the trends are even opposite. The estimated linear trends are sensitive to the selected time period especially for such short periods. In Fig. 5.10 the IWV trends based on winter and summer anomalies from 2002 to 2012 are shown.

It appears that the trends in the winter and summer are differential in Germany with mostly positive trends in the winter and negative trends in northwest in the summer (Fig. 5.10). The amount of atmospheric water vapor almost increased in south Germany in winter and summer of the chosen period. Here, the maximum trend in the winter is 0.45 kg/(m^{2}y) and the minimum is -0.5 kg/(m^{2}y), in contrast, the maximum in the summer is 0.36 kg/m^{2}y and the minimum is -0.44 kg/(m^{2}y). This could be due to different analyzed periods or true seasonal variations in trends.

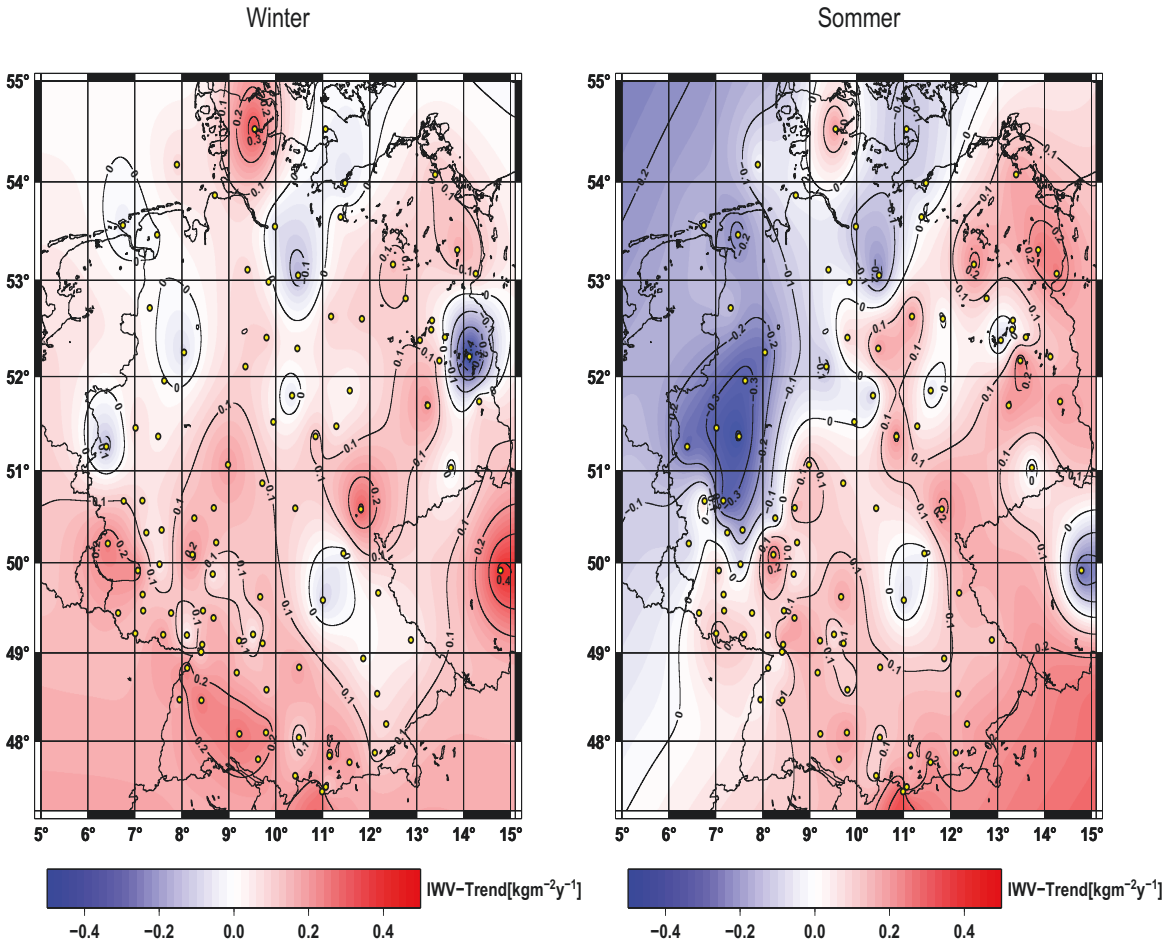

Figure 5.10: IWV winter trend map from 2002 to 2012 (left) and IWV summer trend map from 2002 to 2012 (right). 90 stations (yellow points) with more than six years of measurements with data gaps smaller than three months.

5.3.2 Comparison between GPS- and ECMWF-IWV

Changes in the instruments or in the processing software can cause significant jumps in IWV time series (Gradinarsky et al., 2002). A careful reanalysis is essential for the whole period and for all GPS stations. Within this work, non-reprocessed data are available and data from the near real-time processing has to be used. A time consuming reprocessing is necessary. To validate the results obtained with GPS data, ERA-Interim data are used from 2002 to March 2012. As mentioned in section 2.3.2, the ERA-Interim archive is composed of 6-hourly global fields with a horizontal voxel size of 0.563°x0.563°.[17] Profiles at 0, 6, 12, and 18 UTC are extracted from the ERA-Interim fields for the grid points closest to the stations. Temperature, humidity, pressure, wind information, and IWV are provided in the ERA-Interim products.

Using the IWV time series in the data sets, GPS-IWV data are compared directly with the ERA-interim IWV field. ECMWF data are independent from the quality of GPS observations since ECMWF does not assimilate ground-based GPS data. The

[17] `www.ecmwf.int/research/era/do/get/era-interim`

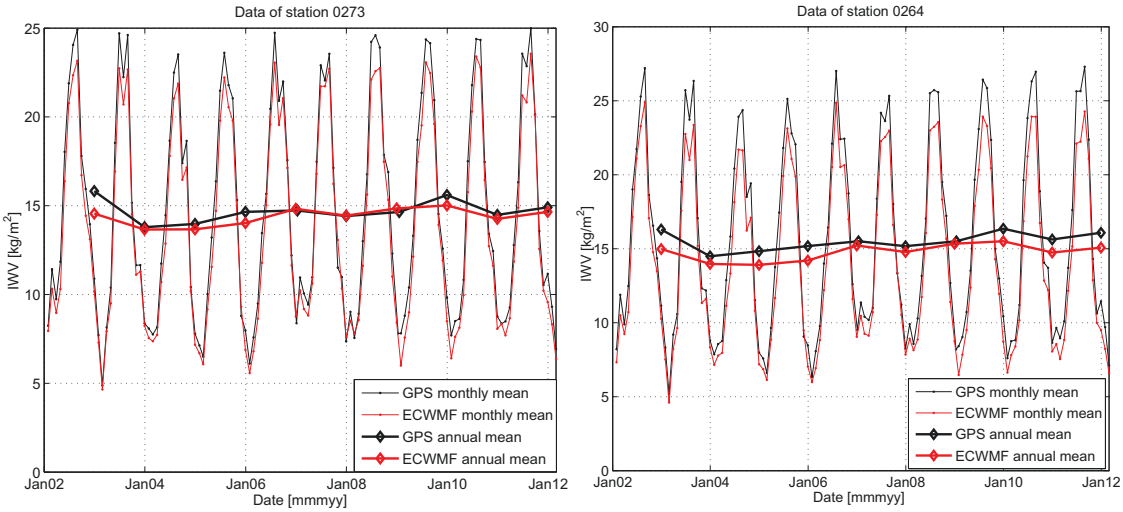

Figure 5.11: Comparison of monthly and annual means between GPS- and ECMWF-IWV from 2002 to March 2012 of station 0273 in Mindelheim and station 0264 in Aschau.

resolution of the ERA-Interim is 1.5°. Therefore, the reanalysis IWV field is not interpolated to the GPS station height to avoid a loss of information. This results in a bias, but should not affect the trend. Two stations with long continuous data are chosen as example data sets. Due to the altitude of the ECMWF surface being lower than that of the GPS station, the ERA40-IWV data show a positive bias.

Site	Mindelheim		Aschau	
Technique	GPS	ECMWF	GPS	ECMWF
Longitude	10.494°	10.5°	12.35°	12.375°
Latitude	48.042°	48°	48.195°	48.25°
Normal height[m]	625.516	765.981	459.343	609.716
Trend [kg/(m^{2}y)]	0.051	0.044	0.094	0.064

Table 5.1: Statistics of the estimated IWV trends from independent techniques for the station Aschau and Mindelheim; The normal height is defined as the height above the quasigeoid (normal gravity) along the plumb-line of the point.[18]

For monthly and annual means, significant differences between the two fields are found (Fig. 5.11). The reason is mainly due to the different temporal resolution of the two data. Compared to 6-hourly ECMWF data, the GPS sampling rate (30 min or 15 min) is obviously high. The trends of two example stations from ECMWF and GPS data are presented in Tab. 5.1. The trends are positive but show deviations of ∼33 %.

[18] `www.bkg.bund.de` (search the German height reference system)

5.4 Regional water vapor analysis

IWV time series of individual stations provide extremely detailed information for a rather limited region around the station. However, for some applications it is more important to investigate the total amount of water vapor within a given region, e.g., within the catchment area of a certain river. Regional means are required to compare the development of the atmospheric humidity in different regions, e.g., coastal regions and mountainous regions.

A method to estimate the total amount of water vapor above any desired region is therefore developed within this work. The regional mean IWV at a certain time should be obtained by computing the mean IWV observed by all stations within this region. This works well for large regions with lots of stations but for small regions with a very inhomogeneous distribution of nearby stations it is often difficult to estimate representative regional means. Therefore, it has been decided to interpolate the IWV observations of the stations on a dense horizontal grid and to estimate the water vapor within that region from the gridded IWV field. The grid should cover the desired region and nearby stations and the grid spacing should be small compared to the dimensions of the region. The total amount of water vapor as well as the regional mean IWV can easily be computed using the IWV of all grid nodes within that region. This method works for any region within a sufficiently dense GPS network even if there is not any station located within that region. It depends on the application which density of stations would be required and if data interpolated from stations outside the region provide reliable information. For example, Germany can be divided into 16 federal states (purple lines in Fig. 3.6). All the stations in different federal states can be selected using a point-in-polygon algorithm (Haines, 1994). The IWVs of all stations in the chosen regions are interpolated on dense grid cells. The total amount of water vapor is the sum of all the grid points.

To get the IWV for every grid point, the least squares collocation is used (Moritz, 1978). The least squares collocation is only an approximation, since the distribution of water vapor is highly variable and the achievable accuracy depends on the number of stations (Hirter, 1996). Equations for the least squares collocation are described in section 6.3.1. For the selected regions, the size of the grid can be set according to individual demand. The grid size 10x10 km is used as an example here. The more stations available in a given region, the more accurate are the results. For the calculation over a larger region only stations with a height below a certain threshold are used. The small IWV observations of isolated stations at high altitudes lead to strong horizontal gradients with the interpolated IWV field. In most cases, these gradients are not realistic and the IWV is underestimated. Stations at high altitudes measure lower ZTDs than the stations at low altitudes (see Fig. 5.12). The reason is the decreased atmospheric pressure with increasing altitude (Jin et al., 2007). However, the dependence of IWV on height is much more problematic to estimated as the weather has a much stronger influence on the IWV than the station altitude. Although the whole atmospheric IWV is measured, the percentage of water vapor above the tropopause (ca. 10 km) is very low. It is clear that for the same conditions a station at 50 m height has a higher IWV than the station at 1,000 m (see Fig. 5.12)

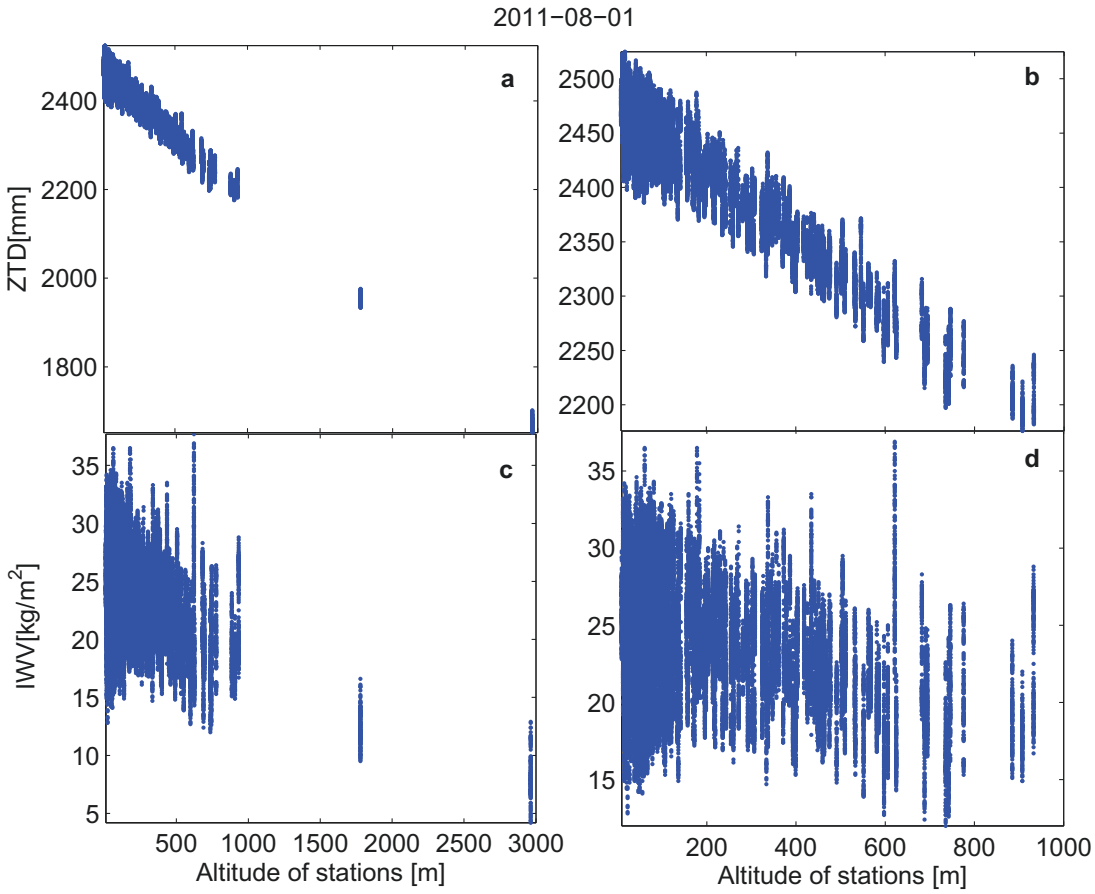

Figure 5.12: (a) and (b) are the relationship between ZTDs and altitudes of all stations and stations below 1,000 m; (c) and (d) are the relationship between IWVs and altitudes of all stations and stations below 1,000 m.

due to the thickness of air column above the station. Therefore, only the stations below the threshold are used for the horizontal interpolation.

It depends on the topography in the region if a threshold should be set and which one should be chosen. Within a flat or gently ascending terrain no height threshold is necessary but if there are GPS stations on isolated mountains it is normally better to exclude these stations. Excluding the IWV observations from stations at higher altitudes has the disadvantage that the IWV within the whole region is overestimated. The same is true for mountainous regions with no receivers in the mountains. In these cases, the interpolated IWV field needs to be modified. Two strategies are used to reduce the interpolated IWV according to the topography:

1) If there are sufficient stations in the mountains, the IWV is interpolated between the stations at the foot of the mountain and the station on top of the mountain. The linear interpolation between these stations replaces the result of collocation on the corresponding grid nodes.

2) If there are no GPS station in the mountains the topography and an empirical model suggested by Morland and Mätzler (2007) is used to reduce the IWV from

the collocation with respect to the terrain height. Both methods cannot substitute IWV observations but help to adjust the interpolated IWV field in mountainous regions. It depends on the specific situation which corrections should be applied.

Vertical IWV adjustment with stations

Firstly, all stations that are higher than the height limit, e.g., 1,000 m are chosen. For each of these stations the nearest station below the limit is determined. A linear equation is set up using these two stations. It is assumed that IWVs depend on the height of the station. In this section, the 1 arc-minute global ETOPO1 relief model[19] is used to calculate the altitude of the grid points. Then all grid points above the height limit in the radius of the half distance of the two stations are replaced with the following equation:

$$IWV_h = IWV_{h_1} + \frac{IWV_{h_1} - IWV_{h_0}}{h_1 - h_0} \cdot (h - h_1) \tag{5.10}$$

where IWV_h is the value of the grid point above 1,000 m, IWV_{h_0} is the value at the nearest GPS station below 1,000 m, IWV_{h_1} is the value of the GPS station above 1,000 m, h is the height of the grid point , h_1 is the height of the GPS station above 1,000 m and h_0 is the altitude of the nearest GPS station below 1,000 m.

Vertical IWV adjustment using an empirical model

The remaining unadjusted grid points above 1,000 m are modified using the following equation (Morland and Mätzler, 2007):

$$IWV_h = a \times IWV_{h_0} \times e^{\frac{h_0 - h}{H}} \tag{5.11}$$

where a equals 1 and H equals 2,000 m, which are empirical values given by Morland and Mätzler (2007). Different height limits can be set. However, this method has a relative large uncertainty, because IWV values of the grid points are adjusted only using the relief height and an empirical model.

To show the effect between with and without the vertical IWV adjustment, two IWV maps generated with and without data of stations above 1,000 m are shown in Fig. 5.14. To visualize the effect of the vertical IWV adjustment, maps with different corrections are shown in Fig. 5.14 and Fig. 5.15. Parts of southwestern Germany are chosen as an example because altitudes of stations vary considerably in this area (Fig. 5.13). The selected region covers the Schwäbische Alb and the Black Forest. The highest mountains are the Feldberg (1,493 m), the Hornisgrinde (1,164 m), and the Lemberg (1,015 m). The difference between the highest altitude (1,493 m) and lowest altitude (200 m) is more than 1,300 m, which is ideal for investigating the effect of height corrections. Without the vertical IWV adjustment in the mountainous region the IWV distribution looks homogeneous, but does not meet the reality (Fig. 5.14, left). Considering altitudes above 1,000 m, the mountain peaks of the Black Forest near the Feldberg are visible in the Fig. 5.14 (right). Figure 5.14 (left) show the interpolated IWV field using the stations below 1,000 m (white circles). The stations above 1,000 m (red circles) provide IWV observations which are considerably smaller. After applying the first vertical IWV adjustment method the IWV

[19] www.ngdc.noaa.gov/ngdc.html

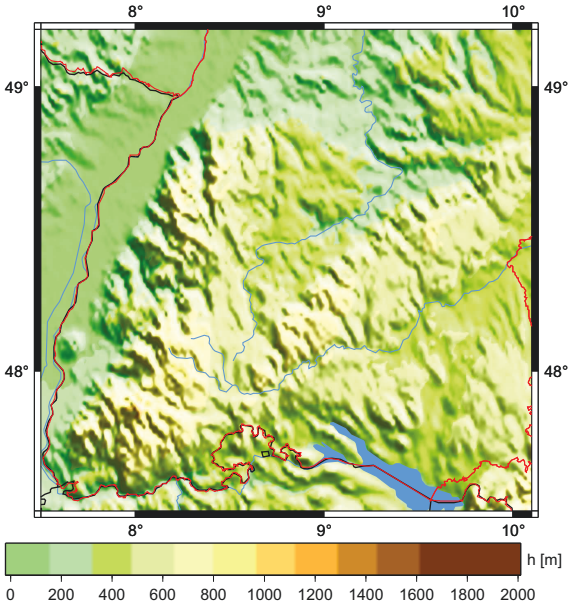

Figure 5.13: Altitude map of the southwestern part of Germany, covering the Black Forest, the Schwäbische Alb, and the Bodensee (Müller, 2011).

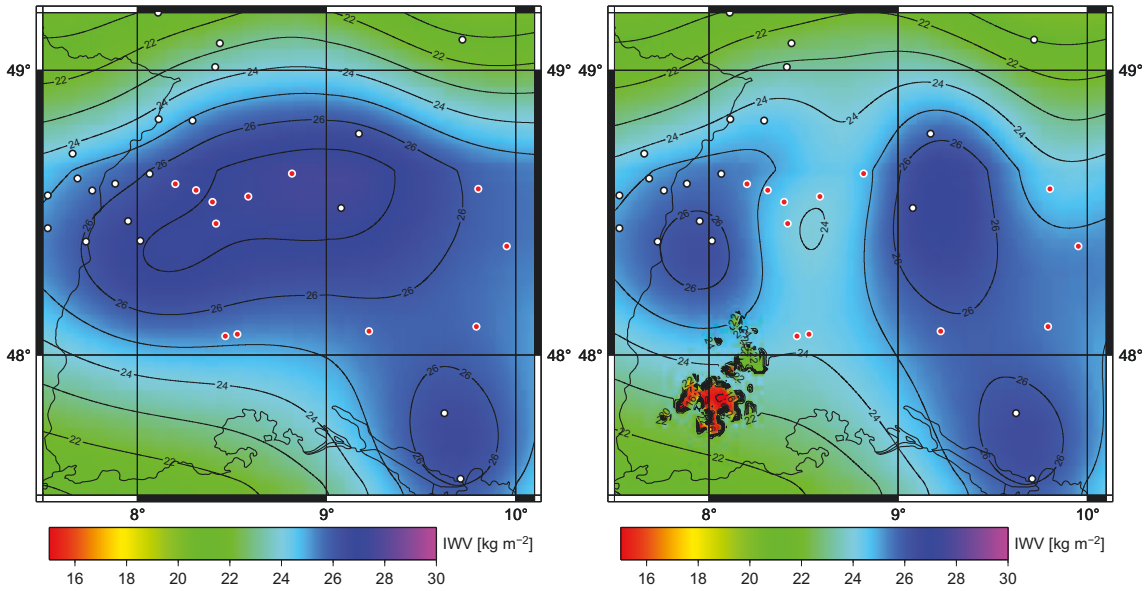

Figure 5.14: IWV map only with the horizontal collocation of stations below 1,000 m (left) and IWV map with the vertical IWV adjustment using data of stations above 1,000 m (right). White circles are stations below 1,000 m and red are stations above 1,000 m (Müller, 2011).

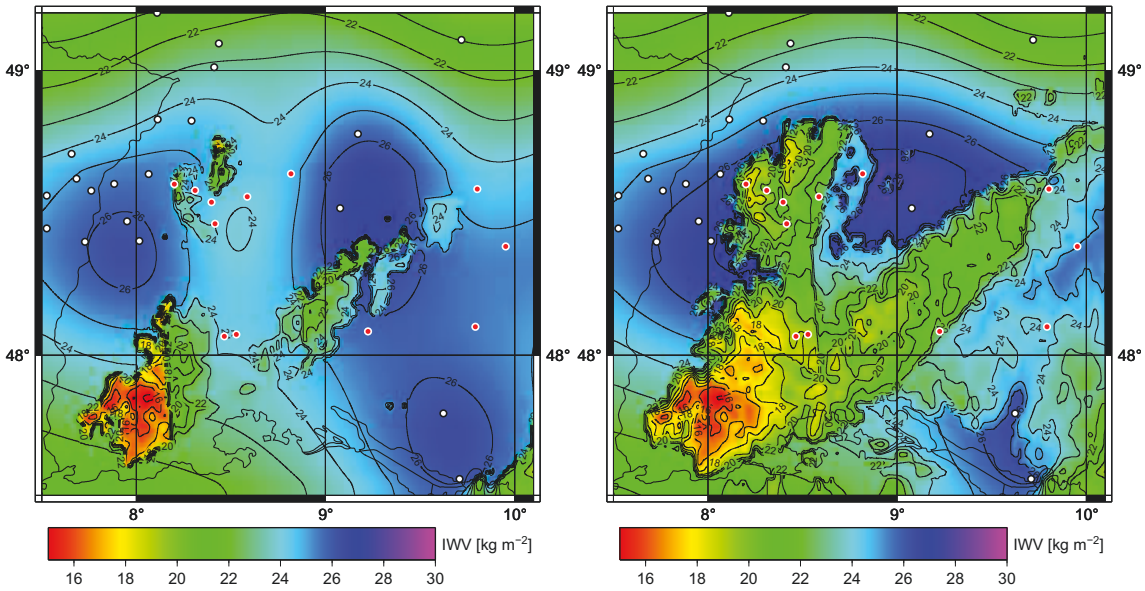

Figure 5.15: IWV map with the vertical IWV adjustment using the height limit 750 m (left) and 500 m (right), white circles are stations below 1,000 m and red circles are stations above 1,000 m (Müller, 2011).

field is considerably modified (Fig. 5.14, right) in the Black Forest. The impact using the second empirical model can be seen in the lower left part of Fig. 5.14 (right). The IWV field is modified according to the topography for altitudes above 1,000 m. Fig. 5.15 shows the impact of the different height limit. Using only stations below 750 m (Fig. 5.15, left) or 500 m (Fig. 5.15, right), does not change considerably the result of the horizontal interpolation and the subsequent adjustment with the first method. However, the second method leads to considerable modifications according to the topography.

The lower the height limit is, the more clearly relief is shown in the map. With a height limit of 750 m further details of the Black Forest are found (details of the Schwäbische Alb in the east). With the height limit of 500 m a large part of the region shows the adjusted values and the relief is easy to distinguish (Fig. 5.15). The more grid points and stations above the height limit are, the more adjusted values need to be calculated. The IWV distributions are different in Fig. 5.14 and in Fig. 5.15 with a large impact of the relief on the IWV distribution.

5.4.1 Estimation of regional water vapor trends

To demonstrate the applicability of the regional analysis described above, three different regions in Germany were investigated: A coastal region in the North (Schleswig-Holstein), a flat region in central Germany (Niedersachsen), and a mountainous region in the South (Baden-Württemberg) (green lines in Fig. 5.9). The regional mean IWV is computed for these three regions and from the period 2002 to 2012. From these data the monthly and annual means (Fig. 5.16, left) and the monthly anomalies (Fig. 5.16, right) are derived.

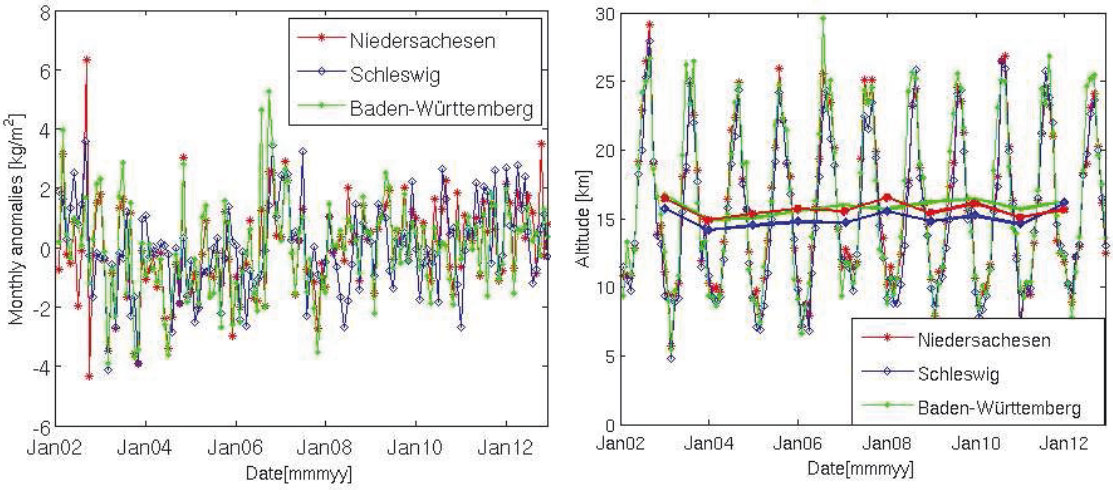

Figure 5.16: IWV monthly means from 2002 to 2012 for Schleswig-Holstein, Niedersachsen, and Baden-Württemberg (left), IWV annual means from 2002 to 2012 with fat lines; IWV monthly mean anomalies (see Eq. 5.7) (right).

The time series reflect the previously determined trends of individual stations within these regions. The trends of the past 11 years in Baden-Württemberg, Niedersachsen, and Schleswig-Holstein are partly different to the trends of the last six years (Tab. 5.2).

Trend[kg/(m^{2}y)]	2002 to 2012	2007 to 2012
Baden-Württemberg	0.06	0.117
Niedersachsen	-0.009	-0.008
Schleswig-Holstein	0.080	0.080

Table 5.2: IWV Trends of three federal states in Germany Baden-Württemberg, Niedersachsen, and Schleswig-Holstein.

In 2007 the EPOS parameters were changed particularly the sampling rate was increased to 15 min. Changes in the software settings can significantly affect the estimates and cause remarkable jumps in the time series. The visible strong change of the annual mean for 2007 (the point at January 2008) in Fig. 5.16 could be possibly caused by the parameter change of the software. The annual means of IWV in Schleswig-Holstein, which is a coastal region, are below those values in Baden-Württemberg and Niedersachsen (Fig. 5.16). The coastal region is relatively flat (Niedersachsen and Schleswig-Holstein), whereas Baden-Württemberg is a mountainous region.

For the regional analysis, the reprocessing is especially required for all stations in the chosen region, otherwise the jumps could have a more strong effect on the results than on the individual station.

6 GPS tomography

A water vapor tomography system was developed at GFZ (Bender et al., 2011a), which uses undifferenced observations from the GNSS receiver network. The system is designed to process the slant path delays of about 300 German GNSS stations in near real-time (currently only limited to GPS). Two implementations of the reconstruction techniques are used to invert the linear inverse problem in this chapter: a Kalman filter and an iterative reconstruction technique (MART). To determine the quality of the GPS tomography, more than 8,000 RS profiles for 2007 are used for the validation. Before the validation, the temporal and spatial distribution of the slant paths, entering the tomographic reconstructions, as well as their angular distribution are studied. However, only GPS derived STDs are used as input for the tomography. In the near future, GNSS water vapor tomography will be reconstructed with GNSS-STDs.

6.1 Inverse problem

The GPS tomography combines a large number of STDs in order to reconstruct a spatially reconstructed refractivity field. In many cases, it is more desirable to obtain the humidity distribution, which is closely related to the wet refractivity and SWDs. The STD (Eq. 3.12) can be subdivided into a hydrostatic and a wet part, the latter being related to the water vapor. The SWD can be separated from the STD by estimating the SHD using the ZHD (Eq. 3.18). The ZHD can be mapped onto the slant path using the hydrostatic mapping function (Niell, 1996; Böhm et al., 2006):

$$SHD = m_h ZHD \tag{6.1}$$

and the SWD is related to the wet refractivity field by the integral along the signal path, given by the difference between the STD and the SHD (see section 3.3):

$$SWD = 10^{-6} \int_s N_w ds = STD - SHD. \tag{6.2}$$

To solve the integral, the curvature of the signal path is neglected. This problem can be discretized using a regular grid of geographic coordinates and linearized by assuming that the signal path does not depend on N_w within each cell:

$$SWD = 10^{-6} \sum_i N_w^i s_i \tag{6.3}$$

where s_i is the subpath within the grid cell i. Equation 6.3 leads to a system of linear equations, if all SWD observations available are combined to a vector $\mathbf{m}$. Then the refractivity field $\mathbf{N_w}$ is mapped on a vector $\mathbf{n}$ and the design matrix $\mathbf{A}$ is given by the slant subpaths in each voxel:

$$\mathbf{m} = \mathbf{An}. \tag{6.4}$$

$\mathbf{A}$ is a large sparse matrix with q rows and p columns, with q being the number of slants and p being the number of grid nodes.

The question to find $\mathbf{n}$ with known $\mathbf{A}$ and $\mathbf{m}$ in Eq. 6.4 is an inverse problem. In general, a solution $\mathbf{n}$ of Eq. 6.4 will not be unique or does even not exist. An alternative for it is minimizing the norm $\tilde{n}$:

$$\min\{\|A\mathbf{n} - \mathbf{m}\|\}. \tag{6.5}$$

To solve inverse problems, different methods are developed. The singular value decomposition is a powerful technique (William et al., 1996). Schwintzer (1990), Koch and Kusche (2002), and Xu et al. (2006) use the approach of the regularization techniques to solve the ill-posed problem. The damped least squares method is implemented in Hirahara (2000) and Noguchi et al. (2004). The Kalman filter and algebraic reconstruction techniques (ART) are used in this work and described in detail in section 6.2.

The solution $\mathbf{n}$ depends to a large extent on the matrix $\mathbf{A}$ which defines the linear mapping from state space to observation space. $\mathbf{A}$ is a p×q matrix and sparse as each signal propagates only through a limited number of voxels. The number of observed STDs is independent from the number of grid nodes and $\mathbf{A}$ is a rectangular matrix with $p > q$ or $q > p$.

The system of linear equations might be underdetermined in some regions and overdetermined in others, due to the irregular distribution of STDs. As a consequence, the ill-posed problems are effectively underdetermined and the solution is not stable and unique (Hansen, 1992). An ill-posed problem leads to an ill-conditioned matrix $\mathbf{A}$, i.e. the inversion of $\mathbf{A^{-1}}$ or $(\mathbf{A^T A})^{-1}$ is unstable and unbounded. Even small errors in the observations could be greatly amplified in the solution by the unbounded inversions. Hence, the least squares solution could lead to a meaningless result. Additionally an ill-conditioned matrix $\mathbf{A}$ amplifies the errors within the system of linear equations, such as the discretization error in $\mathbf{A}$ and $\mathbf{m}$, error of linearization in $\mathbf{A}$, observation error in $\mathbf{m}$, and the rounding error of the inversion algorithm. Therefore, techniques are required, which lead to a stable result and select one solution out of the infinite number of possible solutions of the effectively underdetermined problem (Hansen, 1992).

6.2 Reconstruction techniques

In this chapter, two of the approaches for the tomographic reconstruction with GPS data are chosen to solve the ill-posed inverse problem. One is based on the Kalman filter technique, the other is an iterative technique from the ART family.

6.2.1 ART

ART was first introduced by Gordon et al. (1970) for a computed tomography application. The algorithms of the ART family are classified in several major groups, e.g., additive ART (simple ART), Multiplicative ART (MART), and Simultaneous ART (SART). ART is an iterative procedure for solving a set of linear equations. No matrix inversion has to be performed and it is not even necessary to create the

large sparse matrix $\mathbf{A}$ in computer memory. Only the two vectors $\mathbf{n}$, $\mathbf{m}$ and a data structure containing the slant subpaths in each voxel are required to solve the equations. This leads to an efficient application of computer memory and computing time. The original ART algorithm can be stated as follows (Kak and Slaney, 2001):

$$n_j^{k+1} = n_j^k + \lambda \frac{m_i - \langle \mathbf{A^i}, \mathbf{n^k} \rangle}{\langle \mathbf{A^i}, \mathbf{A^i} \rangle} \mathbf{A^i} \tag{6.6}$$

where j denotes the grid cell, i the observation, k the iteration step, and λ is the relaxation parameter for all iterations. The vector $\mathbf{A^i}$ is taken from the row i of the kernel matrix $\mathbf{A}$. A correction weighted by this term and the relaxation parameter λ is applied to the grid cell j. Within each step of the iteration this is repeated for all cells j and all observations i.

A modified version of ART is the MART, where the correction in each iteration is obtained by making a multiplicative modification to $\mathbf{n}$. Through numerical experiments, the best value of the relaxation parameter was determined to provide the fastest, most flexible and accurate results (Verhoeven, 1993; Subbarao et al., 1997). MART has successfully been used to reconstruct the total electron content of the ionosphere (Stolle et al., 2006; Jin et al., 2008). This technique combines high numerical stability even under bad conditions with computational efficiency:

$$n_j^{k+1} = n_j^k \frac{m_i}{\langle \mathbf{A^i}, \mathbf{n^k} \rangle}^{\frac{\lambda A_j^i}{\sqrt{\langle \mathbf{A^i}, \mathbf{A^i} \rangle}}}. \tag{6.7}$$

In contrast to the ART, the inversion results are always positive if inputs $\mathbf{A}$ and $\mathbf{n}$ have non-negative entries. Therefore, MART has the advantage over ART in determining the wet refractivities that avoid unreasonable negative values.

The simultaneous iterative reconstruction technique (SART) has originally been developed by Gilbert (1972) and further refined by, e.g., Andersen and Kak (1984) and Hobiger et al. (2008). Compared to MART the reconstruction with SART does not depend on the order of the observations within the vector $\mathbf{m}$:

$$n_j^{k+1} = n_j^k + \sum_i \lambda \frac{m_i - \langle \mathbf{A^i}, \mathbf{n^k} \rangle}{\langle \mathbf{A^i}, \mathbf{A^i} \rangle}. \tag{6.8}$$

To stop the iteration and to check the convergence to a stable solution, different parameters can be used to estimate the quality of reconstruction (Bender et al., 2011a), e.g., the relative deviation:

$$\Delta_1 = \frac{\sqrt{\sum_i (n_j^{k+1} - n_j^k)^2}}{\sqrt{\sum_i (n_j^k)^2}}. \tag{6.9}$$

$\Delta_1 < \upsilon$ can be used as stop criteria. If the difference of relative deviations is smaller than the set υ, the iterations will be stopped. However, a small difference does not always indicate a good reconstruction. Sometimes the result can become worse even

with smaller Δ_1. None of these criteria leads to reliable results under ill-conditions. Therefore, a fixed predefined number of iterations is often used.

Using the existing tomography package developed by Bender et al. (2011a), the three algorithms are tested for the generation of the tomography. However, SART and MART have comparable results and only ART shows poorer results due to the derived negative values. MART is tested as the fastest method with relative good results.

In ART algorithms, the relaxation parameter λ gives the weight of the correction term computed for each voxel with respect to the initial voxel value. Large values of λ lead in most cases to faster convergence but also to more pronounced artifacts in the resulting field and can sometimes initiate oscillations. As λ strongly influences both the quality of the reconstructed field and the convergence behavior, the best $\lambda = 0.2$ is used according to Stolle et al. (2006) and Bender et al. (2011a).

The ART algorithms generate rather good results rapidly and only two parameters (relaxation parameter λ and the number of iterations) need to be determined. The ART methods start with an initial field, which is iteratively improved by applying small corrections to each grid cell. Therefore, the initial field plays a very important role. However, these are only empirical methods without a solid theoretical derivation. Furthermore, no error information of the results is provided and no error statistic is used. The stop criteria are not confident and unreliable results can appear because of ill-posedness.

6.2.2 Kalman filter

As mentioned above, the ART algorithms have some disadvantages. In contrast, the Kalman filter technique is adopted for ill-posed inverse problems because of its good capability to estimate dynamically changing parameters. Furthermore, the error covariances of the states and the observations are taken into account and the posteriori state error covariance matrix is derived. Fundamental requirements for a good performance of the Kalman filter are the proper error models for observations as well as for the model state variables.

In the Kalman filter, the refractivities for consecutive time steps $\mathbf{n_k}$ and $\mathbf{n_{k+1}}$ are related through the state propagation matrix $\mathbf{F}$. $\mathbf{n_k}$ is the state vector (the humidity field) at epoch k. The following dynamic model is assumed (Gelb, 1974), which defines the prediction step from time t_k to t_{k+1}:

$$\hat{\mathbf{n}}_{\mathbf{k+1}} = \mathbf{F}\mathbf{n}_{\mathbf{k}} \tag{6.10}$$

$$\hat{\mathbf{P}}_{\mathbf{k}} = \mathbf{F}\mathbf{P}_{\mathbf{k}}\mathbf{F}^{\mathbf{T}} + \mathbf{Q}. \tag{6.11}$$

In the correction step, the current state $\hat{\mathbf{n}}_{\mathbf{k+1}}$ is combined with the latest observations $\mathbf{z_{k+1}}$ leading to an improved state:

$$\mathbf{n}_{\mathbf{k+1}} = \hat{\mathbf{n}}_{\mathbf{k+1}} + \mathbf{G}_{\mathbf{k+1}}(\mathbf{z}_{\mathbf{k+1}} - \mathbf{A}_{\mathbf{k+1}}\hat{\mathbf{n}}_{\mathbf{k+1}}) \tag{6.12}$$

$$\mathbf{P}_{\mathbf{k+1}} = (\mathbf{I} - \mathbf{G}_{\mathbf{k+1}}\mathbf{A}_{\mathbf{k+1}})\hat{\mathbf{P}}_{\mathbf{k+1}} \tag{6.13}$$

$$\mathbf{G}_{\mathbf{k+1}} = \hat{\mathbf{P}}_{\mathbf{k}}\mathbf{A}^{\mathbf{T}}_{\mathbf{k+1}}(\mathbf{R}_{\mathbf{k+1}} + \mathbf{A}_{\mathbf{k+1}}\hat{\mathbf{P}}_{\mathbf{k}}\mathbf{A}^{\mathbf{T}}_{\mathbf{k+1}})^{-1} \tag{6.14}$$

where $\mathbf{P_{k+1}}$ is the error covariance matrix of the state $\mathbf{n_{k+1}}$. $\mathbf{Q}$ reflects the uncertainty of the propagation and $\mathbf{R_{k+1}}$ is the observation error covariance matrix. $\mathbf{z_{k+1}}$ is the set of measurements, $\mathbf{A_{k+1}}$ is the measurement matrix and $\mathbf{G_{k+1}}$ is the Kalman gain matrix at the time t_{k+1}.

The water vapor tomography could be reconstructed using a Kalman filter, which runs continuously and estimates the latest state epoch by epoch. Firstly, the Kalman filter starts with an initial field $\mathbf{n_0}$ with the error covariance matrix $\mathbf{P_0}$. The estimations can be renewed with new observations $\mathbf{z_{k+1}}$ and their error covariance $\mathbf{R_{k+1}}$ in the update step. The Kalman gain matrix $\mathbf{G_{k+1}}$ is calculated with the inversion of matrix using the LU factorization described by Barker (2001). The predicted state $\hat{\mathbf{n}}_{\mathbf{k+1}}$ is mapped by the observation matrix $\mathbf{A}$ into the state of the observations and compared to measurements. Based on the comparison, the new estimate is derived with the Kalman gain matrix. $\mathbf{P_{k+1}}$, containing the information of the accuracy of the estimate, is also derived. The advantage of the Kalman filter is, that it is easy to calculate with the exception of the matrix inversion. It is also proved to be a optimal estimator for linear systems (Kalman et al., 1960). However, the limitations of the Kalman filter are the strong assumptions. Many systems are non-linear models and the error terms and the measurements may have no Gaussian distribution.

6.3 Reconstruction of the $\mathbf{N_w}$ fields

The current investigation is based on the EPOS tropospheric products of the German ground GPS network. In Fig. 6.1 the 272 utilized GPS stations, which build a dense network for the GPS tomography, are shown. The horizontal resolution of the generated tomography is about 50 km, which is limited by the mean GPS inter-station distance of about 40 km. The tomography based on the Kalman filter is developed within this work while the tomography based on the MART technique is part of the tomography package. The reconstruction region for both methods is the same, which covers the region from longitude 4.9° to 15°, latitude 47.3° to 54.8° with the grid described in Fig. 6.1, and the height is from 0 to 10,000 m with 20 equal intervals.

6.3.1 GPS tomography based on MART

The wet refractivities are obtained with MART (see Eq. 6.7) for 2007. For the MART method, to adjust the robustness to unstable solution of several ill-posed inverse problems, a diverse number of iterations number can be used. Too few iterations will include little information about the change of refractivity but on the other hand too many iterations will destroy the balance between the weight of observations vs. background. 100 to 200 iterations are suitable for MART methods according to Bender et al. (2011a). 100 iterations are used here and the temporal resolution is 30 min. Additional observations (IWV, synoptic data, inter-voxel constraints) are used to stabilize the tomographic reconstruction.

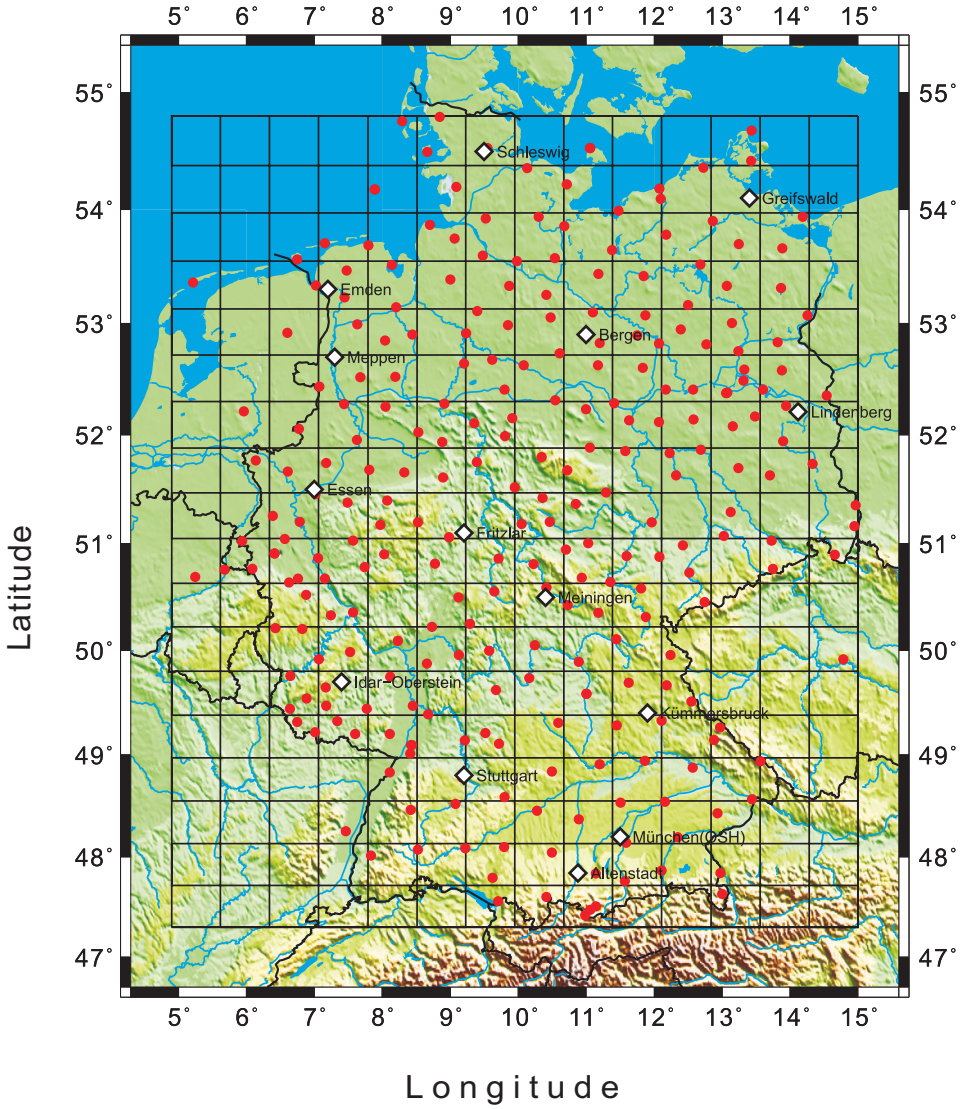

Figure 6.1: Location of the 272 GPS receiver sites (red dots) inside the tomography grid (black) and the German radiosonde stations (white rhombuses). There are no data for station Altenstadt in the year 2007. 14x18x20 cell grid is chosen for the reconstruction.

Initialization

Several methods, e.g., the standard atmosphere or a forecast of a numerical weather model can provide an initial state for the reconstruction. However, the standard atmosphere is usually not very close to the time state. Also weather forecasts with a good spatial resolution are not available in near real-time. Synoptic observations of the DWD are therefore used to estimate the initial state by interpolating the observation horizontally on the lowest grid layer and by extrapolating these data vertically on each grid column. This can be done in near real-time as the synoptic data are provided by the DWD on an hourly basis.

The least squares collocation (Moritz, 1978) is used for the horizontal interpolation:

$$\mathbf{y} = \hat{\mathbf{A}}\mathbf{b} + \mathbf{s} + \mathbf{n} \tag{6.15}$$

where $\mathbf{y}$ is the observation vector, $\mathbf{b}$ is the vector of model parameters, and $\hat{\mathbf{A}}$ is the design matrix of the model depending on the positions of the measurements. The $\mathbf{s}$ describes systematic deviations from the model (signal) and $\mathbf{n}$ is the white noise. The solution is given by the least squares adjustment with the covariance matrix of the noise $\mathbf{C_{nn}}$ and the the signal $\mathbf{C_{ss}}$:

$$\begin{aligned}
\mathbf{b} &= (\hat{\mathbf{A}}^{\mathbf{T}}(\mathbf{C_{nn}} + \mathbf{C_{ss}})\hat{\mathbf{A}})^{-1}\hat{\mathbf{A}}^{\mathbf{T}}(\mathbf{C_{nn}} + \mathbf{C_{ss}})^{-1}\mathbf{y} && (6.16)\\
\mathbf{n} &= \mathbf{C_{nn}}(\mathbf{C_{nn}} + \mathbf{C_{ss}})^{-1}(\mathbf{y} - \hat{\mathbf{A}}\mathbf{b}) && (6.17)\\
\mathbf{s} &= \mathbf{C_{ss}}(\mathbf{C_{nn}} + \mathbf{C_{ss}})^{-1}(\mathbf{y} - \hat{\mathbf{A}}\mathbf{b}). && (6.18)
\end{aligned}$$

The interpolation at additional points could be determined using the covariance vector $\mathbf{C_{ss'}}$ between the observed values and the interpolated values:

$$\begin{aligned}
\mathbf{d'} &= \hat{\mathbf{A}}'\mathbf{b} + \mathbf{s'} && (6.19)\\
\mathbf{s'} &= \mathbf{C_{ss'}}(\mathbf{C_{nn}} + \mathbf{C_{ss}})^{-1}(\mathbf{y} - \hat{\mathbf{A}}\mathbf{b}). && (6.20)
\end{aligned}$$

This model is improved as a numerical approximation method with parameter estimation and statistical interpolation of observations in space and time (Hirter, 1996; Troller et al., 2006):

$$P(x, y, z, t) = (P_0 + a_P(x - x_0) + b_P(y - y_0) + c_P(t - t_0))\exp(-\frac{z - z_0}{H_P}). \tag{6.21}$$

For the given value of the reference height $z_0 = 0\,\mathrm{m}$, the reference horizontal coordinates x_0, y_0, and the reference time t_0 are the mean values of all measurement locations and times. a_P and b_P are horizontal gradients and c_P is the temporal gradient. H_P is the scale height and P_0 is the pressure at the reference point. The design matrix of the pressure is given by:

$$\mathbf{y} = \hat{\mathbf{A}}\mathbf{b} = \tag{6.22}$$

$$\begin{pmatrix}
\exp(\frac{z_1 - z_0}{-H_P}) & \exp(\frac{z_1 - z_0}{-H_P})(x_1 - x_0) & \exp(\frac{z_1 - z_0}{-H_P})(y_1 - y_0) & \exp(\frac{z_1 - z_0}{-H_P})(t_1 - t_0)\\
\exp(\frac{z_2 - z_0}{-H_P}) & \exp(\frac{z_2 - z_0}{-H_P})(x_2 - x_0) & \exp(\frac{z_2 - z_0}{-H_P})(y_2 - y_0) & \exp(\frac{z_2 - z_0}{-H_P})(t_2 - t_0)\\
\dots & \dots & \dots & \dots\\
\exp(\frac{z_N - z_0}{-H_P}) & \exp(\frac{z_N - z_0}{-H_P})(x_N - x_0) & \exp(\frac{z_N - z_0}{-H_P})(y_N - y_0) & \exp(\frac{z_N - z_0}{-H_P})(t_N - t_0)
\end{pmatrix}
\begin{pmatrix} P_0 \\ a_P \\ b_P \\ c_P \end{pmatrix}.$$

For a given value of $H_P = 8,000\,\mathrm{m}$, P_0 can be estimated with:

$$P_0 = \frac{1}{N}\sum_{i=1}^{N}\frac{P_{obs,i}}{\exp(-\frac{z_i - z_0}{H_P})}. \tag{6.23}$$

This quantity is used in Eq. 6.22 and can be removed leading to a new observation P_2:

$$P_{obs} = (P_0 + P_2)\exp(-\frac{z - z_0}{H_P}) \longleftrightarrow P_2 = \frac{P_{obs}}{\exp(-\frac{z_1 - z_0}{H_P})} - P_0. \tag{6.24}$$

The least squares collocation could be carried out with P_2 and the simplified model function:

$$P_2(x, y, t) = a_P(x - x_0) + b_P(y - y_0) + c_P(t - t_0) \tag{6.25}$$

with the new design matrix:

$$\mathbf{y_2} = \hat{\mathbf{A}}_\mathbf{2}\mathbf{b_2} = \begin{pmatrix} (x_1 - x_0) & (y_1 - y_0) & (t_1 - t_0) \\ (x_2 - x_0) & (y_2 - y_0) & (t_2 - t_0) \\ \dots & \dots & \dots \\ (x_N - x_0) & (y_N - y_0) & (t_N - t_0) \end{pmatrix} \begin{pmatrix} a_P \\ b_P \\ c_P \end{pmatrix}. \tag{6.26}$$

If no temporal variation is considered, only two parameters a_P and b_P have to be estimated. To compare the results of the least squares collocation $y_{2,est}$ with the real observations, the removed part has to be added:

$$P_{est} = P_0 + y_{2,est}\exp(-\frac{z - z_0}{H_P}). \tag{6.27}$$

The partial pressure of water vapor e uses the same model as the pressure:

$$e(x, y, z, t) = (e_0 + a_e(x - x_0) + b_e(y - y_0) + c_e(t - t_0))\exp(-\frac{z - z_0}{H_e}). \tag{6.28}$$

The reference coordinates and time are the same. a_e, b_e, c_e, e_0 are fitted using the same method as above. The scale height $H_e = 3,000\,\mathrm{m}$ here. The model function for the temperature T is given by:

$$T(x, y, z, t) = T_0 + a_T(x - x_0) + b_T(y - y_0) + c_T(t - t_0) + \gamma(z - z_0) \tag{6.29}$$

where γ is the vertical gradient and T_0 is the temperature at the reference point. The design matrix of the temperature $\mathbf{y}$ is written as follows:

$$\mathbf{y} = \hat{\mathbf{A}}\mathbf{b} = \begin{pmatrix} 1 & (x_1 - x_0) & (y_1 - y_0) & (t_1 - t_0) & (z_1 - z_0) \\ 1 & (x_2 - x_0) & (y_2 - y_0) & (t_2 - t_0) & (z_2 - z_0) \\ 1 & \dots & \dots & \dots & \dots \\ 1 & (x_N - x_0) & (y_N - y_0) & (t_N - t_0) & (z_N - z_0) \end{pmatrix} \begin{pmatrix} T_0 \\ a_T \\ b_T \\ c_T \\ \gamma \end{pmatrix}. \tag{6.30}$$

However, the vertical gradient γ cannot be estimated from surface observations with sufficient accuracy. In this case, γ can be assumed to be 0.0064 K/m and removed in the observations $T(x, y, z, t)$. The model function becomes:

$$T_2(x, y, t) = T_0 + a_T(x - x_0) + b_T(y - y_0) + c_T(t - t_0) \tag{6.31}$$

with the new design matrix:

$$\mathbf{y_2} = \hat{\mathbf{A}}_\mathbf{2}\mathbf{b_2} = \begin{pmatrix} 1 & (x_1 - x_0) & (y_1 - y_0) & (t_1 - t_0) \\ 1 & (x_2 - x_0) & (y_2 - y_0) & (t_2 - t_0) \\ 1 & ... & ... & ... \\ 1 & (x_N - x_0) & (y_N - y_0) & (t_N - t_0) \end{pmatrix} \begin{pmatrix} T_0 \\ a_T \\ b_T \\ c_T \end{pmatrix}. \tag{6.32}$$

T_0 are the mean values of all the measurements and a_T, b_T, c_T are fitted. To get the required temperature values, the term $\gamma(z - z_0)$ has to be added.

The noise covariance matrix $\mathbf{C_{nn}}$ is assumed to be a diagonal matrix with $\sigma_{noise} = 0.5$ (hPa for the pressure and K for the temperature). The covariance matrix $\mathbf{C_{yy}}$ is computed from the covariance depending on the spatial and temporal distance between two locations (Troller et al., 2006):

$$\Phi_{ij} = \frac{\sigma^2_{obs}}{1 + (\frac{x_i - x_j}{\Delta x_0})^2 + (\frac{y_i - y_j}{\Delta y_0})^2 + (\frac{z_i - z_j}{\Delta z_0})^2 + (\frac{t_i - t_j}{\Delta t_0})^2} \tag{6.33}$$

where the variance of observations σ_{obs} =0.5 hPa (pressure) or 0.5 K (temperature), the correlation length of the observations are set to $\Delta x_0 = 450$ km, $\Delta y_0 = 450$ km, $\Delta z_0 = 60$ km, $\Delta t_0 = 0.08$ h. x_i, y_i, z_i, t_i are coordinates and time of the observation i. x_j, y_j, z_j, t_i are coordinates and time of the observation j.

The signal covariance matrix $\mathbf{C_{ss}}$ and $\mathbf{C_{s's}}$ are computed with the same covariance function (Eq. 6.33) as $\mathbf{C_{yy}}$ but different variance of the signal $\sigma_{sig} = 2.5$ with the unit of K or hPa.

After T, P, and e are interpolated horizontally in the lowest layer, vertical profiles are computed for each grid column by extrapolating the *surface* data vertically:

$$T(z) = T_0 - 0.0064\text{K/m} \cdot z \tag{6.34}$$

$$e = \text{rh} \cdot \text{c} \cdot e^{\frac{a(T(z) - T_c)}{T(z) - b}} \tag{6.35}$$

where e is the partial pressure of water vapor in Pa. The coefficients $T_c = 273.16$ K, $c = 6.1078$, $b = 35.86$, $a = 17.2693882$ are according to Kraus (2006). At last the wet refractivity is computed on each grid node using the Smith and Weintraub (1953) formula:

$$N_w = k_2 \frac{e}{T} + k_3 \frac{e}{T^2}. \tag{6.36}$$

6.3.2 GPS tomography based on a Kalman filter

EPOS provides currently hourly batches of GPS-STDs with a temporal resolution of 2.5 min, which are processed in near real-time. Therefore, every 2.5 min new observations are added to estimate the new state with the Kalman filter. The matrix $\mathbf{F}$, which propagates the state in time, would require the implementation of a physical model for the temporal development of the humidity in the atmosphere (weather model). However, such a complex model cannot be integrated into the Kalman filter and this is not necessary. For a short period like 2.5 min, the water vapor field can

be assumed to remain close to the previous one ($\mathbf{F} = \mathbf{I}$). The increase of the model error, from one cycle to another, is described by $\mathbf{Q}$. $\mathbf{z_k}$ denotes the observation vector with its error covariance $\mathbf{R_k}$. In this implementation, the observation error is derived from the error of the estimated STDs, which is provided by the EPOS. The error correlation, e.g., between observations of the same station or the same satellite, is difficult to quantify. Therefore, the observations are supposed to be uncorrelated and the measurement error covariance matrix is assumed to be diagonal. The error of the observations is derived from GPS slant delay error estimated in section 4.2.1. The estimated error for IWV_z is 1.23 mm and the corresponding error of SWDs is therefore estimated as:

$$\sigma_{SWD} = m_w \frac{\sigma_{IWV_z}}{\Pi} = m_w \frac{1.23}{0.17} = m_w 7.24 \ . \tag{6.37}$$

The wet mapping function is calculated with the input elevation, time and location of each slant. The initial state is constructed with the same method as in the previous section. Only if the estimate is required in a short time after the start of the Kalman filter, the initial state is very important. However, after long time processing, the covariance of the state vector will converge to the true $\mathbf{P}$ no matter of its initial value. Therefore, the solution of Kalman filtering will not be very sensitive to the initial state estimate. For this reason, the variance of the refractivity in $\mathbf{P_0}$ is assumed to be a function of height, which can be modeled by an exponential function in the form of:

$$\sigma_P^2 = \sigma_0^2 e^{-\frac{2h}{h_{sc}}} \tag{6.38}$$

where σ_0 is the error of the ground refractivity and h_{sc} is the scale height. The 1 % of the ground refractivity in the initial field is used as σ_0 and $h_{sc} = 10,000\, m$.

One important parameter is the matrix $\mathbf{Q}$, which describes the uncertainty of the propagation between steps. One main task in this chapter is the design of the covariance matrix used in a specific Kalman filter implementation. A sensibility analysis is carried out in order to determine this parameter. Different methods have been used to estimate $\mathbf{Q}$: Gradinarsky and Jarlemark (2004) determined $\mathbf{Q}$ by the use of wind information from RS data to derive the correlation of states; Perler (2011) predicted the error $\mathbf{Q}$ with empirically estimation using the synoptic data and the numerical weather model COnsortium for Small-scale MOdeling (COSMO) over a period of 2 years with a conventional autocovariance estimation process .

Due to lack of the information (wind and long period RS data), different methods were tested. Finally $\mathbf{Q}$ is assumed to be a diagonal matrix:

$$\sigma_Q^2 = \gamma e^{-\frac{2h}{h_{sc}}} + \sigma_c^2 \tag{6.39}$$

where $\gamma = 0.01$, h_{sc} =4,000 m and $\sigma_c = 0.001$ is a small constant.

Adjustments of the solution for more or less noisy cases could be done by increasing or reducing the constant γ. To prevent too small values of σ_Q at high altitudes, a small constant σ_c is added in the Eq. 6.39. Since the matrix $\mathbf{Q}$ plays an important role in Kalman filter implementation, many tests with different formulas and different scale heights are carried out for the proper extent. Figure 6.2 shows the diagonal elements of the covariance matrices $\mathbf{Q}$ and $\mathbf{P}$ for the resulting tomography

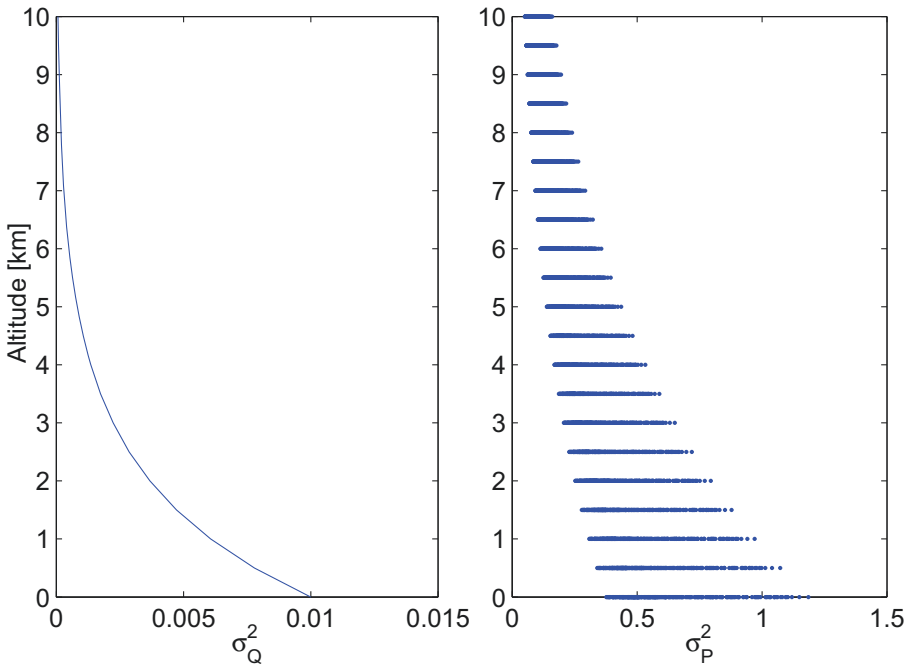

Figure 6.2: σ_Q^2 and σ_P^2 for the Kalman filter for 21 layers at different heights from 0 to 10 km.

at 0 h June 9, 2007 (Fig. 6.6 with the initial state at 12 h June 8, 2007). This σ_Q is for 21 layer of 500 m thickness and 288 batches of 150 s each. To test the tomography result, the 12 h RS observations are used. Different covariance matrices are tested. A good fit of the constructed profiles to the RS observations indicates that the proposed methodology works well.

6.3.3 Comparison of different reconstruction techniques: Kalman filter and MART

The quality of the reconstructed $\mathbf{N_w}$ field can be affected by many factors such as the resolution of the chosen grid, the number, the quality of the input slant data and the method to solve the ill-posed inverse problems. Different methods have different performances and results.

The tomography system developed at GFZ utilizes the MART method. It shows a dependency on the initial field, the iteration number, and the relaxation factor λ. If there are few observations, the results will be similar with the initial field. Figure 6.4 shows example layers reconstructed by the MART tomography. The MART algorithm predicts some pronounced artifacts, which can be caused by the ill-posed inverse problem.

Using the Kalman filter, the error covariance matrix $\mathbf{P_k}$ is computed, which is useful for the quality estimation. The correlation covariance $\mathbf{Q}$ is the most important factor for a successful data inversion. To adjust the correlation of additive observations, the constant γ can be changed. By reducing the value γ close to 0 shows an effect of

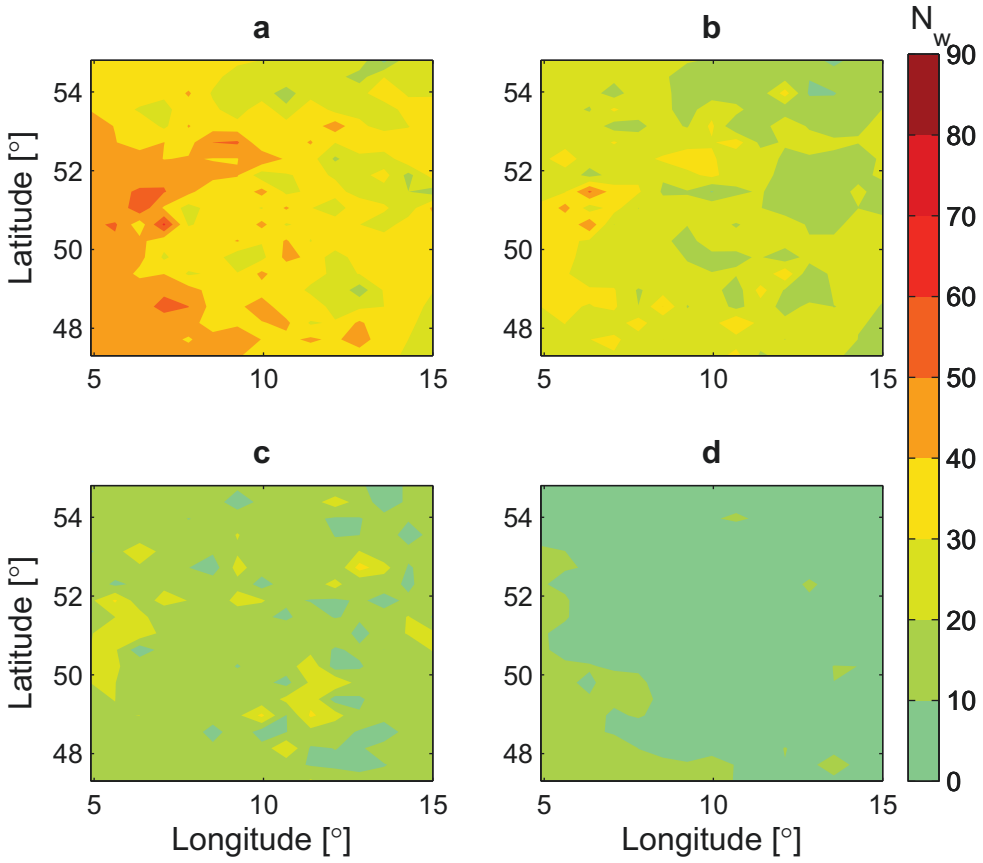

Figure 6.3: MART reconstruction layer of the N_w field at 2,000 m (a), 3,000 m (b), 4,000 m (c), 5,000 m (d).

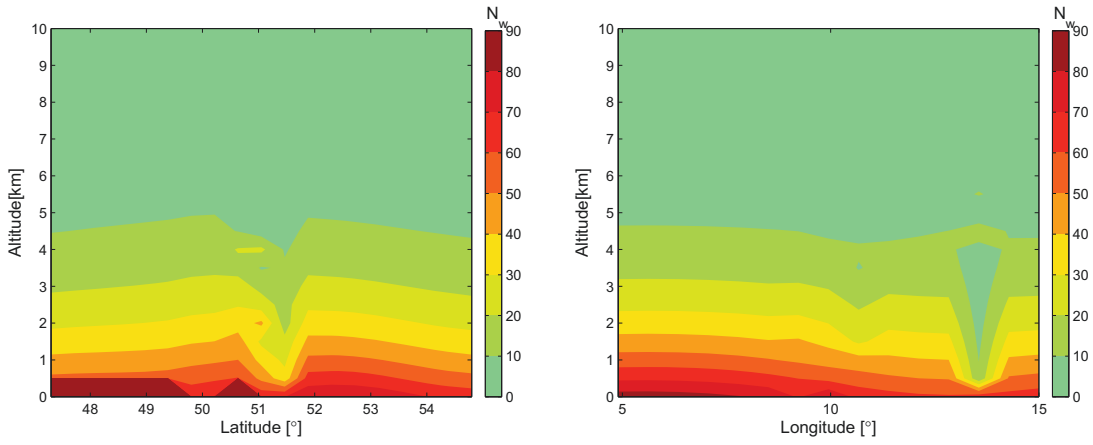

Figure 6.4: MART reconstruction layer of the N_w field at longitude 15° at 0 h June 9 (left); MART reconstruction layer of the N_w field at latitude 54.8° at 0 h June 9 (right).

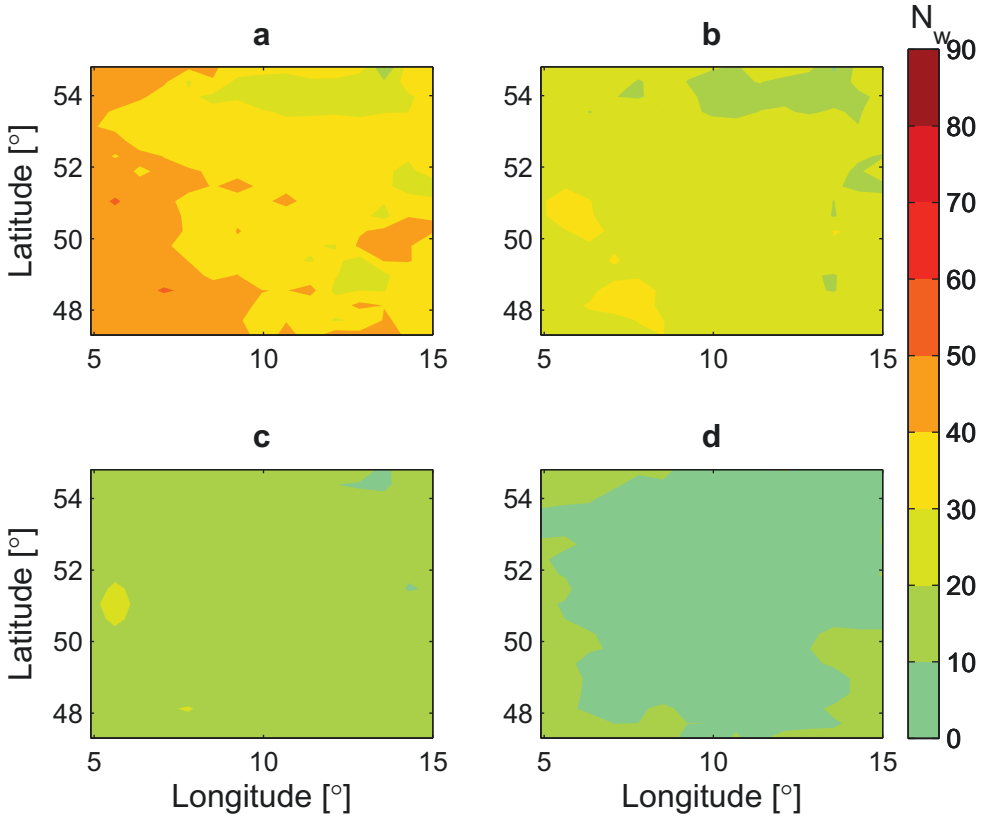

Figure 6.5: Kalman filter reconstruction horizontal layer of the N_w field at 2,000 m (a), 3,000 m (b), 4,000 m (c), 5,000 (d).

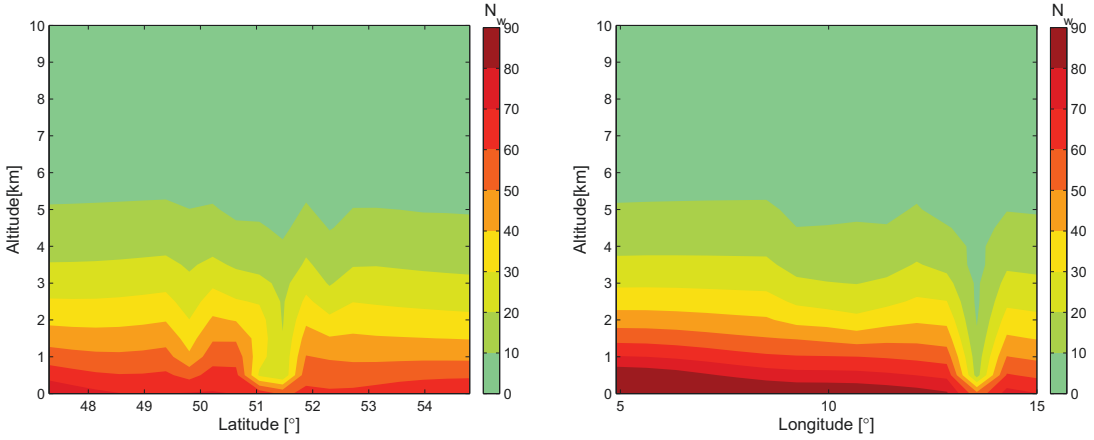

Figure 6.6: Kalman filter reconstruction layer of the N_w field at longitude 15° at 0 h June 9 (left); Kalman filter reconstruction layer of the N_w field at latitude 54.8° at 0 h June 9 (right). (The same time with Fig. 6.4 but with Kalman filter)

smoothing the solution, thus making it more stable. On the other hand, it reduces the capabilities of detection of refractivity changes. Figure 6.5 and 6.6 show layers at the same time with the Fig. 6.3 and 6.4. In contrast to Fig. 6.3 and 6.4, the results in Fig. 6.5 and 6.6 are more smooth between layers. The artifacts present in MART solutions are not visible in the figures based on the Kalman filter method. For further details, the example profiles at 0 h June 9, 2007 according to the method in section 6.4 are generated in Fig. 6.7. The MART and Kalman filter profiles are more similar with each other in contrast to the RS profiles (Fig. 6.7). The RS profiles are more variable due to their high vertical resolution. In comparison with Kalman filter profiles, the MART profiles are more variable, but both show the same tendency of change with RS profiles. It is obvious that the profiles at station Schleswig do not match well in both MART and the Kalman filter. The reason is the low number of observations at this station. It confirms that insufficient observations have an effect on the results, which cannot be improved by different methods.

However, the tomography using the Kalman filter cannot be used for the whole year validation of 2007 because of the following difficulties:

1) Error covariance matrices are roughly estimated. The time correlation between states must be estimated or extracted from long-time series of observations in order to get a more reliable $\mathbf{Q}$. In addition, the error covariance of observations is only estimated from the validation of three months of data with the help of mapping function. More accurate error covariance matrices are required, which can be estimated using long-time data series.

2) The method for the inversion of matrices in the Kalman gain matrix needs to be improved. At the moment it needs 99 hours to reconstruct the tomography from 12 h June 8 to 13 h June 9 (600 iterations). Therefore, it is only a near real-time processing and a more efficient method is required. In addition, the large sparse matrix, which could lead to unstable results, must be taken into account.

6.4 Validation of N_w fields with radiosonde profiles

Because of the above described difficulties and more experience with MART, the MART tomography is used for the validation with the RS data. A set of RS profiles from 13 German RS stations (Fig. 6.1) is available for 2007. The data set with the profiles of the 0 and 12 UTC ascents contains information about the altitude, pressure, temperature, and humidity. In total, 8,109 RS profiles for 2007 are validated with water vapor tomography (Shangguan et al., 2013).

6.4.1 Reconstruction of radiosonde profiles

The wet refractivity profiles of RS can be estimated using the model described in the section 3 (Smith and Weintraub, 1953; Thayer, 1974).

Most of the RS profiles reach up to 20-35 km and for the validation only RS data within the grid used by the tomography are relevant (below 10 km). Most profiles

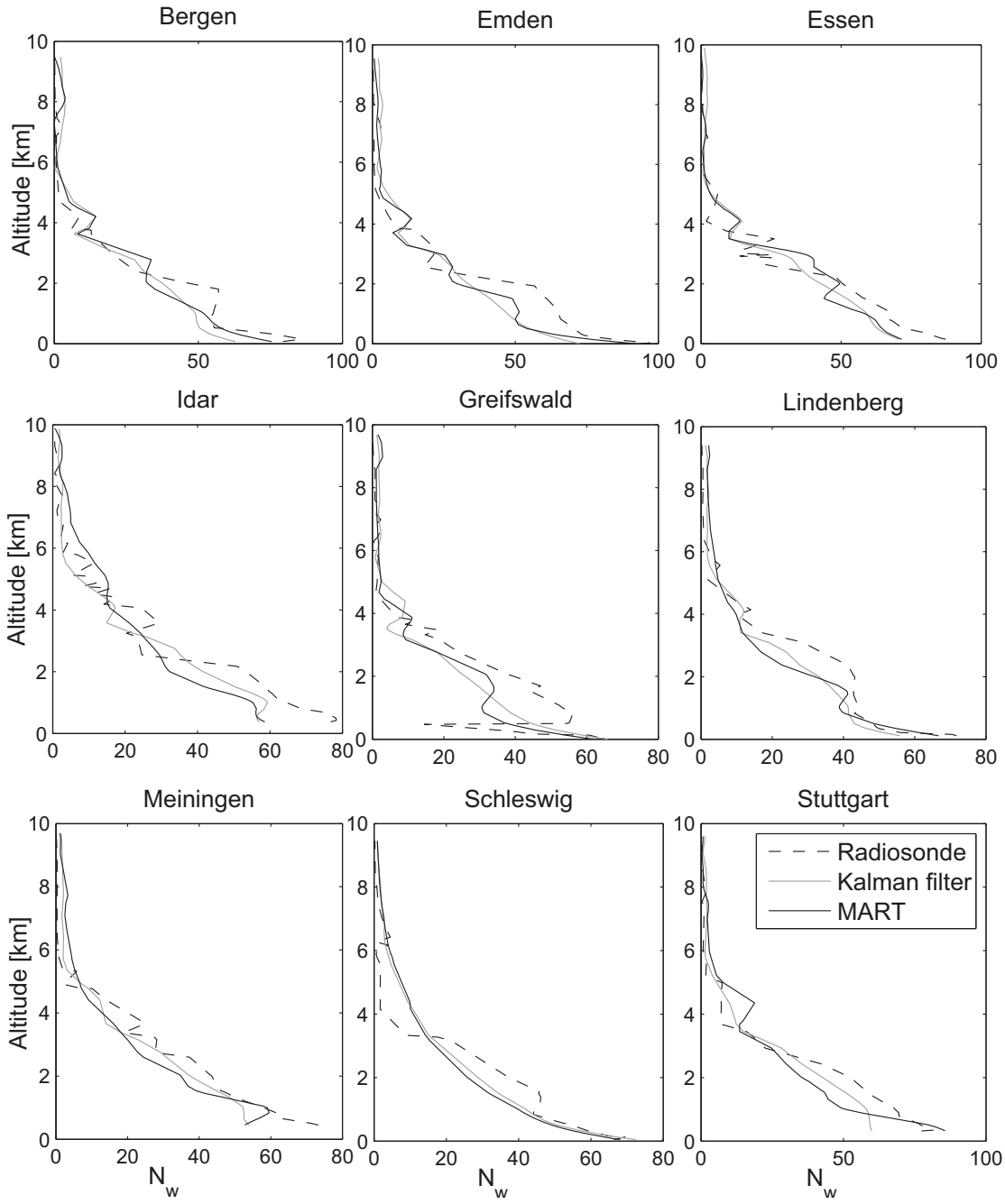

Figure 6.7: Comparison profiles of MART, Kalman filter, and radiosonde at different stations at 0 h June 9, 2007.

consist of 30-50 observations by 10 km, which correspond to a mean vertical distance of the observations between 200 m and 300 m. The vertical distribution is rather variable and many profiles show large gaps. However, not all of them could be used for the validation. 27 RS profiles with no data above 4,000 m are rejected. For the validation, only data within the grid of up to 10 km are used. For the sake of validating the quality of the tomographically reconstructed humidity fields the RS profiles are used as a reference. In addition, the wet refractivity at some start points of the RS profiles is much larger than that at the following points. According to Miloshevich et al. (2009), measurement errors tend to occur in the first 100 m or when the temperature gradient changes abruptly. They are due to the fact that the RS sensor possess different thermal time constants at which the measured air temperature does not accurately represent the temperature from the rh sensor. Hence, if the vertical height difference between the start point and the second point is smaller than 20 m and the wet refractivity difference is larger than 50, then the start point is deleted. Altogether 22 start points are deleted for the whole year. Some RS profiles have two values at the same height and sometimes the height even decreases at some points. For interpolation and integration,the sequence of points with decreasing height is changed and 1 cm is added at the points with the same height.

It should be considered that RS also have their difficulties (Vömel et al., 2007; Miloshevich et al., 2009). The average accuracy of the widely used Vaisala RS92 is about ±4 % for the measured rh value for nighttime soundings and ±5 % for daytime sounding (Miloshevich et al., 2009). Compared to nighttime soundings, there is a solar radiation error in daytime measurements, caused by solar heating of the rh sensor. A time-lag error can be caused by slow sensor response to changing rh conditions at low temperatures (Miloshevich et al., 2004). A comparison between RS humidity observations and GPS-ZWDs can be found in Schneider et al. (2010).

6.4.2 Reconstruction of tomography profiles

The GPS tomography provides $\mathbf{N_w}$ fields on a rather coarse spatial grid and a reconstruction quality, which depends on the geometry of the GPS satellite constellation and many other parameters. These fields have to be compared with a limited number of RS profiles with a high vertical resolution. The quality of the tomographically reconstructed profiles is limited by the low spatial resolution. Moreover, the wet refractivity is assumed to be constant within a voxel. Therefore, the interpolation is applied for the comparison with RS data. Horizontally bilinear interpolation is used with four adjoining grid points whereas vertically cubic spline interpolation is performed (Fig. 6.8) (De Boor, 2001).

Defining criteria for *reliable* columns, which can later be applied, without having reference data is therefore an important task. Another problem is the method to compare a gridded field with the profiles. There are several possibilities, for example, comparing the data point-by-point or regarding whole profiles, therefore, a statistically sound strategy has to be developed.

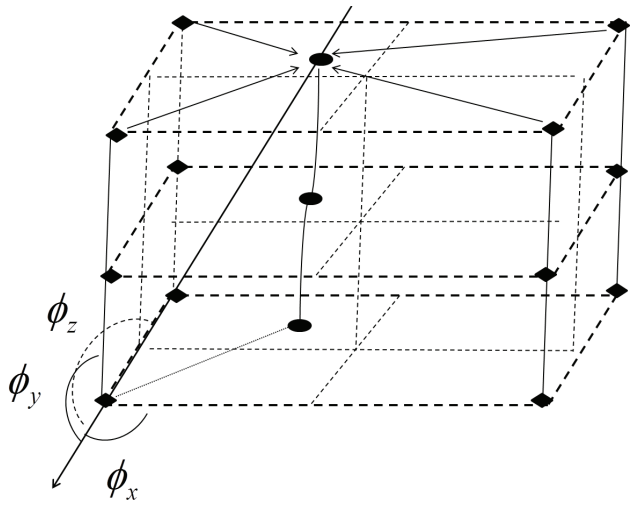

Figure 6.8: Bilinear/spline interpolation: Rhombic points are the center of the voxels and round points are the horizontal locations of RS stations in different layers. In the horizontal the bilinear form with four adjoining points and in the vertical cubic splines are used for the interpolation. ϕ_x, ϕ_y, ϕ_z are the cutting angles between slant path and local axis vectors

6.4.3 Quality estimation of reconstructed profiles

As mentioned above, the MART provides no information about the quality of the result. Therefore, the information of the used slant delays is saved with the wet refractivity for each grid cell. About 25,000 slant delays in 30 min are used to reconstruct the humidity fields, but the distribution of slant paths between the receivers and satellites is always inhomogeneous in space and time, depending on the specific GPS satellite constellation. Consequently, the information available from the observations changes dynamically. Figure 6.9 shows an example of the spatial coverage of the atmosphere with slant paths. It shows that the slant paths are very dense in some areas while in other areas there are almost no slant paths. During COPS a dense GPS network was deployed in the Rhine valley. Therefore, the slants in the Black Forest region in southwestern Germany are very dense in this period (from June to December 2007). On the other hand, there are regions in northern Germany and above the North sea with very few observations. A reliable tomographic reconstruction requires a large number of intersecting slant paths from a wide angular range (Kak and Slaney, 2001) within each grid cell. It can therefore be assumed that cells with no observations or cells with almost parallel slant paths will not be reconstructed very well. As more than 50 % of the cells remain empty and other cells with several GPS stations contain a large number of parallel slant paths (Bender et al., 2009), these criteria can be used to identify regions with insufficient data within the grid.

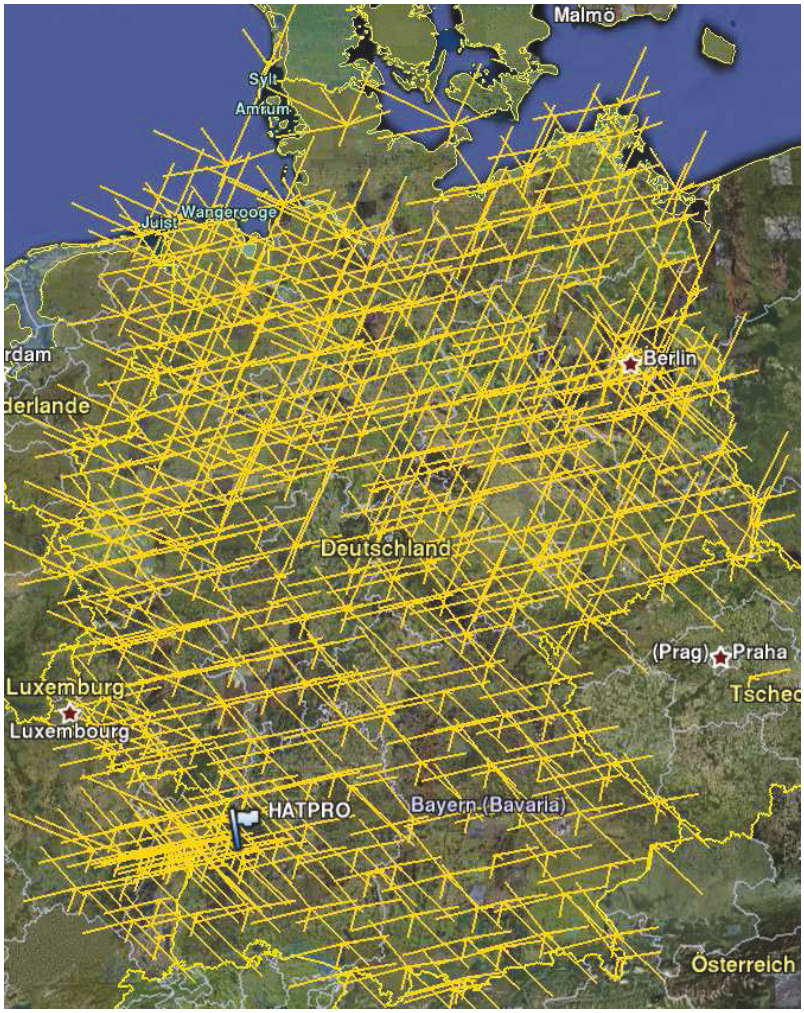

Figure 6.9: Spatial coverage of the atmosphere by GPS slant paths in Germany. The flag shows the location of the COPS investigation area. The sampling rate of STD is 2.5 min.

Density of slant paths

The first step to estimate the quality of the available data is to count the number of slants per grid cell and per column. The number of used delays in every voxel for each column is stored together with the value of wet refractivity in the tomography. In an ideal case, only columns with a large number of evenly distributed slants would be selected, but due to the large number of empty cells, even the columns with one or more empty cells cannot be totally rejected. For comparison with the RS profiles, four neighbored columns are required to interpolate the gridded data on the profile (Fig. 6.8). In an ideal case, the four neighbored columns are fully covered by the observations. However, due to the limited number of stations and satellites the distribution of the observations is very inhomogeneous. In reality, the used interpolated columns may have empty cells.

Figure 6.10 shows a typical situation. The number of slants per voxel within four adjoining columns and at different altitudes can be significantly different. In Fig. 6.10,

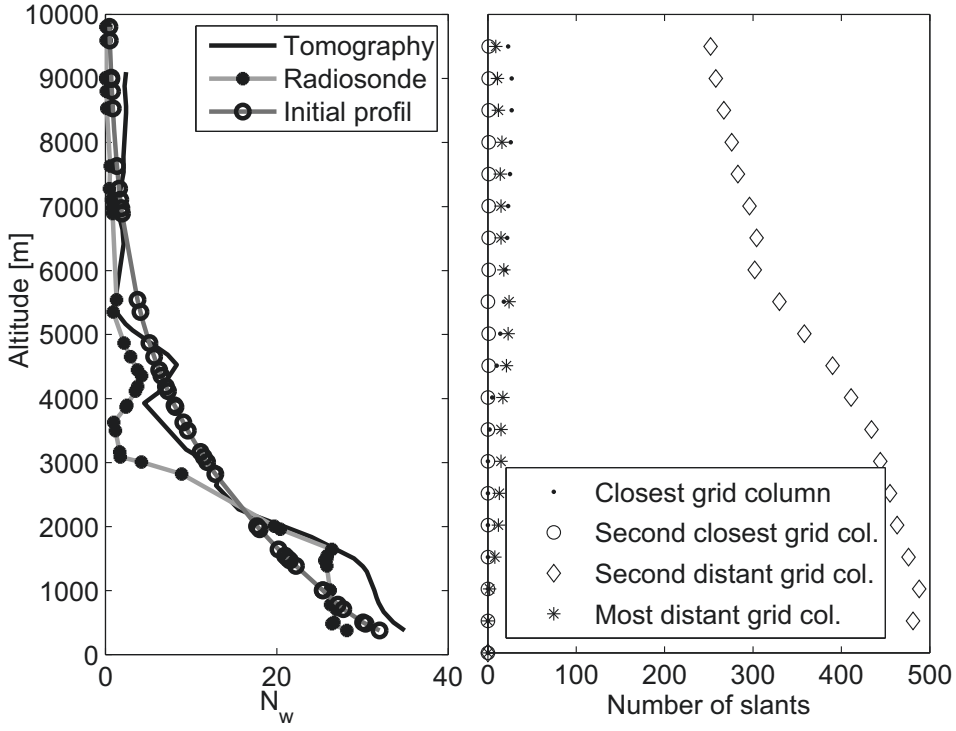

Figure 6.10: Vertical profiles at station Kümmersbruck at 12 h, March 28, 2007(left) and the number of slant paths per voxel in four adjoining columns for interpolation (right).

right, one column is not pierced by any slant path, two columns show a rather small but evenly distributed number of slants which increases slightly with increasing height. This is typical for columns which do not contain any GPS stations but are surrounded by several stations. The last column shows a very high number of slants per cell and contains several stations. The bilinear interpolation of the N_w data from these columns gives the highest weights to the least distant points without considering the number of observations. In Fig. 6.10 the column second closest to the RS profile gets a higher weight than the column with most observations, the interpolated value has a large contribution from the initial field. The reconstructed profile (Fig. 6.10, left) shows segments with a strong impact on the inversion, i.e. the STDs but also the segments which are close to the initial profile. A combination of such contradictory information often leads to strong artifacts in the reconstructed field. Such profiles are rejected for the validation. It is rather difficult to define general criteria for rejecting poor profiles as too restrictive criteria would remove too many profiles, with some of them being relatively good. By varying several parameters, it is decided to reject all sets of four neighboring profiles where the maximum number of slants per cell in one of the four columns is smaller than two. In this case, there are no intersecting slant paths and very often lots of cells without any data. This rather weak requirement already rejects 7 % of the profiles (see Tab. 6.1).

Angular distribution of slant paths

The quality of a tomographic reconstruction depends not only on the number of slant paths, but also on the way these paths are intersecting. Therefore, the crossing angles of any pair of slant paths within each voxel are investigated and discussed next. An almost flat distribution of intersection angles in the range of (0°, 180°) would present an ideal case.

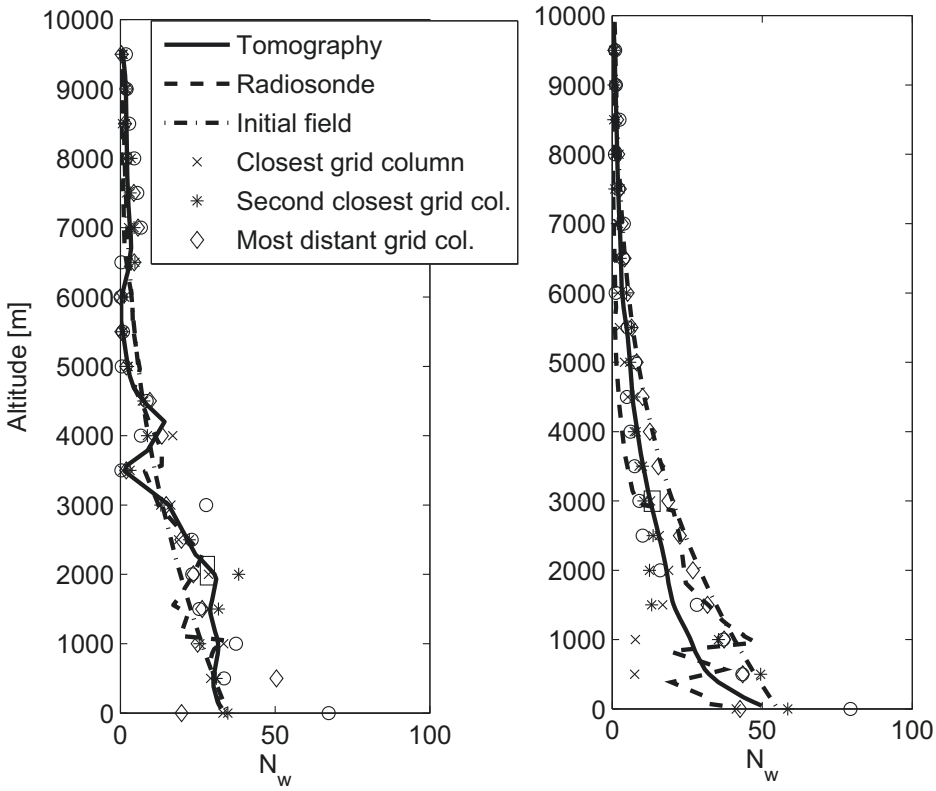

Figure 6.11: Profiles at 12 h, January 31, 2007 of station Bergen (left) and at 12 h June 9, 2007 of Schleswig (right). The grid cells indicated by the black boxes are chosen as examples as these cells are closest to the RS stations.

To investigate a real situation, the intersection angles and their distribution must be computed for each single grid cell. This is done for an example shown in Fig. 6.11. The two profiles are chosen from a region with a rather high density of slant paths and all grid cells contain numerous observations. The RS profiles (dashed line) and the tomographically reconstructed profiles (solid line) are shown together with the N_w data at the surrounding grid points. The humidity profile at Bergen (Fig. 6.11, left) shows rather large deviations from the initial profile but can be reconstructed quite well. In contrast, the humidity profile at Schleswig, which is reconstructed from a comparably large number of STDs does not match the RS profile. Neither the fluctuations in the boundary layer nor the step at 3,000 m is found in the tomography profile. The number of STDs around the RS station is sufficient and it can be assumed that the angular distribution of the slant paths is the reason for the poor

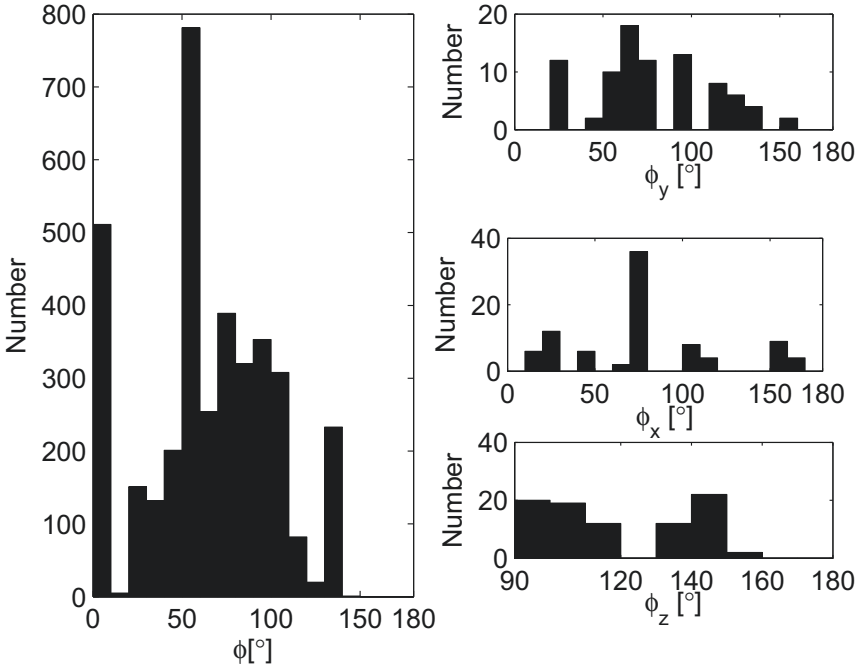

Figure 6.12: Histogram of crossing angles of every two slants in the chosen voxels (see Fig. 6.11 (left)) at station Bergen. The corresponding cutting angles with the axis vectors $\vec{e_x}$, $\vec{e_y}$, $\vec{e_z}$ and a spread of $d\phi_x = 142.75°$, $d\phi_y = 129.37°$, $d\phi_z = 53.81°$ are shown on the right side.

quality of the reconstruction. This aspect is further investigated in more detail. The N_w data indicated by the black box, which from the column closest to the interpolation value is chosen as an example. The histograms of crossing angles of the two selected voxels are shown in Fig. 6.12 (2,000 m) and in Fig. 6.13 (2,500 m) .

The crossing angle ϕ for each pair of slants $\vec{r}_1$ and $\vec{r}_2$ is given by:

$$\phi = \arccos \frac{\langle \vec{r}_1, \vec{r}_2 \rangle}{|\vec{r}1||\vec{r}_2|} \tag{6.40}$$

In case of Bergen (Fig. 6.12, left) a wide distribution of crossing angles ϕ is found, which indicates intersecting slant paths from a wide angular range. On the contrary, the histogram for Schleswig (Fig. 6.13, left) shows a narrow distribution with slant paths pointing in two or three distinct directions. The number of slants in Fig. 6.11 (right) is 80 which is slightly less than 87 in Fig. 6.11 (left) but should be sufficient for a reliable reconstruction. However, in the Schleswig case it is difficult to locate the information provided by the slant delays as all signals propagate almost in the same direction and there are no real intersections between the paths. This leads to a rather poor reconstruction compared to the one for Bergen.

Analyzing distributions as shown in Fig. 6.12 (left) and Fig. 6.13 (left) for each single grid cell would be rather difficult and cannot provide definite information

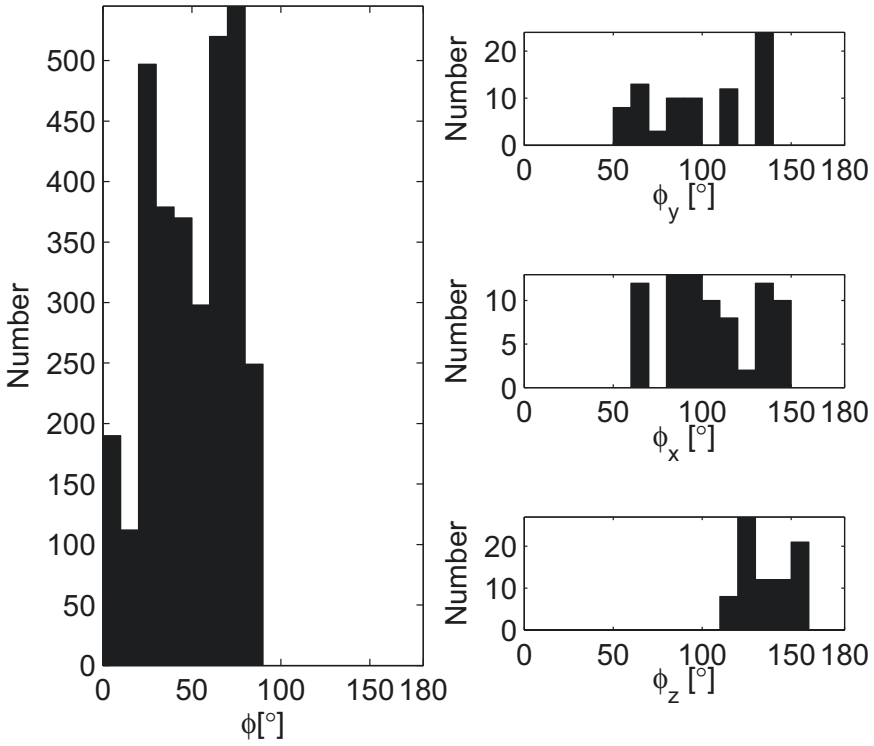

Figure 6.13: Histogram of crossing angles of every two slants in the chosen voxels in Fig. 6.11 (right) at station Schleswig. The corresponding cutting angles with the axis vectors $\vec{e_x}$, $\vec{e_y}$, $\vec{e_z}$ and a spread of $d\phi_x = 82.67°$, $d\phi_y = 88.41°$, $d\phi_z = 45.29°$.

on the reconstruction quality, as the slant path distribution in the entire region has to be considered. A classification number is defined, which is much easier for computation and analysis: For each slant path, the angles to the principal axes of the local Cartesian system are computed, i.e. ϕ_z is the angle to the vertical axis ($90° < \phi_z < 180°$) and ϕ_x and ϕ_y are the angles to the horizontal axes ($0° < \phi_{x,y} < 180°$). The formula for the cutting angle between slant paths and the local axis vector is described by Eq. 6.41 (Fig. 6.8):

$$\phi_i = \arccos \frac{\langle \vec{r}, \vec{e_i} \rangle}{|\vec{r}|} \tag{6.41}$$

where $\vec{r}$ is the slant vector and $\vec{e_i}$ ($i = x, y, z$) are the Cartesian unit vectors.

Figure 6.13 (right) shows the distribution of ϕ_i for Bergen. The number of entries in each histogram is much smaller than in Fig. 6.12 (left), as only one angle is computed for each slant path and each principal axis while in Fig. 6.12 (left) any possible pairs of slant paths are regarded. Again, a wide distribution of angles is found for the station Bergen (Fig. 6.12) while the angles for the station Schleswig are centered at same specific directions (Fig. 6.13). To quantify the width of the distribution, the differences between the maximum and minimum cutting angles are analyzed for

Total number of RS profiles	8109
RS profiles with large gaps	27
No tomographic reconstruction	18
Tomography profiles with too few slants	569
Tomography with poor angular distribution	692
Pairs of profiles for validation	6803

Table 6.1: Number of rejected profiles according to different criteria.

each voxel:

$$d\phi_i = \phi_i^{max} - \phi_i^{min}. \tag{6.42}$$

The angles between the slant paths and the vertical axis are between $90° < \phi_z < 180°$ and $d\phi_z < 90°$. It turns out that $d\phi_z$ is not directly correlated with the reconstruction quality, while large numbers of $d\phi_x$ and $d\phi_y$ usually indicate a wide slant path distribution and a good reconstruction quality. To identify unreliable profiles, the $d\phi_x$ and $d\phi_y$ values of all cells of the four grid columns surrounding the RS station are analyzed. The profile is rejected if the maximum of $d\phi_x$ and $d\phi_y$ are both smaller than 90° in all of the four columns. Another 692 profiles are rejected by this criterion, regarding the profiles passing the criteria defined in the previous section (see Tab. 6.1).

In total 1306 out of the 8109 profiles available are rejected, leaving 6803 profiles for the validation (Tab. 6.1). 27 RS profiles are rejected due to large gaps. For 18 profiles the STD data are not sufficient to start the tomography because no slants are read in the selected time. 569 tomographically reconstructed profiles are excluded from the validation because the number of slant data in the vicinity of the RS station is insufficient and 692 profiles are excluded because the angular coverage is poor.

Most of the rejected profiles (due to an insufficient number of slants) belong to the station Schleswig. As can be seen in Fig. 6.1, there are only few GPS stations around Schleswig and they are located only on the western side.

Certainly not all the profiles selected in this way provide reliable data but due to the necessity to interpolate from the rather coarse tomography grid to the RS station four surrounding columns are required. It must be pointed out that the columns of the reconstructed field, which do not match these criteria, do not necessarily contain poor data. Columns with few observations are dominated by the initial field, which is only modified due to the inter-voxel constraints. If the initial field is chosen well, then the reconstruction will match the real conditions, which leads to a smooth exponential profile. However, this is not the result of the tomographic reconstruction and these data are not considered further.

6.4.4 Comparison of tomography with radiosonde data

After cleaning the available RS profiles and interpolating the reliable parts of the tomographically reconstructed $\mathbf{N_w}$ field on the individual points of the RS profiles,

RS station	a	$\overline{\Delta N_w}$	RMS	$\overline{\Delta N_w^r}$	rms_r
Bergen	28589	-0.343	8.996	-5.024	36.417
Emden	31139	-0.901	7.899	-3.674	16.834
Essen	33363	-0.816	9.149	-3.535	19.310
Fritzlar	8687	-1.124	8.128	-1.384	5.775
Greifswald	31740	-0.75	7.541	-4.156	22.891
Idar	27156	-1.305	8.112	-2.656	11.725
Kümmersbr.	26966	-0.309	6.479	-3.432	15.779
Lindenberg	30107	-1.043	7.633	-3.891	17.417
Meiningen	27509	-0.334	6.713	-2.995	14.198
Meppen	4013	0.031	6.916	-5.542	23.102
München	27166	-0.941	6.476	-3.192	14.523
Stuttgart	33571	-0.673	7.472	-2.917	15.661

Table 6.2: Statistic data of difference between RS and tomography. a is the number of observations. $\overline{\Delta N_w}$, RMS are the average difference of N_w between RS and tomography and its RMS. $\overline{\Delta N_w^r}$, RMS_r are the average and RMS of the relative differences.

two sets of N_w profiles defined on the same points in space are available and can be compared. Many methods can be used for the comparison such as a point-by-point validation or the validation of entire profiles.

Point-by-point validation

In a first step, an attempt is made to compare point-by-point, i.e. the mean differences:

$$\overline{\Delta N_w} = \frac{\sum_{i=1}^{a} N_{w,i}^{GPS} - N_{w,i}^{RS}}{a} \tag{6.43}$$

and their RMS are compared for each station without considering the height or observation time of the data. a is the number of observations. The absolute differences might be misleading for the almost exponential vertical N_w profiles and the corresponding relative differences are also taken into account:

$$\overline{\Delta N_w^r} = \frac{1}{a} \sum_{i=1}^{a} \frac{N_{w,i}^{GPS} - N_{w,i}^{RS}}{N_{w,i}^{RS}}. \tag{6.44}$$

The results for one year data are shown in Tab. 6.2. For each station, the number of observations a is given. There are many observations at different heights from 0 to 10 km and different refractivities between 0 to 100, and as a result that the corresponding differences are quite variable.

The ΔN_w varies from -1.3 to 0.03 and an overall RMS of about 6.5-9 is reached, depending on different RS stations. Most of the $\overline{\Delta N_w^r}$ are positive because of many small RS observations $N_{w,i}^{RS}$ at high altitude as denominator. At high altitude the measured value of RS are always trending to 0 and therefore, the corresponding ΔN_w^r in this region have always large values in spite of small ΔN_w.

These results are rather unspecific and provide little information about the quality of the tomographic reconstruction. It cannot be seen how many profiles show a good representation of the real vertical atmospheric structure.

A better indicator than the mean of all observations is the mean deviation at a certain altitude. For this purpose, the differences of RS and tomography data are classified in 20 vertical layers defined for the tomographic reconstruction and the means as well as their RMS are computed using Eqs. 6.43 and 6.44 for each individual layer. $\overline{\Delta N_w}$ is dominated by deviations in the boundary layer where N_w is large and leads to small relative deviations. $\overline{\Delta N_w^r}$ is dominated by deviations near the tropopause where N_w is small and small deviations can lead to very large relative errors up to several 100 %. The $0 \leq N_w \leq 5$ and the large relative uncertainty of humidity data at higher altitudes do not necessarily correspond to poorly-matched profiles.

Data from three RS stations (Lindenberg, Essen and Meiningen) are chosen as examples. The station Essen represents the most usual case with moderate differences, while the station Lindenberg shows a rather large deviation and the station Meiningen a small deviation. The difference and RMS of the wet refractivity can be found in Tab. 6.2. The result for 20 equidistant layers are shown in Fig. 6.14. It is shown that plots for the different stations follow the same pattern. The bias of different RS stations shows rather large fluctuation in the lower layers. The RMS is rather similar for all stations and decreases with increasing altitude. The relative bias of different RS stations shows large fluctuations in the upper layers. RMS_r increases with the increasing altitude for all stations. Below 2,000 m the mean difference is variable because of an insufficient number of GPS observations in low altitudes. Above 8,000 m the wet refractivity of RS data is rather small and has a large effect on the relative value.

Validation of entire profiles

In a second step, an attempt is made to compare entire profiles and to quantify the degree of consistency between RS and tomography profiles. The visual validation of 6803 individual profiles one by one requires a lot of work. Therefore, defining general criteria which can be checked automatically, is necessary to determine the agreement between RS and tomography profiles in a consistent way. To check if two profiles are almost similar, it is beneficial to compare some integrated quantities, e.g., the ZWD up to the top grid layer:

$$ZWD = \int_0^H N_w dh. \tag{6.45}$$

The ZWD should be similar for both profiles (small difference D):

$$D = |ZWD^{RS} - ZWD^{GPS}| \tag{6.46}$$

It turns out that the absolute differences D of well-matched profiles varies considerably with the weather situation and the relative difference

$$d = D/ZWD^{RS} \tag{6.47}$$

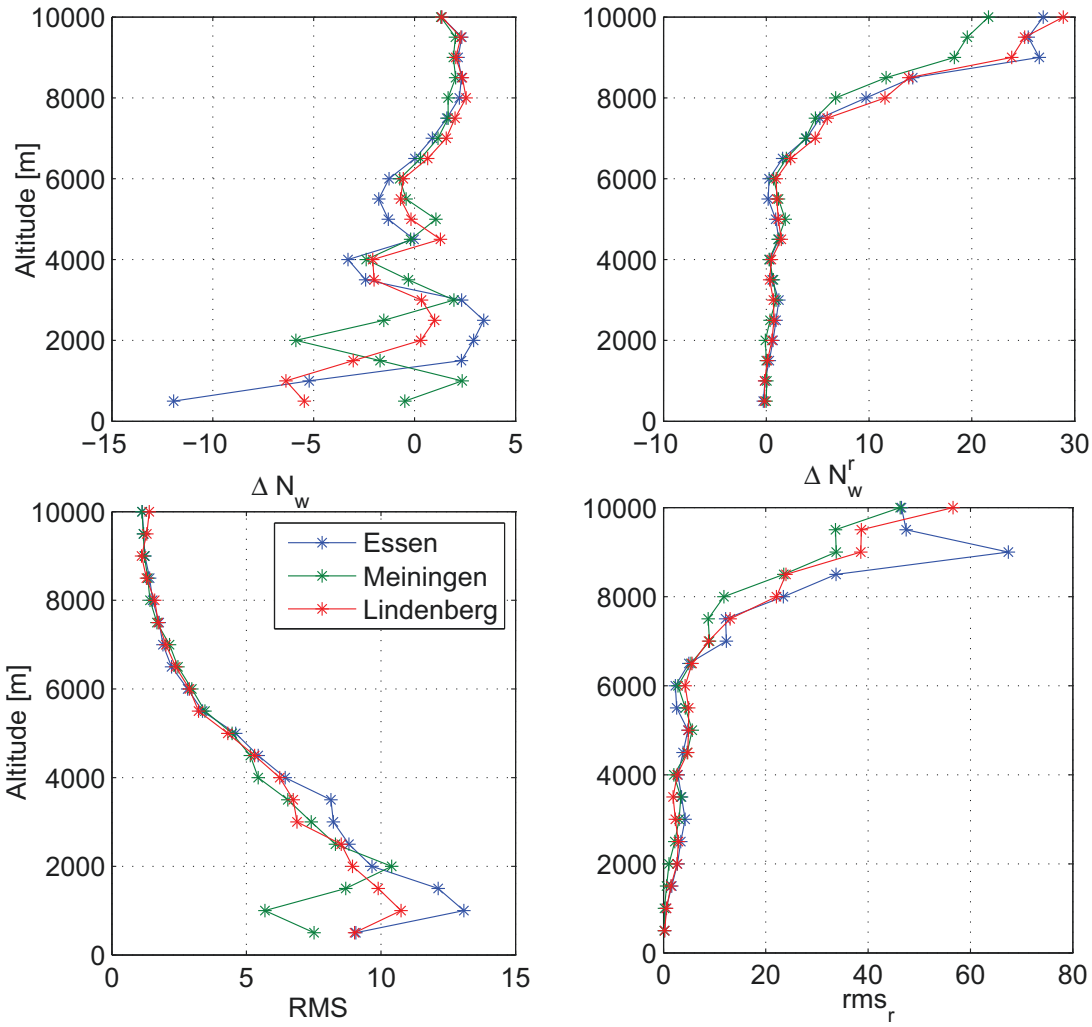

Figure 6.14: Mean difference of ΔN_w and their RMS of all (6803) tomography and RS profiles in 20 levels (left panel); Relative mean differences of ΔN_w^r and their rms_r at the right side.

is used to define more general criteria. However, two completely different profiles can show the same ZWD, i.e. the same area below the function $N_w(h)$ (Fig. 6.15, left) and the area K between the two $N_w(h)$ functions is also considered:

$$K = \int |N_w^{RS} - N_w^{GPS}| dh. \tag{6.48}$$

The refractivity changes considerably with the weather situation and rather small differences on a warm humid summer day can lead to K-quantities much larger than it is found for poorly-matched profiles at a dry and cold winter night. Therefore, the normalized area k is used for comparing the quality in a more general way.

$$k = K/ZWD^{RS}. \tag{6.49}$$

Most profiles look similar if d and k are sufficiently small but there are some profiles with outliers which have a small impact on the integrated quantities d and k,

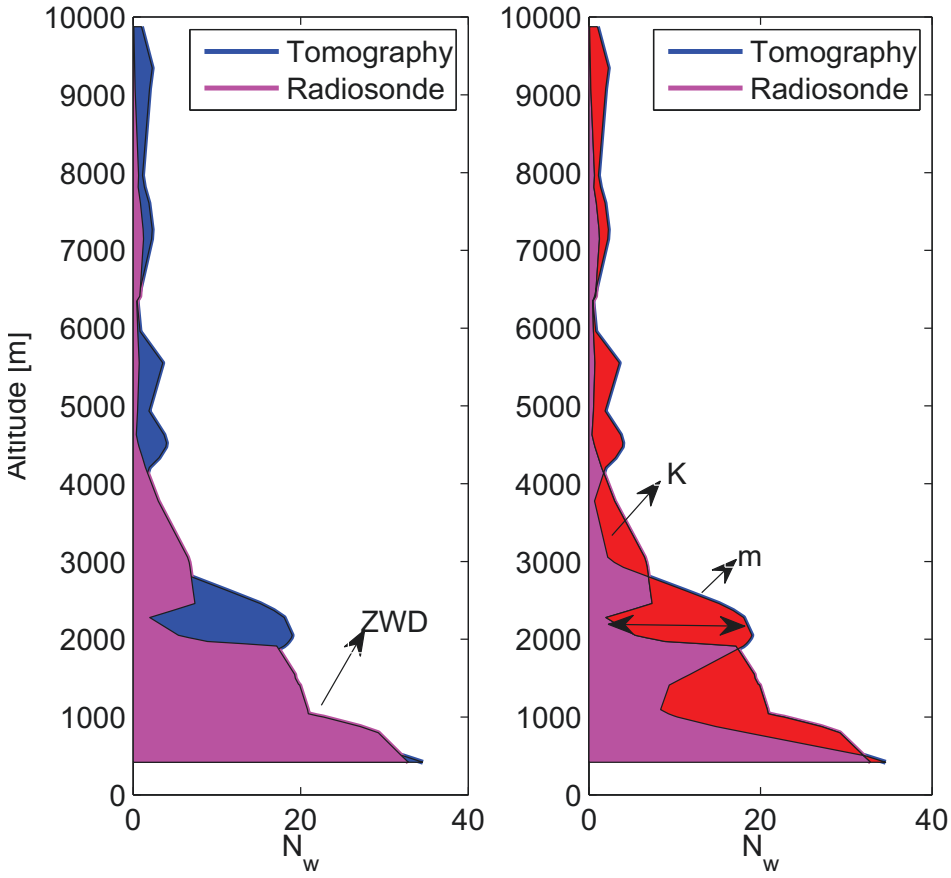

Figure 6.15: Example profiles from the station Kümmersbruck at 12 h January 3, 2007. Used parameters for the validation: m: maximal absolute difference of N_w; ZWD: zenith wet delay (left); D: difference ZWD; K: integral of absolute difference wet refractivity (right).

that need to be rejected. Such outliers can be due to artifacts in the tomographic reconstruction but are also present in the RS data. The maximum differences m is used to identify these outliers:

$$m = \max|N_w^{RS} - N_w^{GPS}|. \tag{6.50}$$

After tries with different values, certain quantities for m, d and k are set by visual inspection. They characterize well-matched profiles and poorly-matched profiles (Tab. 6.3). Profiles belonging to neither group are regarded as indifferent. It turns out that even the relative quantities m, d and k depend to some degree on the atmospheric humidity and different thresholds are defined for different weather situations. More relaxed criteria can be used in case of very humid situations while rather rigid settings are required in dry cases. The ZWD is used to quantify the total amount of atmospheric humidity and four classes with different thresholds for d, k, and m as given in Tab. 6.3 are defined to identify the quality of the tomographically reconstructed profiles. For very dry situations (ZWD <60 mm), it is important to reject outliers (small m) but rather large value of k can be tolerated. With an increasing

ZWD[mm]	Poor m or d or k			Good m and k	
$ZWD <= 60$	$m > 25$	$d > 55\,\%$	$k > 80\,\%$	$m < 15$	$k < 42\,\%$
$60 < ZWD <= 120$	$m > 30$	$d > 38\,\%$	$k > 60\,\%$	$m < 18$	$k < 34\,\%$
$120 < ZWD <= 180$	$m > 31$	$d > 25\,\%$	$k > 40\,\%$	$m < 23$	$k < 30\,\%$
$ZWD > 180$	$m > 32$	$d > 18\,\%$	$k > 30\,\%$	$m < 25$	$k < 28\,\%$

Table 6.3: Criteria for poorly-matched profiles (left) and well-matched profiles (right) between RS and GPS tomography.

Good	Poor	Indifferent
2,139	1,584	3,080
32 %	23 %	45 %

Table 6.4: Division of profiles in three quality classes.

amount of water vapor, the outliers become less important but the normalized area k between the $N_w(h)$ curves must be rather small. A small value of k implies that d is also small and no specific threshold for d needs to be given for the well-matched profiles. However for rejecting poorly-matched profiles d should be specified.

To determine the limit value, a coarse value above or below the mean value is used firstly for the poor and good criteria. Then a sensitive adjustment with smaller and larger values is applied in this work to test the results. The profiles between the set value and the adjustive value are checked individually. The limit value is adjusted until all the poor and good profiles are extracted. Consequently, the values for the criteria are empirically determined and they can be changed according to different situations.

In Fig. 6.16 four characteristic profiles are given together with the corresponding quantities of the ZWD, m, k, and d. Example (a) shows two profiles with almost the same ZWD (small d) and outliers below the threshold for poorly matched profiles but with a large area between the $N_w(h)$ functions ($k = 59.4\,\% > 40\,\%$). The situation in Fig. 6.16 (b) shows one fundamental problem of the GPS tomography: The reconstructed profile is almost identical to the RS profile for altitudes above 1500 m but absolutely off at lower altitudes because of the sparse GPS observations in the boundary layer. The profile is regarded as poorly-matched because $m = 25.93$ is too large. In case (c) the total amount of humidity is wrong and the profile is rejected because $d = 78.14\,\%$ is too large. Figure 6.16 (d) shows a well reconstructed profile.

Results

The results of the validation study are summarized in Tab. 6.4. Considering only the tomographically reconstructed profiles with sufficient slant data (6,803) about 32 % of the profiles match very well and about 23 % do not match at all. For almost half of the profiles (45 %), the classification is rather difficult as they show well-matched parts together with some discrepancies. However, it must be pointed out that there are very few observing systems which provide spatially reconstructed humidity fields

and most humidity observations come with a rather large error. A fraction of 77 % of the profiles with no major discrepancies to the RS profiles and 32 % of well-matched profiles is therefore a good result for the tomography.

There are several reasons for the large number of indifferent profiles which do not match very well with the RS profiles but also show no major discrepancies. One fundamental problem is the different nature of the data: RS take point measurements which represent the atmospheric state only in close vicinity to the RS sensor while the GPS tomography provides voxel means which cover 50x50 km horizontally and several hundred meters vertically. It cannot be expected that both observations are almost identical. Other reasons are the errors of the observation systems. The presented discrepancies can be affected by the quality of RS data and GPS tomography. RS profiles might sometimes provide wrong data and it is difficult to find a statistical representation for these errors. The GPS tomography has to deal with these difficulties. The STD data provided by the GPS processing systems are the result of a rather sophisticated analysis process and the error is difficult to estimate (Deng et al., 2011). These data enter an ill-posed inverse reconstruction technique which potentially amplifies the errors of the input data. Furthermore, the STD data are incomplete and do not cover the whole region which leads to a rather low resolution of the tomographic reconstruction (Bender et al., 2011b). Due to the low vertical resolution and the necessity to interpolate from the spatial grid on the RS profile, it is not possible to resolve details of the RS profile. Especially thin layers of increased or reduced humidity cannot be resolved, as long as their vertical dimensions are below the vertical grid spacing.

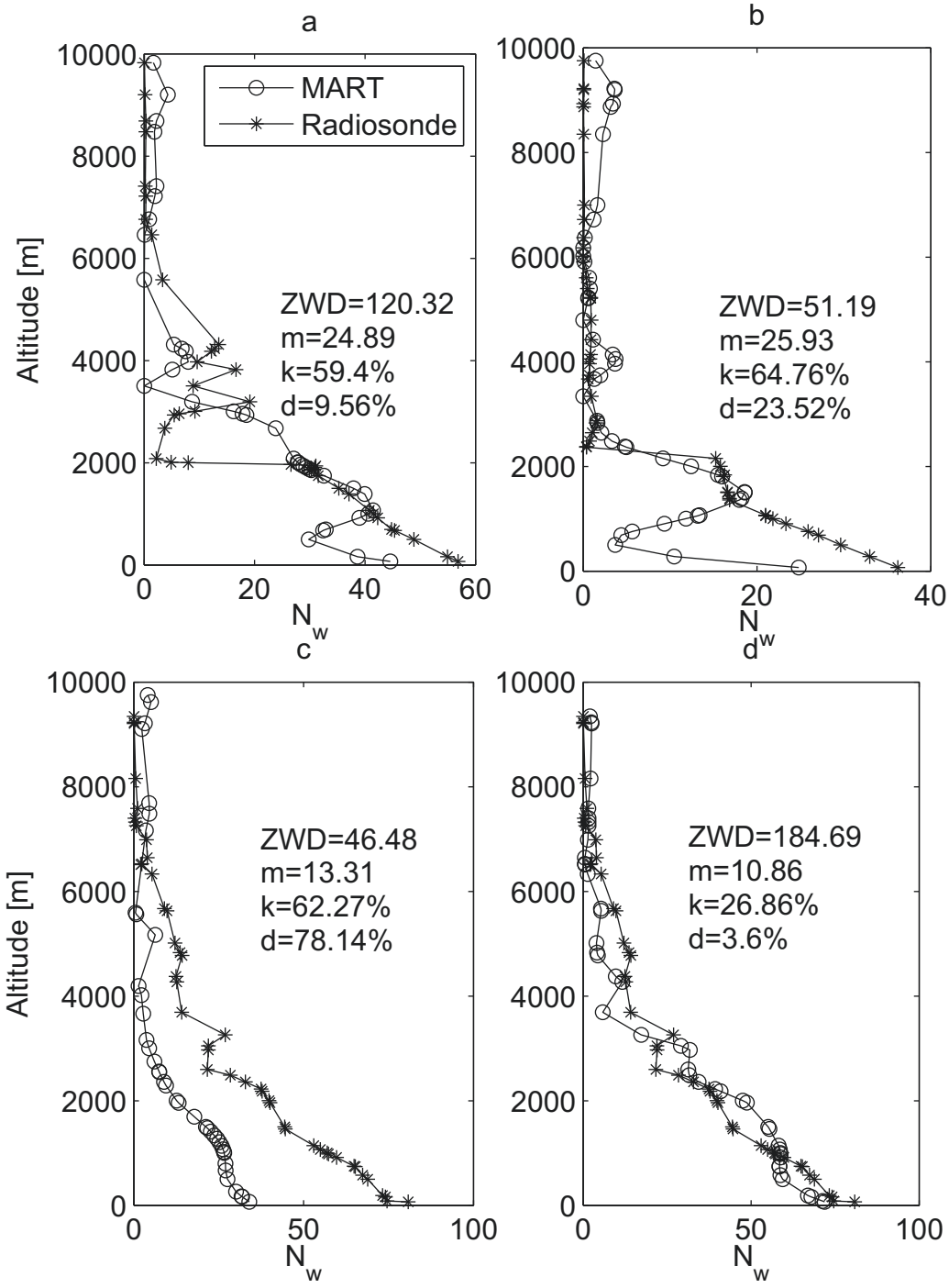

Figure 6.16: Example profiles in different classes, (a) poor with large k, (b) poor with large m,(c) poor with large d, (d) good.

7 Conclusions and outlook

Water vapor in the atmosphere plays an important role in meteorological applications. High accurate water vapor information in space and time can be derived from the observations of a GNSS network. The main objective of this thesis is to analyze and derive the atmospheric water vapor distribution with GNSS data. 3D distribution of the tropospheric water vapor over Germany has been reconstructed. Input data for the water vapor tomography are the GPS tropospheric products from about 300 ground stations.

To reconstruct the water vapor with tomographic techniques, the GPS slant delays from EPOS are used as the input observations. In this thesis, WVR data are used to estimate the accuracy of the GPS-STD. The validation provides evidence for a high agreement between the compared data. The comparison between GPS- and WVR-SIWV at station GFZ0 shows a bias of -0.31 $kg/m^2 \pm 1.89\,kg/m^2$. According to the results, the GPS-STD derived SIWV has a comparable accuracy with WVR data. The estimated accuracy of GPS-SIWV is $\sim 1.79\,kg/m^2$. The analysis indicates that GPS-STDs can reliably resolve atmospheric structures in the research period and are useful as input observations of the water vapor tomography.

However, there are discrepancies between GPS and WVR data on some days. These discrepancies are difficult to be explained by equipment or processing errors. Therefore, the relations between SIWV (GPS - WVR) differences and possible influential factors (meteorological data and elevation) have been tested in this thesis. The differences of SIWV are only relatively dependent on the elevation angles. No clear relations between the differences of SIWV and atmospheric parameters have been found due to the short time frame of the research period. Further studies are planned to verify the relation between influencing factors and the validation results at other months especially in summer. The time series including summer would be collected by the new GFZ-WVR (HATPRO) for the investigation. Furthermore, the effect of GPS data processing and WVR data processing must be also considered because the used parameters in the EPOS or for WVR data also have on an effect on the error of results.

Another important application of the GPS-IWV data is the climatology. Long time series of GPS-IWV data are available at GFZ. A long-term study is applied to the data set. Different statistical methods have been implemented and compared in the study. The biweight mean method is chosen for the trend analysis. Using a linear least squares analysis, the GPS-IWV time series show positive trends at most of stations from 2002 to 2012. Because a new version of EPOS is in operation since 2007, the trends from 2007 to 2012 have been also calculated. In contrast with the trends from 2002 to 2012, the trends from 2007 to 2012 are much more variable. According to these results, the trends are sensitive to the chosen period.

Negative trends are detected in northwestern Germany in summer and more positive trends at most stations in the winter. The strong seasonal trends of IWV on a regional scale underline the necessity of long-term monitoring. However, there are large regional variations and even large opposite trends in different time periods. A

wet or dry year in the beginning or the end of the time period has a strong effect on the results for the short time. With an increasing length of GPS tropospheric data sets, the GPS meteorology will play a more important role in the field of climate research. Differences are shown between the GPS- and ECMWF-data mostly due to the different temporal and spatial resolution of data. In addition, care should be taken to the non-reprocessed GPS data here. There are data gaps at many stations and changes in the GPS estimate such as hardware change and parameter setting by the GPS data processing. With the growth of the time series and progresses in the GRUAN and GNSS4SWEC projects, GPS data will become an independent data source for climate monitoring in the near future.

Within this thesis, a more advanced water vapor tomography system was developed. A new algorithm based on Kalman filter is implemented in the tomography package and tested with the input error covariance matrices (the estimated error covariance of observations, the given initial error covariance matrix of states $\mathbf{P_0}$ and the matrix $\mathbf{Q}$, which describes the uncertainty of the propagation) for several days. The tests demonstrate the good performance of the new algorithm. In comparison with the MART method, the artifacts in the tomography are clearly reduced but it takes a much longer processing time than the MART method. However, the Kalman filter method requires further improvements, namely a better design of the correlation covariance matrix $\mathbf{Q}$, faster method for the inversion of matrices and grid optimization.

To determine the quality of the tomography, the tomography profiles based on MART are validated against the RS data for the whole year 2007. The derived tomography has a spatial resolution of about 50 km horizontally and 500 m vertically up to 10 km altitude. For comparison with the RS profiles, the gridded tomography results are interpolated to the position of RS profiles. Tomographic techniques are limited by errors in the STDs and their poor geometric distribution. The GPS-STD input to the tomography is highly variable in space and time due to the variation of GPS satellite constellation and a uniform quality of the reconstructed fields can therefore not be expected. The distribution of STDs per profiles has been checked before the validation. The number and the configuration of STDs in the individual voxels of tomography is determined. However, four neighbored columns of tomography voxels which are used for interpolation must be taken into account at the same time.

A total of 6,803 profiles, which are considered with sufficient slant data using the described criteria, are validated with different methods. The result of the point-by-point validation between RS profiles and MART tomography shows a mean difference of wet refractivity within -1.3∼0.3 and an overall RMS of about 6.5∼9 compared to RS data, depending on different RS stations. A new developed technique to validate entire profiles is used, which considers the derived parameters for the whole profile. It provides a more reliable conclusion than comparing only point-by-point differences. The validated profiles have been assigned to the well-matched or unmatched group to give an overview of the validation result. The comparison of tomographically reconstructed humidity profiles with RS profiles shows about 32 % of profiles are well-matched. However, there is a non-negligible fraction of profiles with

artifacts, especially in the lower atmosphere and there are regions with insufficient GPS observations. Profiles with large discrepancies are considered as poor agreement profiles (23 %). This result provides a qualitative and quantitative agreement in percent or in profile numbers. This method is helpful to improve reconstruction algorithms by illustrating how well tomography matches the RS data. Different kinds of tomographic algorithms can be tested to get the best agreement.

Apparently, the validation results depend on both the RS and tomographic data. The quality of GPS-SWDs is affected not only by the experimental error but also by several assumptions and approximations made by the GPS data analysis and geometric situation of the STDs. The quality of RS data is mainly affected by sensor errors. In addition, differences in atmospheric conditions sampled at different locations and times should be noted. In particularly, when atmospheric situations change between heavy rain and dry periods, the differences between GPS tomography and RS data are larger. As RS sensors measure the humidity at the instantaneous points, the GPS tomography reconstructs only the average value in one 50x50x0.5 km voxel in 30 min.

The quality of the tomography is mainly limited by the number of observations. It has been shown that many tomography voxels are covered with no or just few GPS-STDs in this study. To get a more dense 3D distribution of GNSS slant observations, the following improvements have to be made:

-Increase the number of GNSS satellites. GLONASS is already fully operational and slant data are basically available. Galileo and Beidou observations will be available within the next years.

-Increase the number of GNSS stations. More and more GNSS stations are available over time. In future, the low cost single frequency receivers will be also used to get a more dense GNSS network.

Using more high quality multi-GNSS slant delays will lead to a considerable improvement of the tomography quality. In parallel, the reconstruction algorithms will be improved and the GPS independent data (WVR, RS) will also be introduced. Then, the water vapor tomography can be further applied in other fields (e.g., nowcasting, severe weather warning, data assimilation).

References

Andersen, A. and Kak, A.: Simultaneous algebraic reconstruction technique (SART): a superior implementation of the ART algorithm, Ultrasonic imaging, 6, 1, 81–94, 1984.

Andrews, D. G.: An introduction to atmospheric physics, ISBN: 9780521693189, Cambridge University Press, 2010.

Barker, V. A.: LAPACK95 users' guide, ISBN-13: 978-0898715040, vol. 13, Society of Industial and Applied Mathematics, 2001.

Bender, M., Dick, G., Wickert, J., Ramatschi, M., Ge, M., Gendt, G., Rothacher, M., Raabe, A., and Tetzlaff, G.: Estimates of the information provided by GPS slant data observed in Germany regarding tomographic applications, J. Geophys. Res., 114, D6, D06 303, doi:10.1029/2008JD011008, 2009.

Bender, M., Dick, G., Ge, M., Deng, Z., Wickert, J., Kahle, H.-G., Raabe, A., and Tetzlaff, G.: Development of a GNSS water vapour tomography system using algebraic reconstruction techniques, Adv. Space Res., 47, 10, 1704–1720, doi:10.1016/j.asr.2010.05.034, 2011a.

Bender, M., Stosius, R., Zus, F., Dick, G., Wickert, J., and Raabe, A.: GNSS water vapour tomography–Expected improvements by combining GPS, GLONASS and Galileo observations, Adv. Space Res., 47, 5, 886–897, doi:10.1016/j.asr.2010.09.011, 2011b.

Bevis, M., Businger, S., Herring, T. A., Rocken, C., Anthes, R. A., and Ware, R. H.: GPS meteorology: Remote sensing of atmospheric water vapor using the Global Positioning System, J. Geophys. Res., 97, D14, 15 787–15 801, doi:10.1029/92JD01517, 1992.

Bevis, M., Businger, S., Chiswell, S., Herring, T. A., Anthes, R. A., Rocken, C., and Ware, R. H.: GPS meteorology: Mapping zenith wet delays onto precipitable water, J. Appl. Meteor., 33, 3, 379–386, doi:10.1175/1520-0450(1994)033<0379:GMMZWD>2.0.CO;2, 1994.

Böhm, J. and Schuh, H.: Vienna mapping functions in VLBI analyses, Geophys. Res. Lett., 31, 1, doi:10.1029/2003GL018984, 2004.

Böhm, J., Niell, A., Tregoning, P., and Schuh, H.: Global Mapping Function (GMF): A new empirical mapping function based on numerical weather model data, Geophys. Res. Lett., 33, 7, L07 304, doi:10.1029/2005GL025546, 2006.

Braun, J., Rocken, C., and Ware, R.: Validation of line-of-sight water vapor measurements with GPS, Radio Sci., 36, 3, 459–472, doi:10.1029/2000RS002353, 2001.

Braun, J., Rocken, C., and Liljegren, J.: Comparisons of line-of-sight water vapor observations using the global positioning system and a pointing microwave radiometer, J. Atmos. Oceanic. Technol., 20, 5, 606–612, doi:10.1175/1520-0426(2003)20<606:COLOSW>2.0.CO;2, 2003.

Calais, E., Han, J., DeMets, C., and Nocquet, J.: Deformation of the North American plate interior from a decade of continuous GPS measurements, J. Geophys. Res., 111, B6, doi:10.1029/2005JB004253, 2006.

Champollion, C., Masson, F., Bouin, M.-N., Walpersdorf, A., Doerflinger, E., Bock, O., and Van Baelen, J.: GPS water vapour tomography: preliminary results from the ESCOMPTE field experiment, Atmos. Res., 74, 1, 253–274, doi:10.1016/j.atmosres.2004.04.003, 2005.

Crewell, S. and Löhnert, U.: Accuracy of boundary layer temperature profiles retrieved with multifrequency multiangle microwave radiometry, IEEE Trans. Geosci. Remote Sens., 45, 7, 2195–2201, doi:10.1109/TGRS.2006.888434, 2007.

Dach, R., Hugentobler, U., Fridez, P., and Meindl, M.: Bernese GPS software version 5.0, Astronomical Institute, University of Bern, 640, 2007.

Davis, J., Herring, T., Shapiro, I., Rogers, A., and Elgered, G.: Geodesy by radio interferometry: Effects of atmospheric modeling errors on estimates of baseline length, Radio Sci., 20, 6, 1593–1607, doi:10.1029/RS020i006p01593, 1985.

De Boor, C.: A Practical Guide to Splines, ISBN: 9780387953663, vol. 27 of *Applied Mathematical Sciences*, Springer, 2001.

Deng, Z., Bender, M., Zus, F., Ge, M., Dick, G., Ramatschi, M., Wickert, J., Löhnert, U., and Schön, S.: Validation of tropospheric slant path delays derived from single and dual frequency GPS receivers, Radio Sci., 46, 6, doi:10.1029/2011RS004687, 2011.

Deng, Z., Bender, M., Zus, F., Ge, M., Dick, G., Wickert, J., and Schön, S.: GPS Meteorology with Single Frequency Receivers, Ph.D. thesis, Fachrichtung Geodäsie und Geoinformatik, Univ. Hannover, 2012.

Emardson, T. R., Elgered, G., and Johansson, J. M.: Three months of continuous monitoring of atmospheric water vapor with a network of Global Positioning System receivers, J. Geophys. Res., 103, D2, 1807–1820, doi:10.1029/97JD03015, 1998.

Emardson, T. R., Johansson, J., and Elgered, G.: The systematic behavior of water vapor estimates using four years of GPS observations, IEEE Trans. Geosci. Remote Sens., 38, 1, 324–329, doi:10.1109/36.823927, 2000.

Ferro, C. A., Hannachi, A., and Stephenson, D. B.: Simple nonparametric techniques for exploring changing probability distributions of weather, J. Climate, 18, 4344–4354, 2005.

Flores, A., De Arellano, J.-G., Gradinarsky, L. P., and Rius, A.: Tomography of the lower troposphere using a small dense network of GPS receivers, IEEE Trans. Geosci. Remote Sens., 39, 2, 439–447, doi:10.1109/36.905252, 2001.

Gaffen, D. J. and Ross, R. J.: Climatology and trends of US surface humidity and temperature, J. Climate, 12, 811–828, 1999.

Garand, L., Grassotti, C., Hallé, J., and Klein, G. L.: On differences in radiosonde humidity-reporting practices and their implications for numerical weather prediction and remote sensing, Bull. Am. Meteorol. Soc., 73, 1417–1424, doi: 10.1175/1520-0477(1992)073<1417:ODIRHR>2.0.CO;2, 1992.

Ge, M., Gendt, G., Dick, G., Zhang, F., and Rothacher, M.: A new data processing strategy for huge GNSS global networks, J. Geod., 80, 199–203, 2006.

Gelb, A.: Applied optimal estimation, ISBN-10: 0262570483, The MIT press, 1974.

Gendt, G., Dick, G., and Soehne, W.: GFZ Analysis Center of IGS. Annual Report 1998, International GPS Service for Geodynamics, pp. 79–87, 1998.

Gendt, G., Dick, G., Reigber, C., Tomassini, M., Liu, Y., and Ramatschi, M.: Near real time GPS water vapor monitoring for numerical weather prediction in Germany, J. Meteorol. Soc. Japan, 82, 1B, 361–370, 2004.

Gilbert, P.: Iterative methods for the three-dimensional reconstruction of an object from projections, Journal of Theoretical Biology, 36, 1, 105–117, 1972.

Gordon, R., Bender, R., and Herman, G. T.: Algebraic reconstruction techniques (ART) for three-dimensional electron microscopy and X-ray photography, Journal of Theoretical Biology, 29, 3, 471–481, 1970.

Gradinarsky, L., Johansson, J., Bouma, H., Scherneck, H.-G., and Elgered, G.: Climate monitoring using GPS, Physics and Chemistry of the Earth, Parts A/B/C, 27, 4, 335–340, doi:10.1016/S1474-7065(02)00009-8, 2002.

Gradinarsky, L. P. and Jarlemark, P.: Ground-based GPS tomography of water vapor: Analysis of simulated and real data, J. Meteorol. Soc. Japan, 82, 1B, 551–560, 2004.

Haines, E.: Point in polygon strategies, Graphics gems IV, pp. 24–46, 1994.

Hammond, W. C. and Thatcher, W.: Northwest Basin and Range tectonic deformation observed with the Global Positioning System, 1999–2003, J. Geophys. Res., 110, B10, B10 405, doi:10.1029/2005JB003678, 2005.

Han, Y., Snider, J., Westwater, E., Melfi, S., and Ferrare, R.: Observations of water vapor by ground-based microwave radiometers and Raman lidar, J. Geophys. Res., 99, D9, 18 695–18 702, doi:10.1029/94JD01487, 1994.

Hansen, P. C.: Analysis of discrete ill-posed problems by means of the L-curve, Society of Industial and Applied Mathematics Review, 34, 4, 561–580, doi:10.1137/1034115, 1992.

Heinkelmann, R., Schmidt, M., Böhm, J., and Schuh, H.: Determination of water vapor trends from VLBI observations, Österreichische Zeitschrift für Vermessung & Geoinformation vgi, 2, 73–79, 2007.

Heise, S., Bender, M., Dick, G., Wickert, J., and Zus, F.: GPS atmosphere sounding: Validation of GPS integrated water vapour with microwave radiometer measurements, in: EGU General Assembly Conference Abstracts, vol. 15, p. 5452, 2013.

Herring, T., King, R., and McClusky, S.: Documentation for the GAMIT GPS analysis software, version 10.3, MIT, Cambridge, 2010.

Hirahara, K.: Local GPS tropospheric tomography, Earth Planets Space, 52, 11, 935–939, 2000.

Hirter, H. A.: Mehrdimensionale Interpolation von meteorologischen Feldern zur Berechnung der Brechungsbedingungen in der Geodäsie, Ph.D. thesis, ETH Zürich, Nr. 11578, 1996.

Hobiger, T., Kondo, T., and Koyama, Y.: Constrained simultaneous algebraic reconstruction technique (C-SART)–a new and simple algorithm applied to ionospheric tomography, Earth Planets and Space, 60, 7, 727, 2008.

Hofmann-Wellenhof, B., Lichtenegger, H., and Wasle, E.: GNSS: Global Navigation Satellite Systems: GPS, GlONASS, Galileo, and More, ISBN-10: 3211730125, Springer, Wien, 2008.

Hopfield, H.: Two-quartic tropospheric refractivity profile for correcting satellite data, J. Geophys. Res., 74, 18, 4487–4499, doi:10.1029/JC074i018p04487, 1969.

Janes, H., Langley, R., and Newby, S.: Analysis of tropospheric delay prediction models: comparisons with ray-tracing and implications for GPS relative positioning, Bulletin géodésique, 65, 3, 151–161, doi:10.1007/BF00806344, 1991.

Jin, S. and Luo, O.: Variability and climatology of PWV from global 13-year GPS observations, IEEE Trans. Geosci. Remote Sens., 47, 7, 1918–1924, doi:10.1109/TGRS.2008.2010401, 2009.

Jin, S., Park, J.-U., Cho, J.-H., and Park, P.-H.: Seasonal variability of GPS-derived zenith tropospheric delay (1994–2006) and climate implications, J. Geophys. Res., 112, D9, doi:10.1029/2006JD007772, 2007.

Jin, S., Luo, O., and Park, P.: GPS observations of the ionospheric F2-layer behavior during the 20th November 2003 geomagnetic storm over South Korea, J. Geod., 82, 12, 883–892, 2008.

Jin, S., Luo, O., and Ren, C.: Effects of physical correlations on long-distance GPS positioning and zenith tropospheric delay estimates, Adv. Space Res., 46, 190–195, 2010.

Kak, A. C. and Slaney, M.: Principles of computerized tomographic imaging, ISBN-13: 978-0898714944, Society of Industial and Applied Mathematics, USA, 2001.

Kalman, R. E. et al.: A new approach to linear filtering and prediction problems, Journal of basic Engineering, 82, 1, 35–45, 1960.

Kalnay, E.: Atmospheric modeling, data assimilation, and predictability, ISBN: 9780521796293, Cambridge University Press, 2003.

Karabatić, A., Weber, R., and Haiden, T.: Near real-time estimation of tropospheric water vapour content from ground based GNSS data and its potential contribution to weather now-casting in Austria, Adv. Space Res., 47, 1691–1703, 2011.

Kneifel, S., Crewell, S., Löhnert, U., and Schween, J.: Investigating water vapor variability by ground-based microwave radiometry: Evaluation using airborne observations, IEEE Trans. Geosci. Remote Sens., 6, 1, 157–161, doi: 10.1109/LGRS.2008.2007659, 2009.

Koch, K.-R. and Kusche, J.: Regularization of geopotential determination from satellite data by variance components, J. Geod., 76, 5, 259–268, 2002.

Köpken, C.: Validation of integrated water vapor from numerical models using ground-based GPS, SSM/I, and water vapor radiometer measurements, J. Appl. Meteor., 40, 4, 1105–1117, doi:10.1175/1520-0450(2001)040<1105:VOIWVF>2.0.CO;2, 2001.

Kraus, H.: Die Atmosphäre der Erde: Eine Einführung in die Meteorologie, ISBN: 3540350179, Springer DE, 2006.

Lanzante, J. R.: Resistant, Robust and Non-Parametric Techniques for the Analysis of Climate Data: Theory and Examples, Including Applications to Historical Radiosonde Station Data, Int. J. Climatol., 16, 1197–1226, doi:10.1002/(SICI)1097-0088(199611)16:11<1197::AID-JOC89>3.0.CO;2-L, 1996.

Leick, A.: GPS satellite surveying, Wiley. com, 2004.

Lutz, S., Troller, M., Perler, D., Geiger, A., and Kahle, H.-G.: Better weather prediction using GPS, GPS World, 21(7), 40–47, 2010.

MacDonald, A. E., Xie, Y., and Ware, R. H.: Diagnosis of three-dimensional water vapor using a GPS network, Mon. Wea. Rev., 130, 2, 386–397, doi: 10.1175/1520-0493(2002)130<0386:DOTDWV>2.0.CO;2, 2002.

Martin, L., Matzler, C., Hewison, T. J., and Ruffieux, D.: Intercomparison of integrated water vapour measurements, Meteorologische Zeitschrift, 15, 1, 57–64, doi:10.1127/0941-2948/2006/0098, 2006.

Mendes, V. d. B.: Modeling the neutral-atmosphere propagation delay in radiometric space techniques, Ph.D. thesis, The University of New Brunswick, Canada, 1998.

Miloshevich, L. M., Paukkunen, A., Vömel, H., and Oltmans, S. J.: Development and validation of a time-lag correction for Vaisala radiosonde humidity measurements, J. Atmos. Oceanic. Technol., 21, 9, 1305–1327, doi:10.1175/1520-0426(2004)021<1305:DAVOAT>2.0.CO;2, 2004.

Miloshevich, L. M., Vömel, H., Whiteman, D. N., and Leblanc, T.: Accuracy assessment and correction of Vaisala RS92 radiosonde water vapor measurements, J. Geophys. Res., 114, D11, D11 305, doi:10.1029/2008JD011565, 2009.

Moritz, H.: Least-squares collocation, Reviews of Geophysics, 16, 3, 421–430, 1978.

Morland, J. and Mätzler, C.: Spatial interpolation of GPS integrated water vapour measurements made in the Swiss Alps, Met. Apps, 14, 1, 15–26, doi:10.1002/met.2, 2007.

Müller: Analyse der zeitlichen und räumlichen Variation der Wasserdampfverteilung in Deutschland, Bachelorarbeit von Hochschule Neubrandenburg, doi:urn:nbn:de:gbv:519-thesis2011-0533-6, 2011.

Niell, A.: Global mapping functions for the atmosphere delay at radio wavelengths, J. Geophys. Res., 101, B1, 3227–3246, doi:10.1029/95JB03048, 1996.

Niell, A., Coster, A., Solheim, F., Mendes, V., Toor, P., Langley, R., and Upham, C.: Comparison of measurements of atmospheric wet delay by radiosonde, water vapor radiometer, GPS, and VLBI, J. Atmos. Oceanic. Technol., 18, 6, 830–850, doi:10.1175/1520-0426(2001)018<0830:COMOAW>2.0.CO;2, 2001.

Nilsson, T. and Elgered, G.: Long-term trends in the atmospheric water vapor content estimated from ground-based GPS data, J. Geophys. Res., 113, D19, D19 101, doi:10.1029/2008JD010110, 2008.

Noguchi, W., Yoshihara, T., Tsuda, T., and Hirahara, K.: Time-height distribution of water vapor derived by moving cell tomography during Tsukuba GPS campaigns, J. Meteorol. Soc. Japan, 82, 1B, 561–568, 2004.

Pacione, R., Sciarretta, C., Faccani, C., Ferretti, R., and Vespe, F.: GPS PW assimilation into MM5 with the nudging technique, Phys. Chem. Earth., 26, 6, 481–485, doi:10.1016/S1464-1895(01)00088-6, 2001.

Perler, D.: Water vapor tomography using global navigation satellite systems, Ph.D. thesis, ETH Zürich, Nr. 20012, 2011.

Pielke, R.: Mesoscale Meteorological Modeling, ISBN: 9780125547666, International geophysics series, Academic Press, 2002.

Rocken, C., Ware, R., Van Hove, T., Solheim, F., Alber, C., Johnson, J., Bevis, M., and Businger, S.: Sensing atmospheric water vapor with the Global Positioning System, Geophys. Res. Lett., 20, 23, 2631–2634, doi:10.1029/93GL02935, 1993.

Rocken, C., Johnson, J., Van Hove, T., and Iwabuchi, T.: Atmospheric water vapor and geoid measurements in the open ocean with GPS, Geophys. Res. Lett., 32, 12, L12 813, doi:10.1029/2005GL022573, 2005.

Rose, T., Crewell, S., Löhnert, U., and Simmer, C.: A network suitable microwave radiometer for operational monitoring of the cloudy atmosphere, Atmos. Res., 75, 3, 183–200, doi:10.1016/j.atmosres.2004.12.005, 2005.

Saastamoinen, J.: Atmospheric correction for the troposphere and stratosphere in radio ranging satellites, The use of artificial satellites for geodesy, Geophys. Monogr. Ser., 15, 247–251, doi:10.1029/GM015p0247, 1972.

Scargle, J. D.: Studies in astronomical time series analysis. II-Statistical aspects of spectral analysis of unevenly spaced data, The Astrophysical Journal, 263, 835–853, 1982.

Schmidt, T., Wickert, J., and Haser, A.: Variability of the upper troposphere and lower stratosphere observed with GPS radio occultation bending angles and temperatures, Adv. Space Res., 46, 150–161, 2010.

Schneider, M., Romero, P., Hase, F., Blumenstock, T., Cuevas, E., and Ramos, R.: Continuous quality assessment of atmospheric water vapour measurement techniques: FTIR, Cimel, MFRSR, GPS, and Vaisala RS92, Atmos. Meas. Tech., 3, 2, 323–338, doi:10.5194/amt-3-323-2010, 2010.

Schuh, H. and Böhm, J.: Very long baseline interferometry for geodesy and astrometry, in: Sciences of Geodesy-II, pp. 339–376, Springer, 2013.

Schüler, T.: On ground-based GPS tropospheric delay estimation, Ph.D. thesis, University of Bundeswehr Muenchen, 2001.

Schwintzer, P.: Sensitivity analysis in least squares gravity modelling by means of redundancy decomposition of stochastic prior information, Deutsches Geodatisches Forschungsinstitut, 1990.

Seeber, G.: Satellite geodesy: foundations, methods, and applications, ISBN-10: 3110175495, Walter de Gruyter, 2003.

Seidel, D. J.: Water vapor: distribution and trends, Encyclopedia of Global Environmental Change, John Wiley & Sons, Ltd, Chichester, 2002.

Shangguan, M., Bender, M., Ramatschi, M., Dick, G., Wickert, J., Raabe, A., and Galas, R.: GPS tomography: validation of reconstructed 3-D humidity fields with radiosonde profiles, Annales Geophysicae, 31, 1491–1505, doi:10.5194/angeo-31-1491-2013, URL `www.ann-geophys.net/31/1491/2013/`, 2013.

Smith, E. K. and Weintraub, S.: The constants in the equation for atmospheric refractive index at radio frequencies, Proceedings of the IRE, 41, 8, 1035–1037, doi:10.1109/JRPROC.1953.274297, 1953.

Solheim, F. S., Vivekanandan, J., Ware, R. H., and Rocken, C.: Propagation delays induced in GPS signals by dry air, water vapor, hydrometeors, and other particulates, J. Geophys. Res., 104, D8, 9663–9670, doi:10.1029/1999JD900095, 1999.

Steigenberger, P., Tesmer, V., Krügel, M., Thaller, D., Schmid, R., Vey, S., and Rothacher, M.: Comparisons of homogeneously reprocessed GPS and VLBI long time-series of troposphere zenith delays and gradients, J. Geod., 81, 6-8, 503–514, doi:10.1007/s001990-006-0114-0, 2007.

Stolle, C., Schlüter, S., Heise, S., Jacobi, C., Jakowski, N., and Raabe, A.: A GPS based three-dimensional ionospheric imaging tool: Process and assessment, Adv. Space Res., 38, 11, 2313–2317, 2006.

Strikwerda, J.: Finite difference schemes and partial differential equations, ISBN: 9780898715675, Society for Industrial and Applied Mathematics, 2007.

Stull, R. B.: Meteorology for scientists and engineers: a technical companion book with Ahrens' Meteorology Today, ISBN 13: 9780534372149, Brooks/Cole, 2000.

Subbarao, P., Munshi, P., and Muralidhar, K.: Performance evaluation of iterative tomographic algorithms applied to reconstruction of a three-dimensional temperature field, Numerical Heat Transfer, 31, 3, 347–372, doi:10.1080/10407799708915114, 1997.

Teunissen, P. J. and Kleusberg, A.: GPS for Geodesy, ISBN-10: 3642720137, vol. 2, Springer Berlin, 1998.

Thayer, G. D.: An improved equation for the radio refractive index of air, Radio Sci., 9, 10, 803–807, doi:10.1029/RS009i010p00803, 1974.

Troller, M., Geiger, A., Brockmann, E., and Kahle, H.-G.: Determination of the spatial and temporal variation of tropospheric water vapour using CGPS networks, Geophysical Journal International, 167, 2, 509–520, doi:10.1111/j.1365-246X.2006.03101.x, 2006.

Verhoeven, D. D.: Multiplicative algebraic computed tomographic algorithms for the reconstruction of multidirectional interferometric data, Optical Engineering, 32, 2, 410–419, 1993.

Vogelmann, H. and Trickl, T.: Wide-range sounding of free-tropospheric water vapor with a differential-absorption lidar (DIAL) at a high-altitude station, Applied optics, 47, 12, 2116–2132, 2008.

Vömel, H., Selkirk, H., Miloshevich, L., Valverde-Canossa, J., Valdés, J., Kyrö, E., Kivi, R., Stolz, W., Peng, G., and Diaz, J.: Radiation dry bias of the Vaisala RS92 humidity sensor, J. Atmos. Oceanic. Technol., 24, 6, 953–963, doi:10.1175/JTECH2019.1, 2007.

Wallace, J. M. and Hobbs, P. V.: Atmospheric science: an introductory survey, ISBN-10: 012732951X, vol. 92, Academic Press, 2006.

Ware, R., Alber, C., Rocken, C., and Solheim, F.: Sensing integrated water vapor along GPS ray paths, Geophys. Res. Lett., 24, 4, 417–420, doi:10.1029/97GL00080, 1997.

Whitney, A., Rogers, A., Hinteregger, H., Knight, C., Levine, J., Lippincott, S., Clark, T., Shapiro, I., and Robertson, D.: A very-long-baseline interferometer system for geodetic applications, Radio Sci., 11, 421–432, 1976.

Wickert, J., Beyerle, G., König, R., Heise, S., Grunwaldt, L., Michalak, G., Reigber, C., and Schmidt, T.: GPS radio occultation with CHAMP and GRACE: A first look at a new and promising satellite configuration for global atmospheric sounding, Annales Geophysicae, 23, 3, 653–658, doi:10.5194/angeo-23-653-2005, URL `www.ann-geophys.net/23/653/2005/`, 2005.

William, H., Flannery, B. P., Teukolsky, S. A., and Vetterling, W. T.: Numerical Recipes in C: The Art of Scientific Computing (Fortran Version), ISBN: 9780521574396, Cambridge University Press, 1996.

Wirth, M.: Measuring Water Vapor with Differential Absorption Lidar, in: Atmospheric Physics, pp. 465–476, Springer, 2012.

WMO: Guide to meteorological instruments and methods of observation, ISBN:9789263100085, WMO, URL `library.wmo.int/pmb_ged/wmo_8_en-2012.pdf`, 2008.

Wolfe, D. E. and Gutman, S. I.: Developing an operational, surface-based, GPS, water vapor observing system for NOAA: Network design and results, J. Atmos. Oceanic. Technol., 17, 4, 426–440, 2000.

Wulfmeyer, V., Behrendt, A., Bauer, H. S., Kottmeier, C., Corsmeier, U., Blyth, A., Craig, G., Schumann, U., Hagen, M., Crewell, S., Di Girolamo, P., Flamant, C., Miller, M., Montani, A., Mobbs, S., Richard, E., Rotach, W., M., Arpagaus, M., Russchenberg, H., Schlüssel, P., König, M., Gärtner, V., Steinacker, R., Dorninger, M., Turner, D. D., Weckwerth, T., Hense, A., and Simmer, C.: Tthe convective and orographically induced precipitation study: a research and development project of the world weather research program for improving quantitative precipitation forecasting in low-mountain regions, Bulletin of the American Meteorological Society, 89, 10, 1477–1486, doi:10.1175/2008BAMS2367.1, 2008.

Xu, A., Xu, Z., Ge, M., Xu, X., Zhu, H., and Sui, X.: Estimating Zenith Tropospheric Delays from BeiDou Navigation Satellite System Observations, Sensors, 13, 4514–4526, 2013.

Xu, G.: GPS: theory, algorithms, and applications, ISBN-13: 978-3540727149, Springer-Verlag Berlin Heidelberg, 2007.

Xu, P., Shen, Y., Fukuda, Y., and Liu, Y.: Variance component estimation in linear inverse ill-posed models, J. Geod., 80, 2, 69–81, 2006.

Zhang, X. and Andersen, O. B.: Surface ice flow velocity and tide retrieval of the Amery ice shelf using precise point positioning, J. Geod., 80, 4, 171–176, doi:10.1007/s00190-006-0062-8, 2006.

Zhu, S., Reigber, C., and König, R.: Integrated adjustment of CHAMP, GRACE, and GPS data, J. Geod., 78, 1-2, 103–108, doi:10.1007/s00190-004-0379-0, 2004.

Zumberge, J., Heflin, M., Jefferson, D., Watkins, M., and Webb, F.: Precise point positioning for the efficient and robust analysis of GPS data from large networks, J. Geophys. Res., 102, B3, 5005–5017, doi:10.1029/96JB03860, 1997.

List of Figures

List of Tables